A Study on Long-Range High-Resolution Coherent Optical Frequency Domain Reflectometry Method with Applying Light-Source Phase-Noise Compensation

光源位相雑音補償を適用した
長距離高分解能コヒーレント光周波数領域反射測定法
に関する研究

February 2015

Yusuke KOSHIKIYA

古敷谷　優介

A Study on Long-Range High-Resolution Coherent Optical Frequency Domain Reflectometry Method with Applying Light-Source Phase-Noise Compensation

光源位相雑音補償を適用した
長距離高分解能コヒーレント光周波数領域反射測定法
に関する研究

February 2015

Waseda University

Graduate School of Fundamental Science and Engineering,

Yusuke KOSHIKIYA

古敷谷　優介

Contents

1. Introduction

1.1. Background

Optical fiber networks began to be deployed for trunk line and submarine systems in the 1980s in Japan to meet the demand for broadband communication [1-1]–[1-3]. In recent year, broadband communication becomes a common lifeline. Fiber-to-the-home (FTTH) services, which were introduced in 1997, are mainstream services for providing such broadband communication [1-4]–[1-8], and their provision to subscribers has spread rapidly. The number of FTTH subscribers in Japan exceeded 24 million at the end of June 2013 [1-9]. As a result, telecommunication carriers have enormous facilities, such as optical fiber cables. In order to ensure the reliability of optical communication systems for broadband services, design, construction and maintenance technologies are of fundamental importance. In particular, attention has been focused on optical fiber monitoring for the cost effective and efficient maintenance of optical networks.

The basic functions of an optical fiber line monitoring should be designed to diagnose reflection and loss events in optical fiber lines and to immediately locate them with the appropriate spatial resolution over the length of more than several kilometers. It is also one of important functions to investigate characteristics of optical fiber lines by the measurement. The optical reflectometry is a promising technology for use in optical fiber monitoring because operators can perform tests from central office (or remotely from anywhere via a network) without installing any equipment in the customer's premises. There are three types of optical reflectometry as follows;

- Optical low coherence reflectometry (OLCR)

- Optical time domain reflectometry (OTDR)
- Optical frequency domain reflectometry (OFDR)

OLCR has a fine spatial resolution of better than micrometer level [1-10], [1-11]. However its measurement range is mechanically limited to a few meters by its measurement principle. OLCR employs a laser with low coherency such as a white light source, and observes an interference generated by the reflection beam from a device and the local beam reflected by the movable mirror in the local arm as shown in Fig. 1-1. The interference is observed only when the distance to a reflection is exactly same as the distance to the mirror because of the low coherency of the light source. Therefore, OLCR can obtain the fine spatial resolution. However, measurable positions are determined by the position of the mirror, and so the movable range of the mirror restricts the measurement range. OLCR is mainly used for measurements of optical devices. As is mentioned above, the measurement range of OLCR is insufficient for the optical fiber line monitoring, and so it is not suitable to employ OLCR to measurements of optical fiber networks.

On the other hand, OTDR has a long measurement range of several tens of kilometers and a moderate spatial resolution of a few-meter level. Therefore it is widely used for optical sensing of optical fiber cable networks and structures, e.g., buildings and bridges. OFDR employs coherent detection technique, and so it is called coherent OFDR (C-OFDR). C-OFDR has the measurement range of a few kilometers and the spatial resolution of micrometer or centimeter. Therefore, it is used for measurements of optical devices or short optical fiber networks.

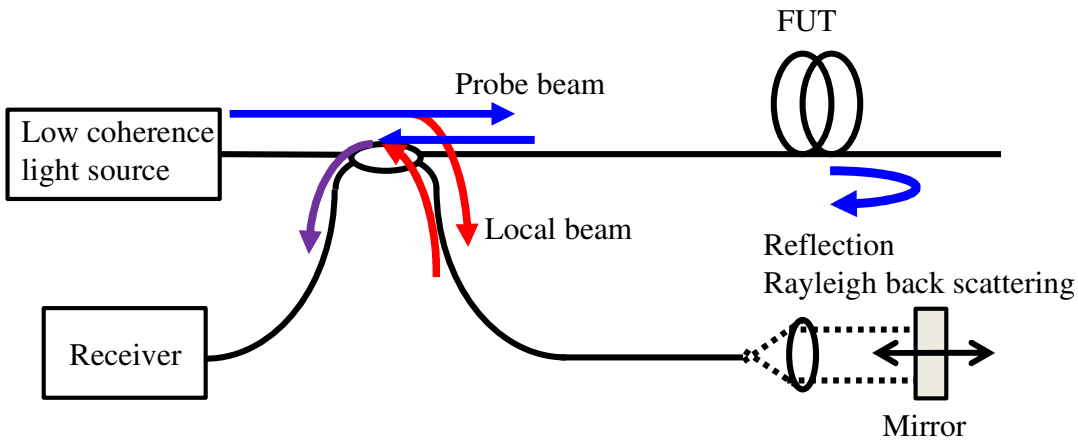

Figure 1-1 Schematic illustration of OLCR

1.2. Optical fiber line monitoring system with OTDR

1.2.1. Principle and system configuration

OTDR is a widely used reflectometry technique for diagnosing optical fiber links [1-12]–[1-18]. As shown in Fig. 1-2, it launches a probe pulse into a fiber (or device) under test (FUT or DUT), and observes the intensities of the back-reflected beams as a function of the arrival time. As a result, a reflection intensity (or reflectivity) versus distance map can be obtained. Typically, OTDR realizes a few meter level spatial resolution over several tens of kilometers. OTDR is employed for diagnosing fiber networks because of its long range and moderate resolution. The spatial resolution of OTDR is directly related to the time resolution of the system, which is determined by either the launched pulsewidth or the bandwidth of the receiver. Both factors are related to detection sensitivity, which means that with OTDR there is a trade-off between the spatial resolution and the measurement range (or the sensitivity).

Figure 1-3 shows the schematic configuration of an optical fiber line monitoring system employing bi-directional OTDRs with two different wavelengths. The test light from the λ_1OTDR in the central office (CO) is introduced into a fiber line by using an L/U-band coupler that includes a dielectric thin filter designed to eliminate U-band wavelengths [1-19]. Chirped fiber Bragg gratings (FBG) are installed in the termination cables in front of optical network terminals (ONTs) as optical filters (hereafter called termination filters) [1-20]. These filters eliminate the test light of the λ_1OTDR and allow a communication light to pass.

1.2.2. Event detection procedure

Figure 1-4 shows a two-tiered procedure where the first step consists of fault isolation, and the second step is precise fault location. The first step is to isolate the categories of faults that have occurred in the optical fiber line or on the customer's premises by using the λ_1OTDR from the CO [1-21]. When a fault occurs, we hear about it first from the customer. This notification informs us whose network, which includes a fiber line and customer equipment (e.g., an ONT and a computer), is disconnected. At this time, however, we cannot isolate the fault category solely from the information provided by the customer. Therefore we have to isolate the fault by using the λ_1OTDR. Since a termination filter with an FBG strongly reflects the test light from the λ_1OTDR, we can isolate the fault category by detecting any change in the reflected power from the termination filters with the λ_1OTDR.

When the branched optical fibers have different lengths, we can distinguish reflections from each termination filter. Here, the difference between fiber lengths must be more than the spatial resolution of the λ_1OTDR. In general, the spatial resolution of the λ_1OTDR is about 2~6 m [1-21]. If there is no change in the reflected powers from the filters, there is a fault in the customer's equipment (e.g., an ONT or a personal computer). If all the reflected powers change from their initial levels, there is a fault in the region sharing a single fiber between the CO and the optical splitter. In this case, we can pinpoint the fault location from the CO by using the λ_1OTDR. When only one of the reflected power levels changes from its initial level, we can also deduce that there is a fault in the branched fiber region between the optical splitter and the ONT of the customer who informed us of the problem with his network.

When all differences between the lengths of fibers are less than the spatial resolution of the λ_1OTDR, which means that one overlapping reflection is observed in OTDR trace, it is difficult to isolate the type of fault. Therefore, a better spatial resolution is required for a wide applicability.

The second step is to locate the fault precisely in the faulty fiber between the optical

splitter and the ONT. After isolating the fault category, the λ_2OTDR should be exchanged for an ONT at the end of the faulty branched fiber. We undertake the fault location by using the λ_2OTDR without cutting or replacing the termination filter because the test light of the λ_2OTDR can pass through the termination filter. The OTDR traces between the splitter and the ONT enable us to pinpoint the fault location in the branched fiber region.

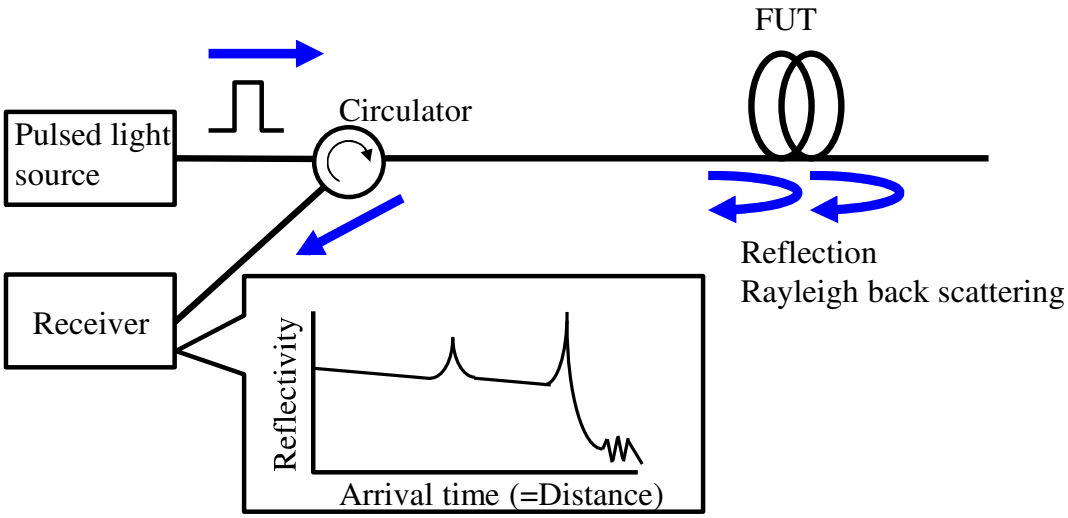

Figure 1-2 Schematic illustration of OTDR

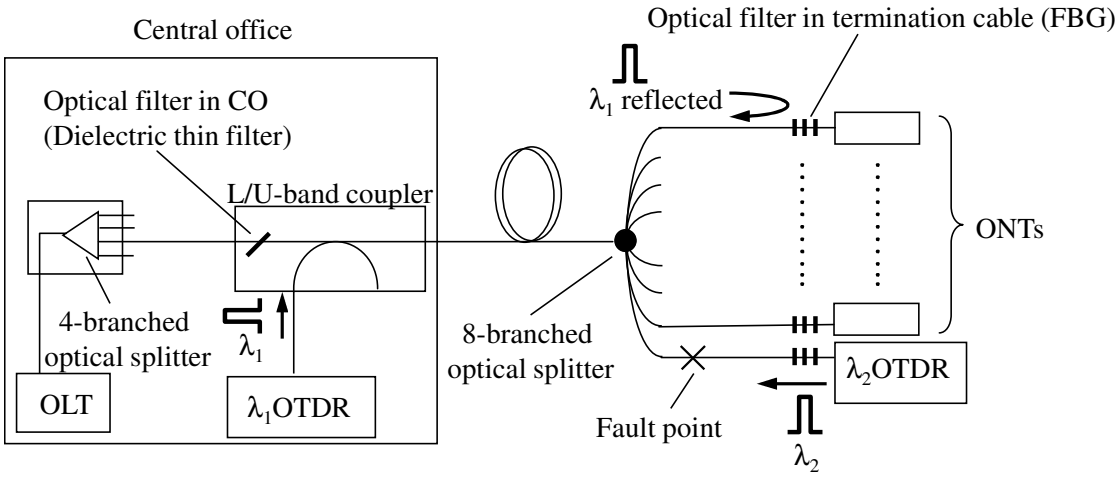

Figure 1-3 Optical fiber line monitoring system employing two-wavelength bi-directional OTDRs

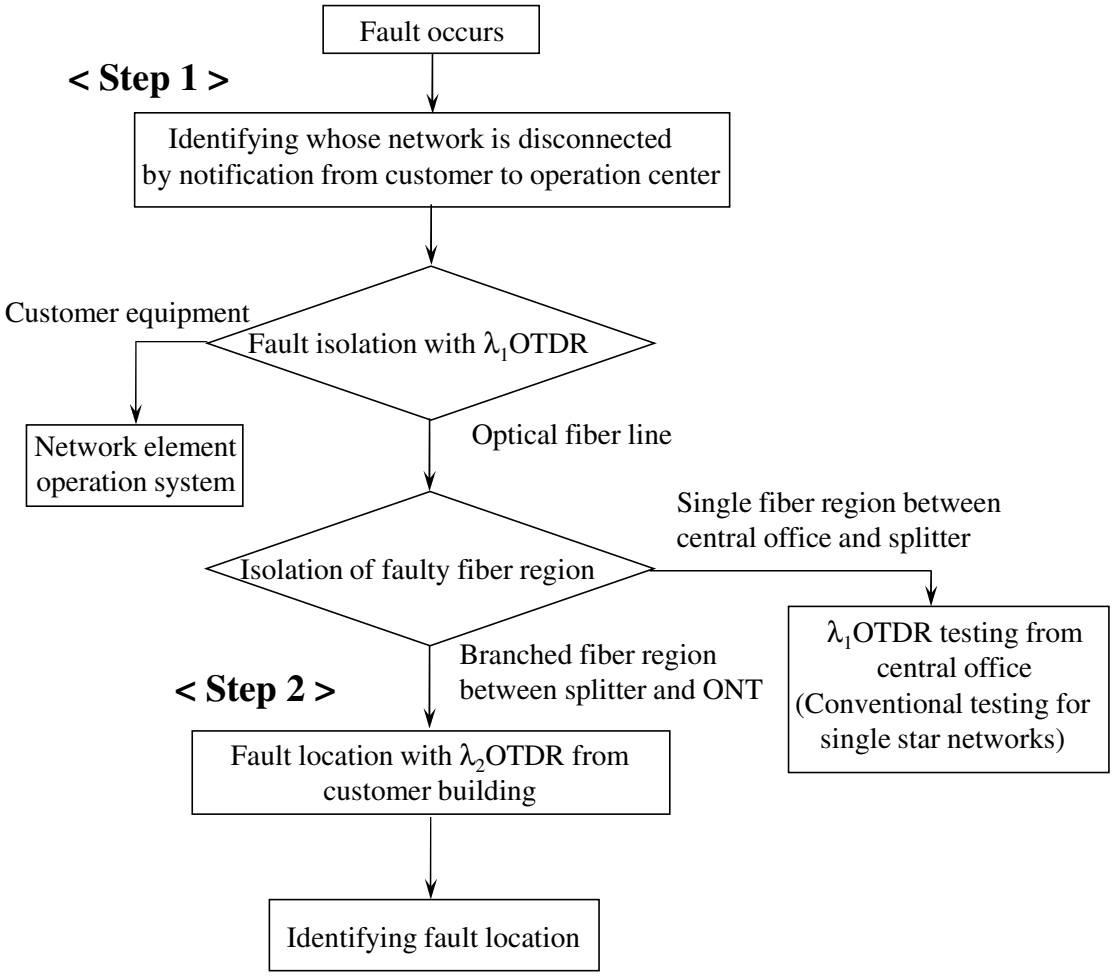

Figure 1-4 Basic procedure for locating faults in branched fibers with OTDRs

1.2.3. Measurement results obtained by monitoring system and procedure

Figure 1-5 shows the experimental setup we used to evaluate monitoring system with the bi-directional OTDR test method and the test procedure. We measured the location of a fault in a test fiber by using the λ_1OTDR and the λ_2OTDR. The test wavelength of the λ_1OTDR was 1650 nm. The test wavelength of the λ_2OTDR used on the customer's premises was 1550 nm. The fiber lengths between the optical splitter and optical filters #1, #2, #3 and #4 were 30, 60, 70, and 150 m, respectively. To add bending loss as a quasi-fault in the fiber #4, we coiled the fiber 1 turn around a mandrel with radiuses R of 6.5 and 10 mm at a distance of 100 m from the optical filter #4. The pulse widths of the λ_1OTDR and the λ_2OTDR were 20 and 35 ns, which correspond to spatial resolutions of 2 and 3.5 m, respectively.

The solid line in Fig. 1-6 shows the OTDR trace when there was no bending loss in the tested fibers and the broken line shows the λ_1OTDR trace of the tested fiber with the bending loss. We were able to distinguish the reflections from the termination filters #1, #2, #3 and #4. A comparison of the values before and after adding the bending loss reveals that the reflection of the optical filter #4 decreased 2.3 dB. The spatial resolution was about 6 m. Therefore, we were able to determine that the fault occurred in the optical fiber line #4 below the optical splitter by monitoring the fluctuation in the reflection.

The solid, broken and dash-dotted lines in Fig. 1-7 show the traces measured by the λ_2OTDR when there was no bend, a bend of R = 10 mm and a bend of R = 6.5 mm, respectively. We can find bending loss at a point 100 m from the termination filter #4. The spatial resolution was 4 m and the dynamic range was 7.5 dB.

As shown in this section, OTDR provides a certain level of maintenances for current networks. However, it is difficult to realize spatial resolution of better than sub meter level and measurement range of longer than several tens of kilometers simultaneously because of the trade-off between the resolution and the measurement range (or the

sensitivity) based on its principle.

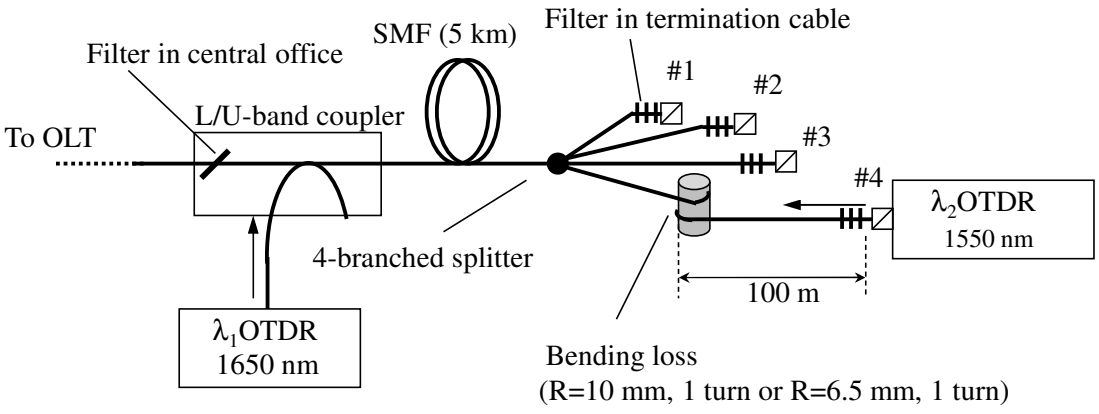

Figure 1-5 Experimental setup.

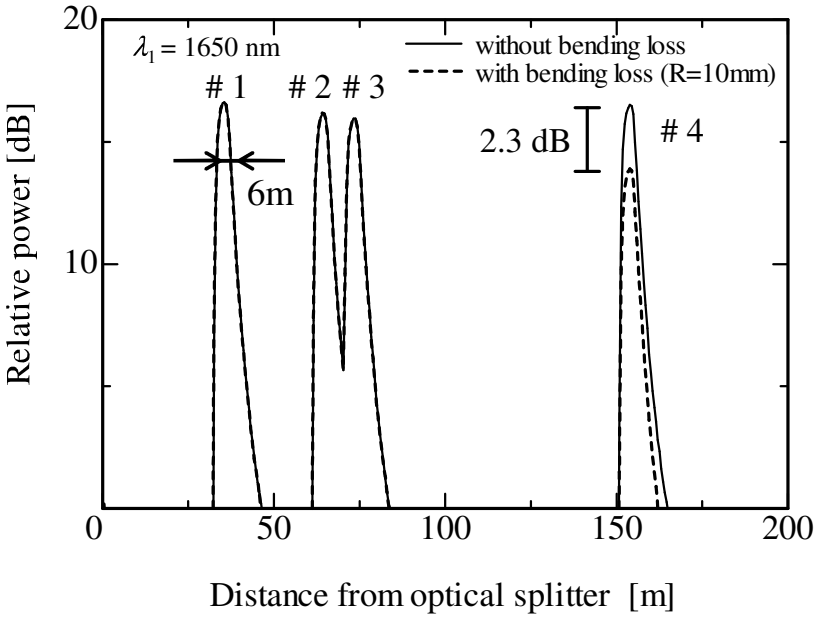

Figure 1-6 OTDR traces obtained by λ_1OTDR from CO.

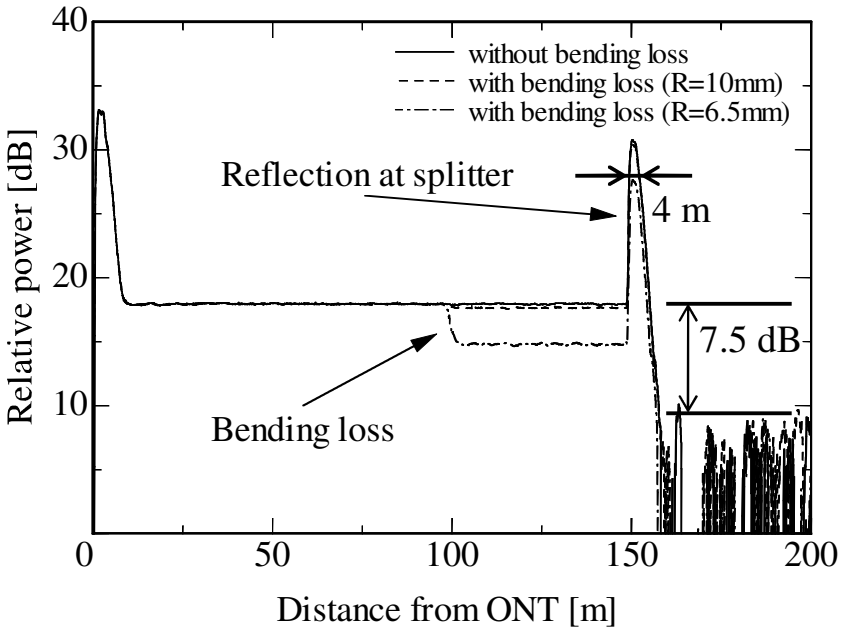

Figure 1-7 OTDR traces obtained by λ_2OTDR from customer side.

1.3. Objective and outline of this thesis

In recent years, various optical components have been installed in networks, and so optical reflectometry with a better resolution and a long measurement range is becoming increasingly important as a tool for the precise observation of adjacent reflection or loss events. Realizing a longer measurement range while maintaining a high spatial resolution is an essential issue as regards the development of optical fiber reflectometry. Such high performance reflectometry technologies would provide a new type of metric for fiber diagnosis, such as discrimination between closely located events in optical access networks or local beat length detection for locating a high polarization-mode dispersion (PMD) section in a trunk line [1-22], [1-23]. For such advanced applications, a required measurement range and a spatial resolution are more than several tens of kilometers and less than sub meter, respectively.

As mentioned in the previous sections, optical reflectometry has been widely used for diagnosing optical fiber networks. In particular, OTDR, which typically has a one- or ten-meter spatial resolution, is one of the most useful reflectometry for conventional applications. However, the performance of conventional OTDR is insufficient as the tool for the advanced maintenance because there is a tradeoff between a spatial resolution and a measurement range resulting in a spatial resolution of more than a few meters. It is also difficult to employ OLCR for diagnosing optical fiber networks because the measurement range is restricted physically by the movable range of the mirror.

C-OFDR is well known as a promising technique for achieving high spatial resolution and high sensitivity. The technique, which is sometimes called a frequency modulated continuous wave (FMCW) technique, was originally developed for radar systems, and has been developed for optical reflectometry since the 1980s [1-24]–[1-36]. In contrast to OTDR, C-OFDR provides a fine resolution but a limited measurement distance. As shown in Fig. 1-8, C-OFDR is a frequency domain technology that uses a continuous probe beam whose frequency is linearly swept. The back-reflected beam

from an FUT is detected by a coherent receiver where the original linearly frequency-swept probe is used as a local beam. Since the reflected beam at a single point in an FUT is a time-delayed replica of the linearly frequency-swept probe beam, a single reflection point yields the photocurrent of a single beat frequency. The beat frequency is proportional to the roundtrip time of the reflection. Therefore, by analyzing the spectrum of the detected photocurrent, we can obtain reflection intensity versus distance map. One of the advantages of C-OFDR is its fine spatial resolution, which is determined by the resolution of the above spectral analysis and is independent of the receiver's bandwidth. Spatial resolutions of much less than one millimeter have been exploited in several studies and commercially deployed. Such a fine resolution is suitable for testing optical devices such as modulators, optical filters, and connectors.

As is mentioned above, the resolution of C-OFDR is equivalent to the resolution of a spectral analysis of the beat signal. In other words, the spectral purity of the beat signal affects the resolution. If the linearity of the frequency sweep degrades as a result of some imperfection in the sweeping mechanism, the spectral purity of the beat signal also degrades. Even if the sweeping mechanism is perfect, the intrinsic spectral broadening of the light source spectrum, namely a phase noise, modifies the sweep linearity. If the roundtrip time of the probe beam exceeds the coherence time, the frequency of the back-reflected probe has uncorrelated fluctuation with respect to the local beam at the coherent receiver, resulting in the degradation of the spectral purity of the beat signal [1-37]–[1-39]. This means that degradation of its spatial resolution is caused by the light source phase noise. The last statement explains why C-OFDR has always been limited to short-range use. It has commonly been perceived that the measurement range with a high spatial resolution for C-OFDR is limited to less than (half the) coherence length of the used light source. It is difficult to use conventional C-OFDR for diagnosing optical networks of several tens of kilometers because the coherence lengths of lasers commonly used for C-OFDR are about several kilometers or less.

The main purpose of this thesis is to realize a long range measurement with a high

spatial resolution and sensitivity by overcoming the limitation of C-OFDR due to the light source phase noise and clarify applicability to optical fiber network diagnostics as shown in Fig. 1-9.

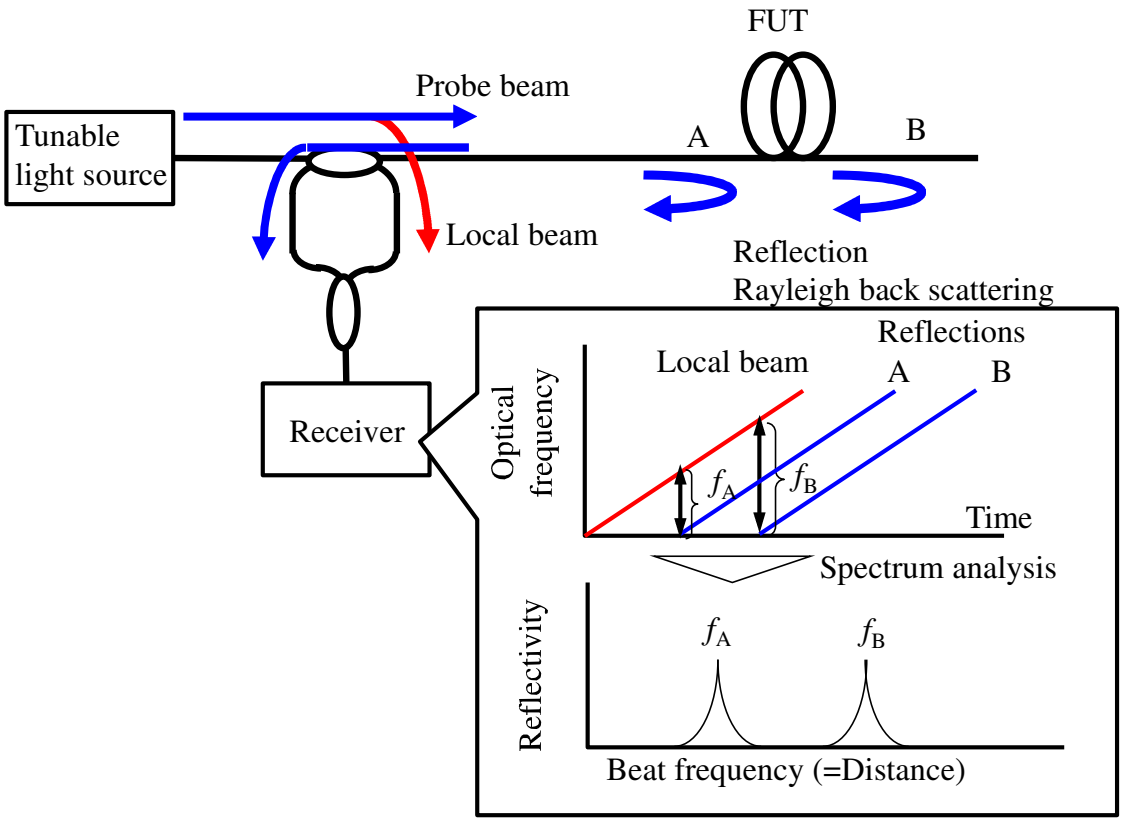

Figure 1-8 Schematic illustration of C-OFDR.

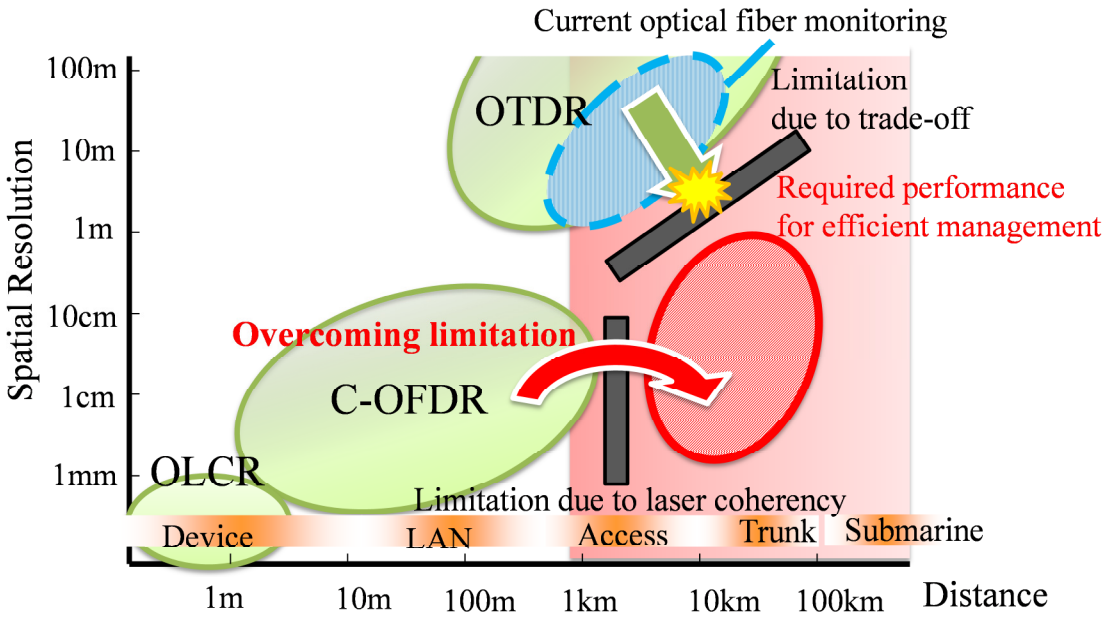

Figure 1-9 Objective of this thesis

Figure 1-10 shows the organization of this thesis, which consists of eight chapters.

After this introduction, chapter 2 describes a basic principle of conventional C-OFDR, an influence of a light source phase noise and its compensation technique for measurements within the light source coherence length. Then, a theory of C-OFDR employing a novel phase noise compensation (PNC) technique, which is called a concatenative reference method (CRM), for measurements beyond the light source coherence length (PNC-OFDR) is described. In the phase noise compensation within the coherence length, a reference signal, which is obtained by a reference interferometer and includes information of the light source phase noise, is used for the phase noise compensation. Our novel compensation technique beyond the coherence length gives reference signals which can be used for the phase noise compensation in the measurement beyond the coherence length. Reference signals can be generated by performing a calculation based on the single reference signal obtained from the single reference interferometer. It is theoretically clarified that PNC-OFDR can compensate for a phase noise for the measurement beyond the coherence length.

Chapter 3 describes C-OFDR with a single sideband with a suppressed carrier (SSB-SC) modulator and a narrow linewidth laser as a tunable light source for improvement in the performance of conventional C-OFDR. The advantage of SSB-SC modulation is clarified theoretically by comparison with a double sideband with suppressed carrier modulation. A centimeter level spatial resolution over a 5 km measurement range and high sensitivity with a noise level of 30 dB lower than the Rayleigh backscattering level is demonstrated.

Chapter 4 describes a basic configuration of PNC-OFDR based on the theory described in chapter 2 and C-OFDR with an SSB-modulator and a fiber laser, which is described in chapter 3. It is also clarified that the dominant factor determining the PNC-OFDR resolution for a long-range measurement is acoustic perturbation acting on FUT. After appropriately compensating for the laser's phase noise, an acoustic phase noise caused by environmental acoustic perturbation plays a dominant role in the deterioration of spatial resolution. It is also demonstrated that a laser-induced phase noise compensation scheme

with the CRM functions ideally, and almost completely eliminates a phase noise even over a 40 km range with sixteen-fold concatenation.

Chapter 5 describes a new scheme for improving the spatial resolution by expanding the optical frequency sweep span of PNC-OFDR. It is clarified that a 3rd-order sideband is generated by employing two $LiNbO_3$ intensity modulators (LN-IM) arranged in series as the external modulator. And the optical frequency sweep span becomes three times broader than that of conventional PNC-OFDR. Based on the scheme, sub-cm spatial resolution measurement over a 10 km range with PNC-OFDR adopting the 3rd-order sideband sweeping is demonstrated

Chapter 6 describes that fading noise in PNC-OFDR can be effectively reduced by applying an optical comb light source without any degradation in the reflectometry performance. The optical comb light source provides broad wavelength tunability, which is required for the frequency shift averaging (FSAV) for fading noise reduction, while maintaining a narrow linewidth of the fiber laser used as a seed lightwave. The deterioration of the spatial resolution is caused by the group velocity dispersion (GVD), when conducting such measurements with a broad lightwave bandwidth to suppress fading noise. It is also clarified that PNC-OFDR with a reference interferometer simultaneously compensates for both a phase noise and GVD induced by wideband measurement and a dispersive medium. It is confirmed that these PNC-OFDR functions enable us to realize a high accuracy measurement of Rayleigh scattering level with low fading noise and high spatial resolution over 10km range.

Chapter 7 describes results of a field test on identification of high-birefringence (or PMD) sections along installed cables with a bandwidth-division PNC-OFDR. The bandwidth-division PNC-OFDR technique, which permits a fast sweep of the optical source frequency, makes it possible to reduce the influence of environmental perturbation, which is the dominant factor degrading the spatial resolution at a long measurement range after the compensation of the light source phase noise. In field tests, we successfully observe beat lengths as small as 20 cm, which shows that there are very large birefringence sections in the installed cables.

Chapter 8 summarizes results obtained in this study.

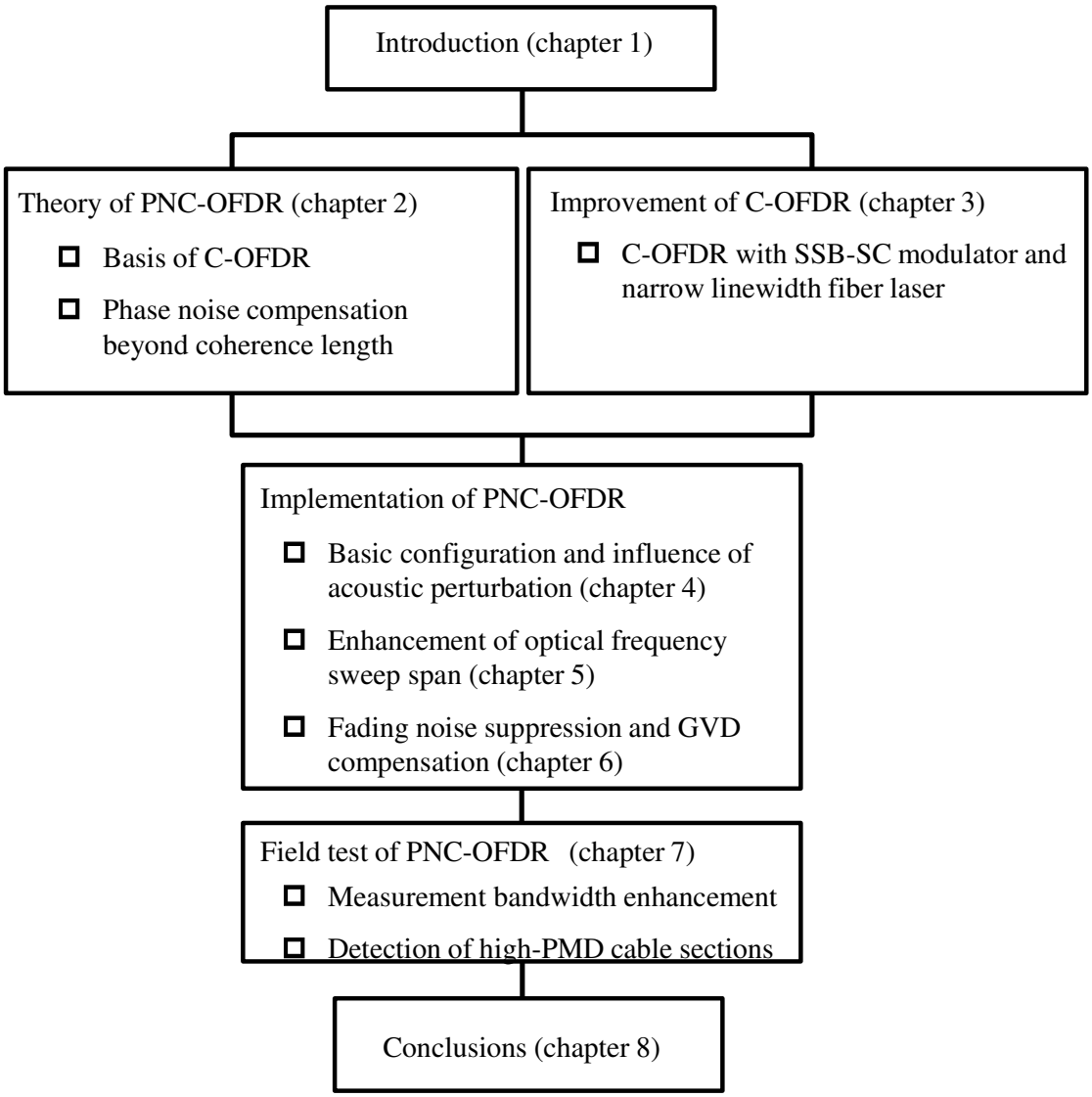

Figure 1-10 Thesis organization.

2. Theory of PNC-OFDR

2.1. Introduction

C-OFDR is attracting considerable attention for monitoring optical communication networks since it provides a narrow spatial resolution [2-1]–[2-4] that enables us to locate closely separated reflection sites in a network under test. Moreover, thanks to the inherently coherent detection, a high dynamic range [2-5], [2-6] can be realized that allows the measurement of Rayleigh backscattering throughout a fiber network. However, the C-OFDR measurement range is limited by the laser coherence length because a laser phase noise causes serious degradation to the signal-to-noise ratio (SNR) as the measurement distance approaches the laser coherence length [2-7]. In order to employ the technique for applications that involve monitoring medium- or long-haul systems, the measurement range can be extended beyond the laser coherence length by using C-OFDR with the CRM, namely PNC-OFDR. In PNC-OFDR, a reference interferometer is used to provide laser phase-noise information to enable us to compensate for the temporal signals of the measurement. The phase noise is canceled out at the best compensation positions or compensated to a lower level when the reflection events occur around the best compensation positions. The “concatenately generated phase” (CGP), which is used for the phase noise compensation with only a single reference interferometer, makes it possible to divide the FUT into several sections and use different CGPs to compensate for the laser phase noise of different sections.

In this chapter, the theory of PNC-OFDR is developed. As preparations for

discussion, section 2.2, 2.3 and 2.4 describe the basic theory of conventional C-OFDR, the light source phase noise and the conventional phase noise compensation technique for the measurement within the coherence length, respectively. Section 2.5 describes the theory of PNC-OFDR. Section 2.6 summarizes this chapter.

2.2. Basic principle of C-OFDR

C-OFDR uses a continuous probe beam whose frequency is linearly modulated with respect to time (see Fig. 2-1). Let T_{sw} be the temporal length of the linear sweep. When we define the sweep rate of the frequency as γ, the total sweep range is given by $\Delta F=\gamma T_{sw}$. Specifically, the coherent length of the probe beam is defined as the time during which it interacts with the back-reflected light described later.

The probe beam is launched into the FUT. The reflected or backscattered beam yielded in the FUT returns to the input end, and is received by a coherent receiver where the original probe beam is used as a local beam. When we consider only a single reflection in the FUT, the reflected beam is a time-delayed replica (the delay equals the round-trip time of the reflection) of the probe beam. As a result, the interference between the reflected and local beams produces a photocurrent at the receiver with a constant beat frequency, f_{beat}, which equals the difference between the optical frequencies of the two interfering beams (see Fig. 2-1(b)). Since the beat frequency is proportional to the round-trip delay, a spectral analysis of the beat signal gives us the reflection intensity as a function of distance.

To observe the above operation in detail, let $E(t)$ be the complex amplitude of the probe beam, then $E(t)$ is given by

$$\begin{aligned} E(t) &= E_0 \exp\{j\Omega(t)\} \\ &= E_0 \exp\left\{ j\left[2\pi\left(f_0 + \frac{\gamma t}{2} \right) t \right] \right\}, \end{aligned} \tag{2-1}$$

where γ (Hz/s) is a sweep rate of the optical frequency, and f_0 is a initial frequency. $\Omega(t)$ represents the phase of the beam, and its derivation,

$$\frac{d\,\Omega(t)}{dt} = 2\pi\left(f_0 + \gamma t\right), \tag{2-2}$$

is an instantaneous angular frequency that evolves linearly with respect to time. Consider a single reflection point in an FUT whose roundtrip time is τ_{FUT}. When the reflected beam returns to the input end, the amplitude $E_R(t)$ is given by

$$\begin{aligned} E_R(t) &= E(t-\tau_{FUT}) \\ &= \sqrt{R}E_0 \exp\left\{ j\left[2\pi\left(f_0 - \gamma\tau_{FUT} + \frac{\gamma t}{2} \right) t \right] \right\}, \end{aligned} \tag{2-3}$$

where the constant phase terms ($= -2\pi f_0\tau + \pi\gamma\tau^2$) are omitted. R is the reflectivity of the FUT. The reflected beam is mixed with the (local) probe beam, and yields a photocurrent represented by

$$\begin{aligned} i_{FUT}(t) &= \sqrt{R}E_R(t)E^*(t) \\ &= \sqrt{R}E_0^2 \cos\left[\Omega(t) - \Omega(t-\tau_{FUT})\right], \end{aligned} \tag{2-4}$$

or

$$i_{FUT}(t) = \sqrt{R}E_0^2 \cos\left[2\pi\gamma\tau_{FUT}t\right].$$

By Fourier-transforming the signal, and recalling that the sweep length is T_{sw}, we obtain the power spectrum of the photocurrent corresponding to the single reflection as

$$\begin{aligned} S_{FUT}(f) &= \left| \int_{-T/2}^{T/2} i_{FUT}(t) e^{j2\pi f t} dt \right|^2 \\ &= RE_0^4 \left[\frac{\sin\pi(f-\gamma\tau_{FUT})T}{\pi(f-\gamma\tau_{FUT})} \right]^2. \end{aligned} \tag{2-5}$$

This sinc function with a peak at $f=\gamma\tau_{FUT}$ corresponds to the single reflection peak located at τ_{FUT}. The spatial resolution of C-OFDR can be represented by the interval between two adjacent zero points, which is given by $1/T_{sw}$. The spectral resolution corresponds to the round-trip delay of $(1/T_{sw})/\gamma = 1/\Delta F$, where ΔF is the total frequency sweep range. Hence, as with every measurement system, the time resolution of C-OFDR is limited by the physical limit, which is given by the inverse of the spectral range of the test signal used. By converting it into the distance, the single-way spatial resolution Δz of C-OFDR is given by

$$\frac{c}{2n\Delta F}. \tag{2-6}$$

where c and n are the light velocity in a vacuum and the refractive index, respectively.

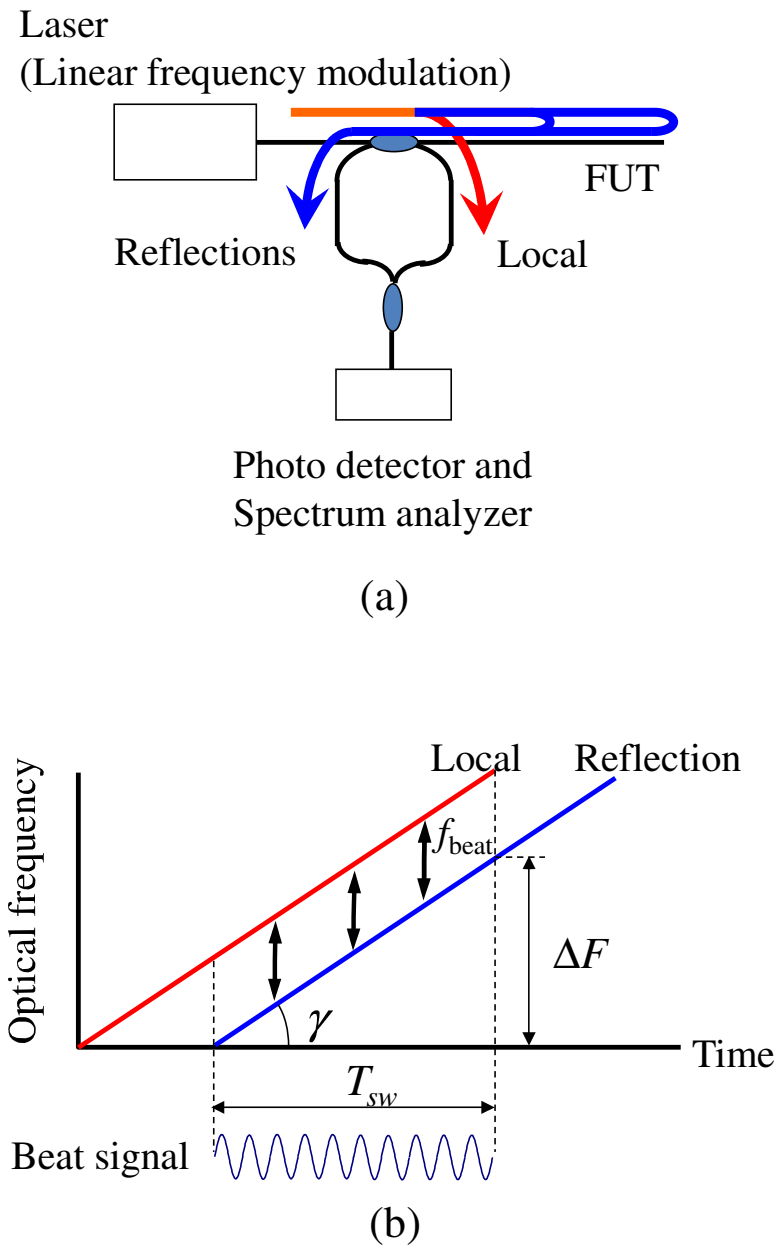

Figure 2-1 (a) C-OFDR configuration and (b) linearly swept optical frequency and beat signal generated from the local beam and reflected beam.

2.3. Light source phase noise

The ideal performance of C-OFDR described in the previous section assumes a frequency sweep with perfect linearity, which is impossible to achieve in practice. In a real C-OFDR system, the frequency sweep is imperfect for several reasons, the result being that the frequency-time trace of the probe beam includes some degree of nonlinearity. Then, the beat frequency for a single reflection fluctuates, the corresponding spectrum is broadened, and therefore the spatial resolution degrades as shown in Fig. 2-2.

The effect of the nonlinearity of the frequency sweep is represented by adding the undesired phase change $\theta(t)$ to (2-1). Then the probe beam is given by

$$\begin{aligned} E(t) &= E_0 \exp\{ j\Omega(t)\} \\ &= E_0 \exp\left\{ j\left[2\pi\left(f_0 + \frac{\gamma t}{2} \right)t + \theta(t) \right] \right\}. \end{aligned} \tag{2-7}$$

The instantaneous frequency of the beam is still given by the derivation of $\Omega(t)$,

$$\frac{d\Omega(t)}{dt} = 2\pi(f_0 + \gamma t) + \frac{d\theta(t)}{dt}, \tag{2-8}$$

where $d\theta/dt$ shows the undesired frequency change. Accordingly, the frequency sweep rate is a function of time:

$$\gamma'(t) = \frac{1}{2\pi}\frac{d^2\Omega(t)}{dt^2} = \gamma + \frac{1}{2\pi}\frac{d^2\theta(t)}{dt^2}. \tag{2-9}$$

There are several origins of $\theta(t)$. One of the most inevitable origins of $\theta(t)$ is the intrinsic spectral broadening of the laser, which is intrinsically added through the

spontaneous photon emission. Other possible origins include imperfections in the sweeping mechanism or mechanical vibration of the laser cavity. Since, $\theta(t)$ is generally a probability value, the trace is not deterministic, i.e., the trace shown here is a sample of the entire event group. The coherence time, τ_C, is defined in Fig. 2-3 as the average length of time during which the frequency trace maintains its linearity, or in other words, the time during which the optical phase (or frequency) maintains its correlation.

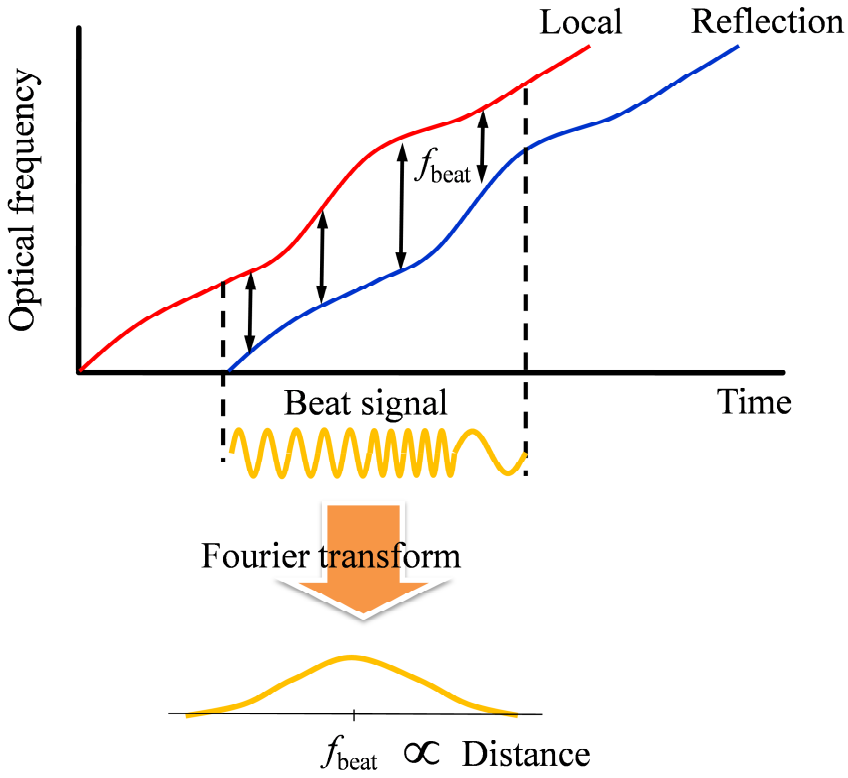

Figure 2-2 Nonlinearity of optical frequency sweep and broadening of beat signal spectrum.

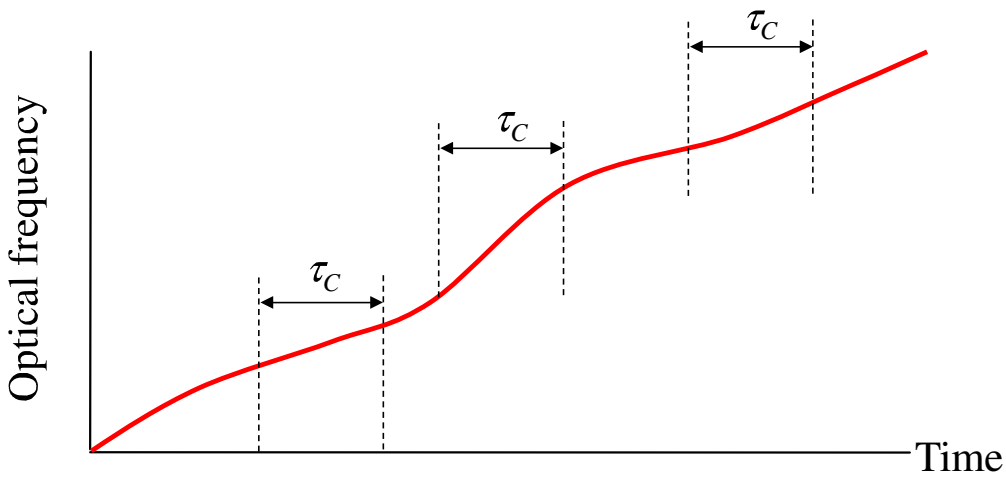

Figure 2-3 Frequency-time trace of the probe beam deformed by the phase noise. τ_C stands for the coherence time of the light source.

2.4. Phase noise compensation within the coherence length

Here we consider the C-OFDR measurements within the coherence time, i.e., when the roundtrip length of the FUT is less than the coherence length of the light source. C-OFDR has conventionally been used within such a range. Figure 2-4 shows the frequency-time trace in such a case for local and back-reflected beams. Recall that the frequency trace is almost linear within the coherence time; hence it is also linear within the delay of the entire FUT. The traces of the local and back-reflected beams are almost parallel to each other throughout the sweep.

The behavior of the beat frequencies with respect to different reflection distances is depicted in Fig. 2-4 for different times. The beat frequency for a single reflection changes with changes in $\gamma'(t)$. However, the proportionality between the beat frequency and the reflection distance is maintained over the entire measurement range. Therefore, the following linear relationship holds between the beat frequency and the round-trip delay:

$$f_{FUT} \cong \gamma'(t)\,\tau_{FUT}\,. \tag{2-10}$$

In such a case, if we obtain the beat signal of a single reflection point as a reference, the beat frequency at any distance can be predicted by

$$\frac{f_{FUT}}{\tau_{FUT}} \cong \frac{f_{ref}}{\tau_{ref}} \tag{2-11}$$

and compensated for by using the linear relationship.

When there is a linear relationship between the beat frequency and the distance over the entire range, the frequency fluctuation can be compensated for by resampling the beat signal from the FUT by the reference beat signal, as shown in Fig. 2-5. Here, the

reference beat as a sampling clock is provided to a data acquisition card (DAC) in order to realize the resampling scheme. This technique has been a standard technology in short-range C-OFDR [2-3], [2-4], [2-8]–[2-10].

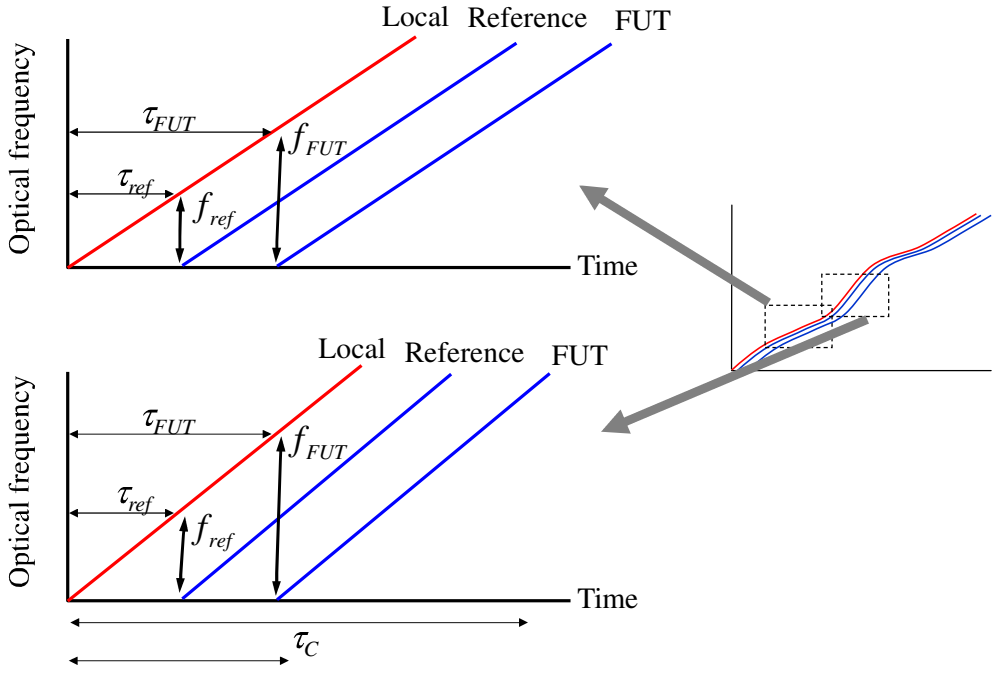

Figure 2-4 Schematic view of C-OFDR operation in a range shorter than the coherence time.

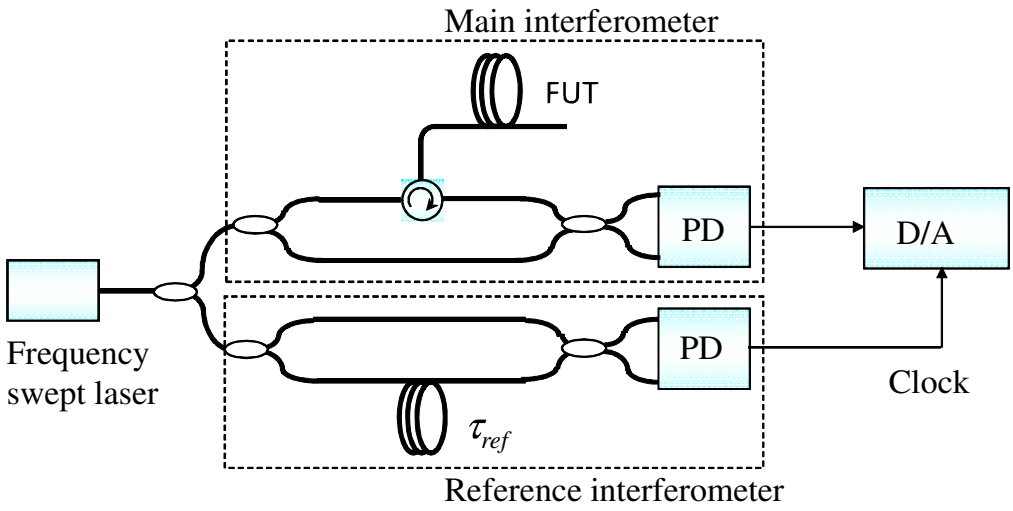

Figure 2-5 Schematic view of C-OFDR configuration in a range shorter than the coherence time.

2.5. Phase noise compensation beyond the coherence length

This section describes the theory of the CRM for PNC-OFDR [2-11], [2-12]. In PNC-OFDR, the reference interferometer is used to provide phase noise information about the optical source used for resampling the temporal signals of the measurement. The phase noise, which is originated from the light source and included in the measurement signal, is then compensated for when the reflection events occur around a distance of half of the delay fiber length in the reference interferometer. The difference from the compensation within the coherence length is to use the CRM. This enables us to compensate for the phase noise over the entire measurement length, which is much longer than the light source coherence length.

Firstly, the compensation within the coherence length is theoretically considered. Let $E(t)$ be the electrical field of the C-OFDR probe beam, whose frequency is linearly swept. Then $E(t)$ is given by

$$E(t) = E_0 \exp\{j[\omega_0 t + \pi\gamma t^2 + \theta(t)]\}, \tag{2-12}$$

where E_0 is the laser optical electric field amplitude, and ω_0 is the initial optical angular frequency. γ is the frequency sweep rate. $\theta(t)$ is the randomly fluctuating optical phase at time t. When a reflection point in the FUT is located at a distance whose round trip time is τ_{FUT}, the beat signal (measurement signal) is given by

$$i_{FUT}(t) \propto \cos[2\pi\gamma\tau_{FUT}t + \theta(t) - \theta(t - \tau_{FUT}) + C_{FUT}], \tag{2-13}$$

where C_{FUT} is a constant. $\theta(t)-\theta(t-\tau_{FUT})$ is the phase noise of the light source. If we adopt a reference interferometer with a delay time τ_{ref}, the obtained reference signal is

$$\begin{aligned} i_{ref}(t) &\propto \cos\left[2\pi\gamma\tau_{ref}t + \theta(t) - \theta\left(t - \tau_{ref}\right) + C_{ref}\right] \\ &\equiv \cos\left[X_{ref}(t)\right], \end{aligned} \tag{2-14}$$

where $X_{ref}(t)$ is the phase term of $i_{ref}(t)$, and C_{ref} is a constant. Compensation is realized by resampling $i_{FUT}(t)$ based on timing corresponding to certain increments in the phase $X_{ref}(t)$, for example π increments. When the resampling time based on π increments is t_M, the following relationship is given:

$$M\pi = X_{ref}(t_M)$$
$$t_M = \frac{M\pi - \theta(t_M) + \theta\left(t_M - \tau_{ref}\right) - C_{ref}}{2\pi\gamma\tau_{ref}}. \tag{2-15}$$

where M is the sampling index. The measurement signal resampled by (2-15) becomes

$$i_{FUT}(t_M) \propto \cos\left[\left(\pi\tau_{FUT}/\tau_{ref}\right)M + \Phi(t_M) + C\right], \tag{2-16}$$

where C is a constant. The phase term $\Phi(t_M)$ is the randomly sampled collection of $\Phi(t)$ shown as follows:

$$\Phi(t) = [\theta(t) - \theta(t - \tau_{FUT})] - \frac{\tau_{FUT}}{\tau_{ref}}\left[\theta(t) - \theta\left(t - \tau_{ref}\right)\right]. \tag{2-17}$$

In fact, (2-16) can be viewed as an expression of a sampled signal from a continuous signal expressed by

$$i_{RFUT}(t) \propto \cos\left[\left(\pi\tau_{FUT}/\tau_{ref}\right)t + \Phi(t) + C\right]. \tag{2-18}$$

The phase noise $\Phi(t)$ is canceled out when τ_{ref} equals τ_{FUT} and remains at a small value when $\tau_{FUT} - \tau_{ref} < \tau_c$, where τ_c is the laser coherence time. Therefore, if we use a reference interferometer whose delay (τ_{ref}) is close to that of the measured reflection point (τ_{FUT}), the phase noise compensation is successfully achieved with the above resampling process.

On the other hand, this is not the case when $\tau_{FUT} - \tau_{ref} > \tau_c$. Suppose that we have

only a single reference interferometer whose delay is around τ_c ($\tau_{ref} \approx \tau_c$), while the FUT is much longer than the delay. The problem is that the reference signal obtained from the reference interferometer is effective only at the roundtrip distance of τ_c in the FUT, namely it cannot compensate for the laser's phase noise over the entire length of the FUT.

The frequency trace is no longer linear in the measurement range, as shown in Fig. 2-6. We can consider using a reference interferometer with a delay of τ_{ref}, which is around the coherence time, and obtaining the reference beat frequency, but the reference cannot estimate the beat frequency at delays beyond the coherence length, at least with the simple linear estimation described above (Fig. 2-6(a)).

The key idea of CRM is described schematically in Fig. 2-6(b). The beat frequency observed with the delay τ_{FUT} (or τ_{ref}) equals the change in the optical frequency during the delay (green arrow). Here we recall that the change in every physical values that occurred in a certain time is a summation of the changes that occurred in its divided time sections. We already know that the frequency change that occurs in time $t-\tau_{ref}$ to t is given by the reference interferometer. Therefore, if we assume that $\tau_{FUT}=N\tau_{ref}$ (N: integer), namely that τ_{ref} is a divided time section of τ_{FUT}, the beat frequency at τ_{FUT} can be calculated using

$$f_{FUT}(t) = \sum_{n=0}^{N-1} f_{ref}(t - n\tau_{ref}). \tag{2-19}$$

If we define the phase of the beat signal, $X_i(t)$, (i = *FUT* or *ref*), by

$$f_i(t) = \frac{dX_i(t)}{dt}, \tag{2-20}$$

then the integral version of (2-19), namely a CGP, is obtained as

$$X_{FUT}(t) = X_N(t) = \sum_{n=0}^{N-1} X_{ref}(t - n\tau_{ref}). \quad (2\text{-}21)$$

$X_N(t)$ can be numerically calculated from $X_{ref}(t)$ and $n\tau_{ref}$, which are obtained with the reference interferometer. Therefore, it is possible to compensate for the laser phase noise by dividing the FUT into several sections and using appropriate $X_N(t)$ values to each sections as shown in Fig. 2-7. Note that although the compensation process is required for every sections, the data need only be acquired once. Moreover, the estimation obtained by using (2-21) is exactly correct, and the perfect phase noise compensation is possible when $\tau_{FUT}=N\tau_{ref}$, and is still effective around the distance corresponding to τ_{FUT}.

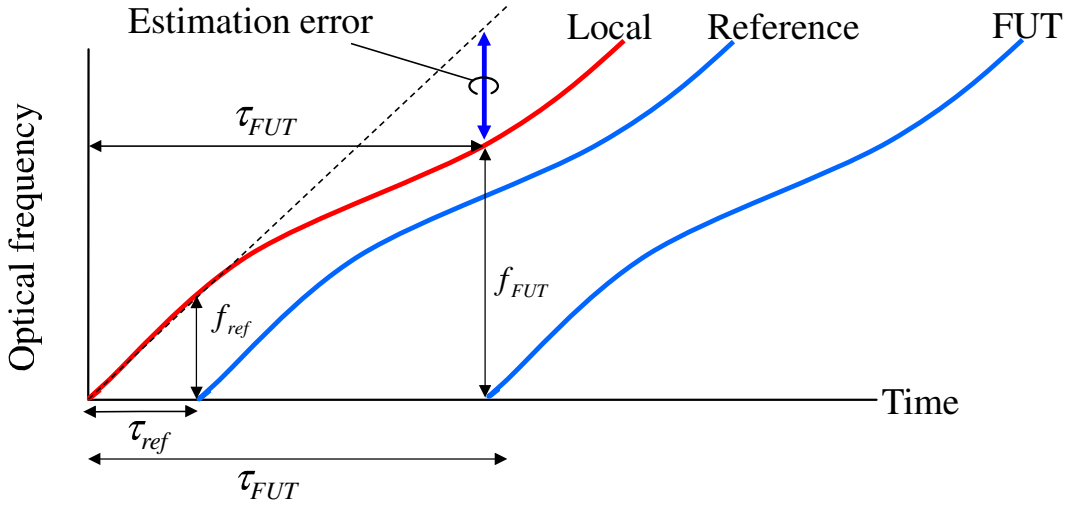

(a)

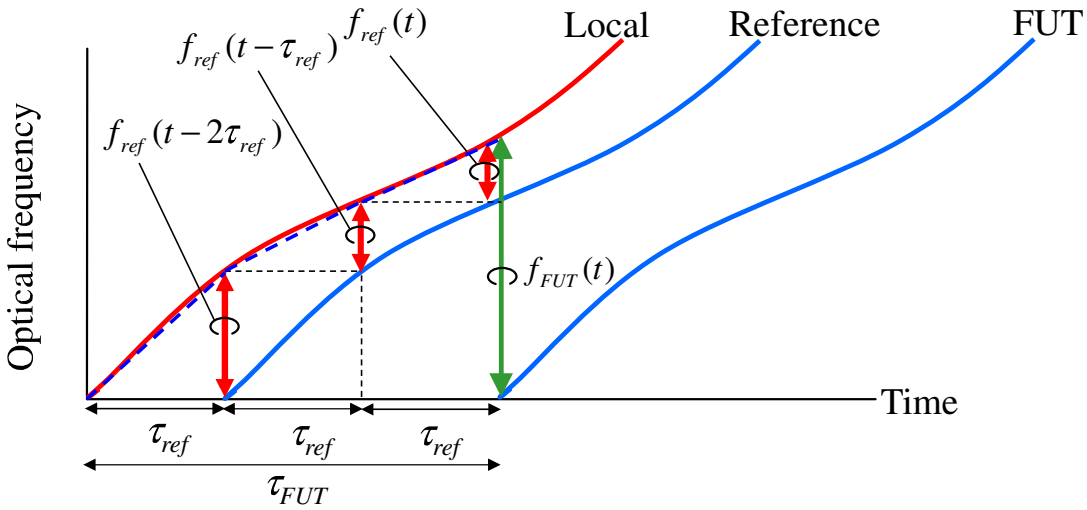

(b)

Figure 2-6 Schematic diagram of the phase noise compensation in PNC-OFDR.

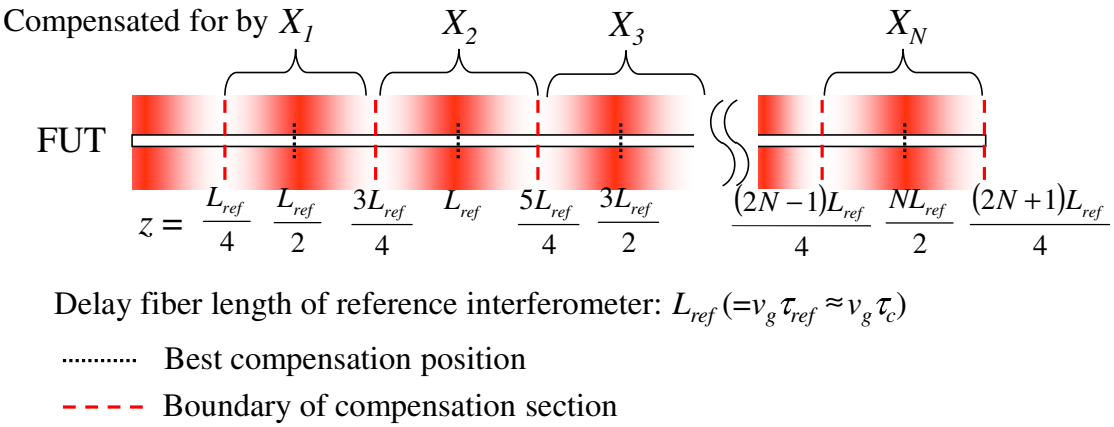

Figure 2-7 Relation between compensation section and newly generated phase signals. L_{ref} is delay fiber length of reference interferometer, and v_g is group velocity.

Next, we consider the effect of the estimation error when the measured distance is different from an integer multiplied by the reference delay. In principal, the proposed phase noise compensation scheme realizes perfect compensation at a measurement distance of $\tau_{FUT} = N\tau_{ref}$. However, this is not guaranteed when $\tau_{FUT} \neq N\tau_{ref}$. It appears that the most natural way to estimate the phase noise at a distance from the best compensation point is to use a linear fitting starting from the best point, as shown in Fig. 2-8. In practice, if the phase noise compensation is accomplished by resampling the measured beat signal according to the reference, the linear estimation described above is automatically employed, and is not exactly correct at $\tau_{FUT} \neq N\tau_{ref}$. (As described later, this resampling is realized numerically by acquiring and storing both the measured and reference signals in a computer.) Therefore, the effect of the error in the described case is important.

An analysis of the remaining phase noise when $\tau_{FUT} \neq N\tau_{ref}$ can be considered under the assumption that the light source phase noise obeys the random walk model. In such a simple case, the variance of the phase difference with time interval τ is given by [2-13]

$$\left\langle \Delta\theta_\tau^2(t) \right\rangle \equiv \left\langle \left[\theta(t) - \theta(t-\tau)\right]^2 \right\rangle = \frac{|\tau|}{\tau_c}, \tag{2-22}$$

where < > denotes the ensemble average.

According to (2-14) and (2-21), the N-th generated phase $X_N(t)$ is given by

$$\begin{aligned} X_N(t) &= \sum_{n=0}^{N-1} X_{ref}(t - n\tau_{ref}) \\ &= 2\pi\gamma N\tau_{ref}t + \theta(t) - \theta(t - N\tau_{ref}) + C_{Nref}. \end{aligned} \tag{2-23}$$

In the linear estimation shown in Fig. 2-8, the phase noise $\theta(t)-\theta(t-\tau_{FUT})$ incorporated in $i_{FUT}(t)$ is estimated by

$$\frac{\tau_{FUT}}{N\tau_{ref}}\left[\theta(t)-\theta(t-N\tau_{ref})\right]. \tag{2-24}$$

Therefore, the remaining phase noise $\Phi_N(t)$ after the compensation is given by

$$\Phi_N(t)=\left[\theta(t)-\theta(t-\tau_{FUT})\right]-\frac{\tau_{FUT}}{N\tau_{ref}}\left[\theta(t)-\theta(t-N\tau_{ref})\right]. \tag{2-25}$$

Consequently, the measured beat signal after compensation is represented by

$$i(t)=\sqrt{R}E_0^2\cos\left[2\pi\gamma\tau_{FUT}t+\Phi(t)+C\right]. \tag{2-26}$$

The effect of the compensation is to reduce the phase fluctuation from $\theta(t)-\theta(t-\tau_{FUT})$ to $\Phi_N(t)$.

Starting from (2-26) and (2-25), and using (2-22), we can calculate the power spectrum of $i(t)$, which corresponds to the reflection profile yielded in PNC-OFDR by a single reflection point located at τ_{FUT}. First, the autocorrelation function of $i(t)$ is calculated, then (2-22) is needed [2-12]. According to the Wiener-Khinchin theorem, the power spectrum of $I(t)$ is obtained as the Fourier transform of the autocorrelation function. The analysis shows that the power spectral density $S_{signal}(f)$ of the coherent interaction factor regenerated by the phase noise compensation process is given by

$$S_{signal}(f)=4R\cdot e^{-2\kappa}\cdot\delta(f-f_{beat}), \tag{2-27}$$

where κ is given by

$$\kappa = \frac{\tau_{FUT}}{\tau_C}\left|1-\frac{\tau_{FUT}}{N\tau_{ref}}\right|. \tag{2-28}$$

By using a new notation,

$$\Delta\tau_{FUT} = \tau_{FUT} - N\tau_{ref}. \tag{2-29}$$

κ is given by

$$\kappa = \frac{|\Delta\tau_{FUT}|}{\tau_c}\left(1+\frac{\Delta\tau_{FUT}}{N\tau_{ref}}\right). \tag{2-30}$$

The first factor, $|\Delta\tau_{FUT}|/\tau_c$, indicates that the coherence decreases exponentially as the measured distance is detuned from the central point, as with the familiar coherence characteristic of random walk phase perturbation. The second factor, $1+\Delta\tau_{FUT}/N\tau_{ref}$, slightly modifies the property of PNC-OFDR, where, for a finite measurement distance, $N\tau_{ref,}$ the degree of the coherence degradation is asymmetrical at shorter and longer measurement distances from the best compensation point. Figure 2-9 plots the signal power as a function of $\Delta\tau_{FUT}$. To be exact, because of the asymmetry, the switching point of the concatenated reference phases, $X_N(t)$, for use in obtaining a better compensation effect is not the mid-point between neighboring best compensation points. However, in the following experiments, we ignore this small problem and employ $X_N(t)$ to compensate for the phase noise in $(N-1/2)\tau_{ref} < \tau_{FUT} < (N+1/2)\tau_{ref}$. The compensation effect works well in the coherence time range of the light source on either side of the mid-point.

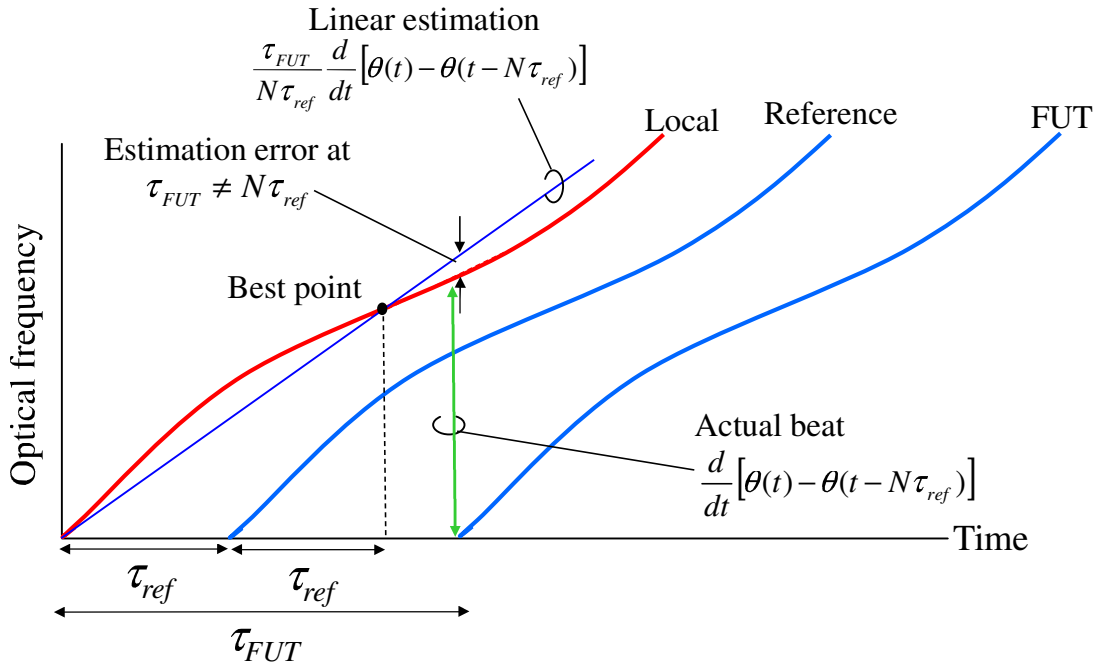

Figure 2-8 Schematic view of the phase noise estimation error when the measured point is at a distance from the best compensation point. (For N=2.)

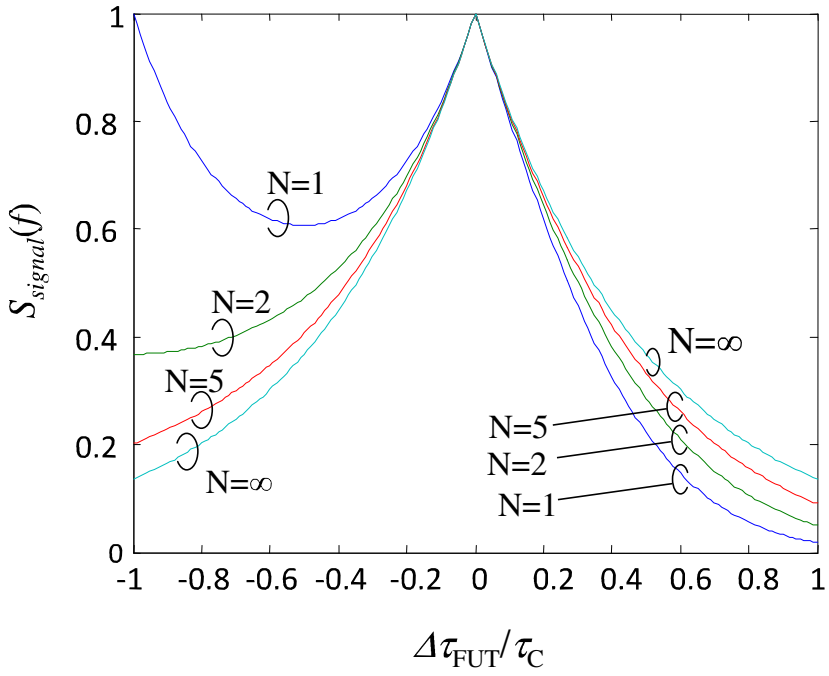

Figure 2-9 Signal intensities as a function of detuning from the best compensation points.

2.6. Conclusion

The theory of C-OFDR employing a novel phase noise compensation technique (or CRM) for measurements beyond the light source coherence length was proposed. The CRM generated appropriate reference signals for the compensation by a single measurement with a reference interferometer and numerical calculation. It was theoretically confirmed that the compensation effect worked well in the coherence time range of the light source on either side of the mid-point in divided sections of FUT. Hence the CRM is effective to overcome the limit of C-OFDR measurement range, and PNC-OFDR can be used for measurements beyond the coherence length.

3. C-OFDR with SSB-SC modulator and narrow linewidth fiber laser

3.1. Introduction

The optical frequency of the tunable light source used in C-OFDR is swept linearly with respect to time, and the lightwave is split into a probe and a local light. The probe light is launched into an FUT. Reflected of backscattered lights from the FUT are recombined with the local light, and a beat signal is generated. The frequency of the beat signal is detected by a receiver and analyzed by Fourier transformation. The beat frequency is proportional to the distance to a reflection point in the FUT because of the linear sweep of the optical frequency. Hence, C-OFDR can measure the longitudinal distribution of the reflectivity in the FUT. The spatial resolution and the measurement range are restricted by the optical frequency sweep range of C-OFDR and the coherence length of the light source used, respectively. Therefore, by considering a laser with broad frequency sweep range and good coherency, a basic performance of C-OFDR can be improved.

On the other hand, C-OFDR cannot overcome the limitation due to laser coherency by only this approach. However, the number of calculation for the phase noise compensation can be reduced by employing the laser with broad frequency sweep range and good coherency as a light source for PNC-OFDR. As a result, PNC-OFDR with high spatial resolution and long measurement range beyond the coherence length can be

rationally realized. Previously reported C-OFDRs have included the use of a tunable laser diode (5 mm spatial resolution for 2 km) [3-1], or an external modulator and a solid-state laser (140 mm spatial resolution for 1 km) [3-2] as the tunable light source. A long range measurement of 95 km achieved with C-OFDR employing a narrow linewidth fiber laser with a piezoelectric transducer for tuning has also been reported but the spatial resolution was not mentioned [3-3].

In this chapter, C-OFDR with a SSB-SC modulator and a narrow linewidth fiber laser as a tunable light source is described [3-4]. This technique realizes frequency tuning while maintaining light source coherence. Section 3.2 explains the basis of a scheme for C-OFDR employing an external modulator as the tunable light source. The SSB-SC modulation and a double sideband with suppressed carrier (DSB-SC) modulation for C-OFDR frequency tuning are also compared theoretically, as a results, the advantage of using SSB-SC modulation is clarified. In section 3.3, an experimental setup employing SSB-SC modulation with a Mach-Zehnder interferometric (MZI) modulator and a narrow linewidth fiber laser is described. Centimeter level spatial resolution over the entire measurement distance up to 5 km, with a noise level of 30 dB lower than the Rayleigh backscattering level, is also demonstrated. Section 3.4 summarizes this chapter.

3.2. Measurement principle of C-OFDR employing narrow line width fiber laser and external modulator

In C-OFDR, the maximum measurement range and the spatial resolution are limited by the coherence length and frequency sweep span of the light source. Therefore, it is extremely important that the light source has a narrow spectral linewidth and a broad frequency sweep span if we are pursuing to achieve long range measurement with high spatial resolution. To realize such a light source, we can employ a tunable laser diode or a narrow linewidth laser combined with an external modulator (e.g., an optical phase modulator or an intensity modulator). By using the tunable laser diode we can realize measurements with a high spatial resolution of several micrometers because of the broad frequency sweep span, but long range measurement is difficult because of the broad spectral linewidth of the laser (e.g., several hundred kHz). In contrast, a tunable light source consisting of a narrow linewidth laser and an external modulator as shown in Fig. 3-1 can sweep the optical frequency while maintaining the high coherency of the laser. This is a major advantage for long range measurement over several kilometers. When the lightwave from a narrow linewidth laser is modulated with a modulation frequency of f_m by the phase modulator or the intensity modulator, the optical frequency of an Nth-order modulation sideband is expressed as f_0+Nf_m ($N\neq0$, integer), where f_0 is the center frequency of the narrow linewidth laser. The modulation sideband frequencies are swept by changing the modulation frequency f_m linearly with respect to time at a frequency sweep rate γ. However, when using such modulators, the beat spectra of the different-order sidebands overlap each other in the frequency domain, and the backscattering profile of the FUT cannot be obtained correctly. To avoid this problem, techniques have been reported that involve insertion of a fiber delay line in a probe lightwave path [3-5] and that use a DSB-SC modulator and an acousto-optic (AO) frequency shifter [3-6]. However, the use of a long fiber delay line, which must be more than twice the length of the FUT, or an AO frequency shifter complicates the C-OFDR configuration. Moreover, the measurement sensitivity deteriorates because a broader

band receiver is needed owing to the higher beat frequency that these techniques induce. In contrast, because SSB-SC modulation can sufficiently suppress an optical carrier and modulation sidebands except for the +1st-order sideband, we have realized a simple configuration without a long fiber delay line or an AO modulator.

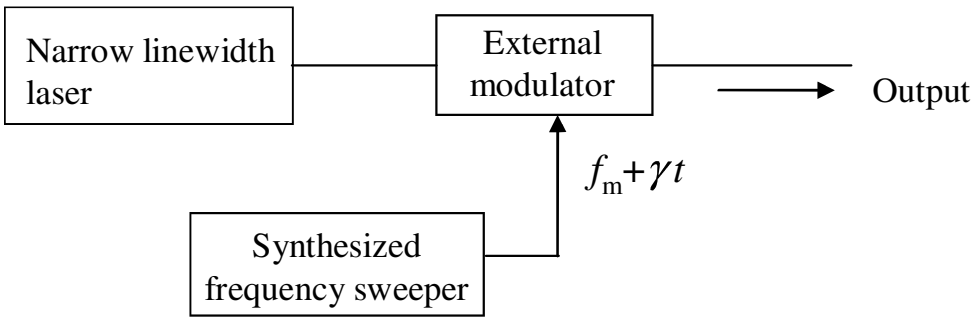

(a)

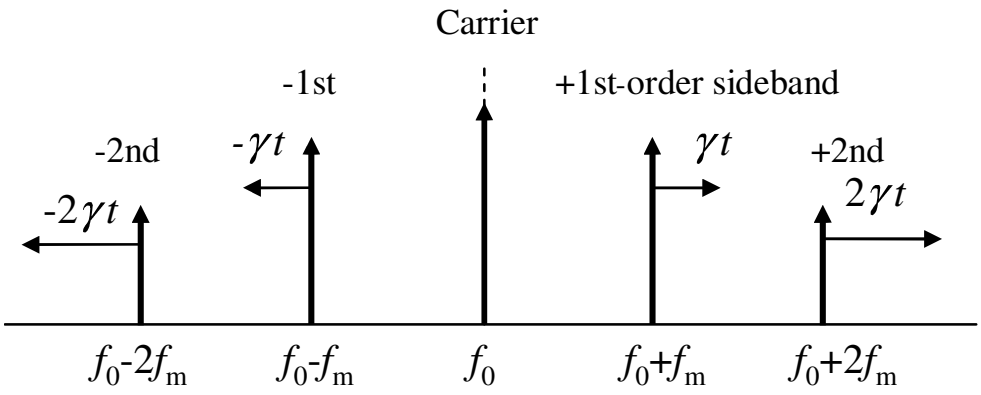

(b)

Figure 3-1 (a) Configuration of tunable light source consisting of narrow linewidth laser and external modulator and (b) spectrum of modulated lightwave.

Figure 3-2 shows a model of a spectrum after modulation. Here, it is assumed that the carrier and modulation sidebands except for the ±1st-order sidebands are negligible because of sufficient suppression. The frequency of the +1st and –1st-order sidebands $f_1(t)$ and $f_{-1}(t)$ are given by

$$f_1(t) = f_0 + f_m + \gamma t \tag{3-1}$$

$$f_{-1}(t) = f_0 - f_m - \gamma t, \tag{3-2}$$

where $\gamma$is the frequency sweep rate, which is defined as $\gamma = \Delta F/T_{\mathrm{swp}}$. ΔF and T_{swp} are the frequency sweep span and frequency sweep time, respectively. The optical fields of the ±1st-order sidebands $E_1(t)$ and $E_{-1}(t)$ are given by

$$\begin{aligned} E_1(t) &= E_0 \exp[\, j(\pi \gamma t^2 + 2\pi f_0 t + 2\pi f_m t)] \\ &= E_0 \exp[j\Phi_1(t)] \end{aligned} \tag{3-3}$$

and

$$\begin{aligned} E_{-1}(t) &= \sqrt{R} E_0 \exp[j(-\pi \gamma t^2 + 2\pi f_0 t - 2\pi f_m t)] \\ &= \sqrt{R} E_0 \exp[j\Phi_{-1}(t)], \end{aligned} \tag{3-4}$$

where E_0 is the laser optical electric field amplitude and R is the power ratio of the –1st and +1st-order sidebands. Namely, R=1 and R<1 mean the DSB-SC modulation and the SSB-SC modulation, respectively. The currents of beat signals between a local lightwave and a backscattered lightwave caused by the –1st and +1st-order sidebands can be written as

$$i_1(t) = \left|E_1(t) + E_1(t-\tau)\right|^2 \propto \cos[\Phi_1(t) - \Phi_1(t-\tau)] \tag{3-5}$$

and

$$i_{-1}(t) = \left|E_{-1}(t) + E_{-1}(t-\tau)\right|^2 \propto R\cos[\Phi_{-1}(t) - \Phi_{-1}(t-\tau)], \tag{3-6}$$

where τ is the total delay time experienced by a probe light relative to a local signal. Of course, there is interference between the +1st and -1st-order sidebands, but it is negligible because their beat frequencies are much higher than those of the signals shown by (3-5) and (3-6). Because $i_1(t)$ and $i_{-1}(t)$ are observed simultaneously at time t, a superimposed current $i(t)$ is given by

$$\begin{aligned} i(t) &= i_1(t) + i_{-1}(t) \\ &\propto X\cos(2\pi\gamma\tau t + \phi), \end{aligned} \tag{3-7}$$

where the electric field amplitude X of the superimposed current is described by

$$X = \sqrt{(R-1)^2 + 4R\cos^2(2\pi f_0\tau)} \tag{3-8}$$

and ϕ is expressed by

$$\phi = \tan^{-1}\left[\frac{\sin(-\pi\gamma\tau^2 + 2\pi f_0\tau + 2\pi f_m\tau) + R\sin(-\pi\gamma\tau^2 - 2\pi f_0\tau + 2\pi f_m\tau)}{\cos(-\pi\gamma\tau^2 + 2\pi f_0\tau + 2\pi f_m\tau) + R\cos(-\pi\gamma\tau^2 - 2\pi f_0\tau + 2\pi f_m\tau)}\right]. \tag{3-9}$$

The amplitude A of the beat signal power is as follows

$$A = X^2 = (R-1)^2 + 4R\cos^2(2\pi f_0\tau). \tag{3-10}$$

Note that the amplitude A of the beat signal power oscillates at the center frequency f_0 of the laser with respect to the total delay time τ. The relationships between the amplitude A and the one way distance z given by (3-10) are shown in Fig. 3-3, where f_0=200 THz, and R=1, 0.1 and 0.01. The distance z is expressed by $z=\tau c/2n$, where c is the velocity of light in a vacuum, and n is the group index of a fiber core. The amplitude of the beat signal power converges to 1 as the sideband power ratio R decreases. The variation in the amplitude A in relation to the distance z for the DSB-SC modulation (R=1) is much larger than that for the SSB-SC modulation (R<1). Moreover, with the DSB-SC modulation, there are distances at which the amplitudes are zero. This means that the detected power of the beat signal is zero at distance intervals of 0.25 μm, and this characteristic is independent of time t. Generally, a spatial resolution of better than 0.25 μm is not achievable with C-OFDR. However, when the fiber expansion and contraction is too slow to be ignored in the measurement time, and there is a reflection at the point where the amplitude becomes zero, C-OFDR employing DSB-SC modulation cannot observe the contribution of the reflection to the value of the measurement point, and so the reflection is overlooked. It should be noted that when there are only reflections that occur continuously along the FUT such as Rayleigh backscattering, the influence of the variation can be disregarded because the value of the measurement point is an integration of the Rayleigh backscattering spectrum from each scatter element existing over many cycles of the amplitude variation within the spatial resolution. These large variations and zero points of the amplitude that are obtained when using DSB-SC modulation become error factors in the reflection measurement. As the sideband power ratio R becomes smaller, as found with SSB-SC modulation, the error of the reflection measurement caused by the distance dependence of the amplitude also becomes smaller. From the above discussion, the SSB-SC modulation should be employed for tunable light source of C-OFDR.

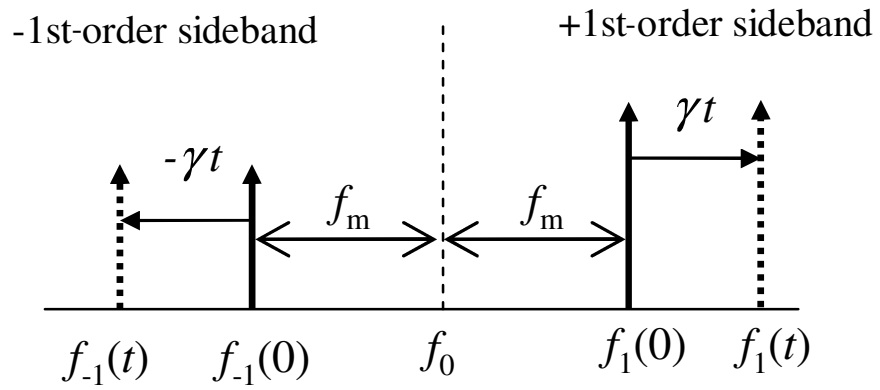

Figure 3-2 Model of lightwave spectrum after modulation.

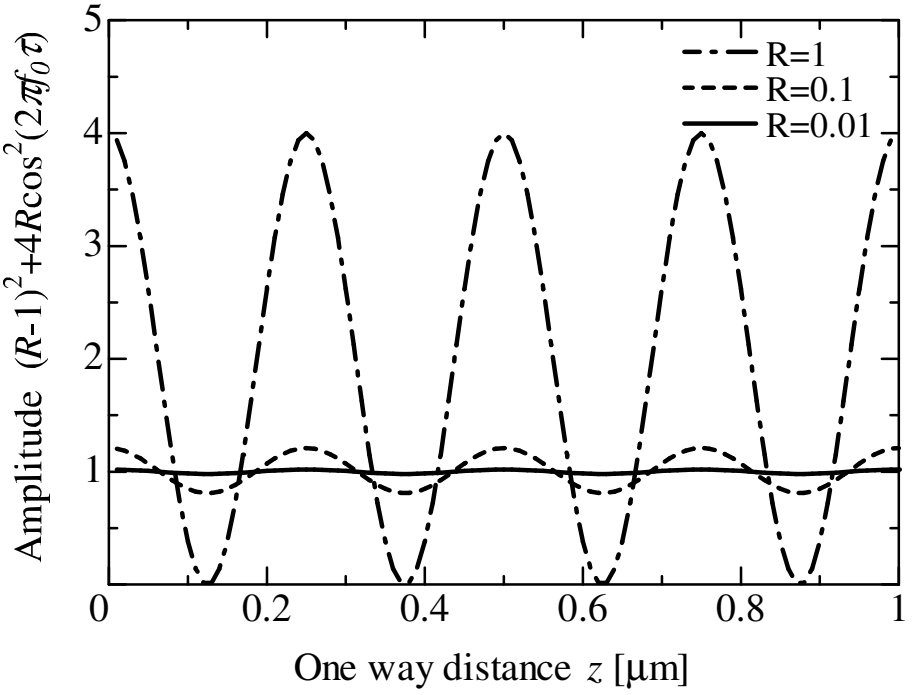

Figure 3-3 Calculated amplitudes *A* as a function of one way distance z by using (3-10) are shown by solid (R = 0.01), dashed (R = 0.1) and dash-dotted (R = 1) lines.

3.3. Experiments and discussion

3.3.1. Configuration

The configuration for experiments is shown in Fig. 3-4. This C-OFDR consists of a tunable light source with an SSB-SC modulator for external frequency sweeping, a main interferometer, which includes the FUT, and a reference interferometer. The light source is a fiber laser with a narrow linewidth (Ethernal^{TM}, Orbits Light wave, Inc.). The linewidth measured by the delayed self-heterodyne approach with an 80 km fiber delay line was 2 kHz. This corresponds to a coherence length of about 30 km in the fiber. The lightwave was modulated with the SSB-SC modulator, which was driven by a synthesized frequency sweeper [3-7]. SSB-SC modulation is realized by using a modulator consisting of a main MZI and two sub MZI as shown in Fig. 3-5. The input lightwave is modulated by $\phi\cos(2\pi f_m t+\pi\gamma t^2)$, $-\phi\cos(2\pi f_m t+\pi\gamma t^2)$, $\phi\sin(2\pi f_m t+\pi\gamma t^2)$ and $-\phi\sin(2\pi f_m t+\pi\gamma t^2)$ at each arm where ϕ is the modulation index. Moreover, the lightwaves are given phase differences of π and $\pi/2$ in the MZI_A and MZI_B, and MZI_C, respectively. Thus, the final output of the optical field $E_{out}(t)$ is expressed as [3-8]

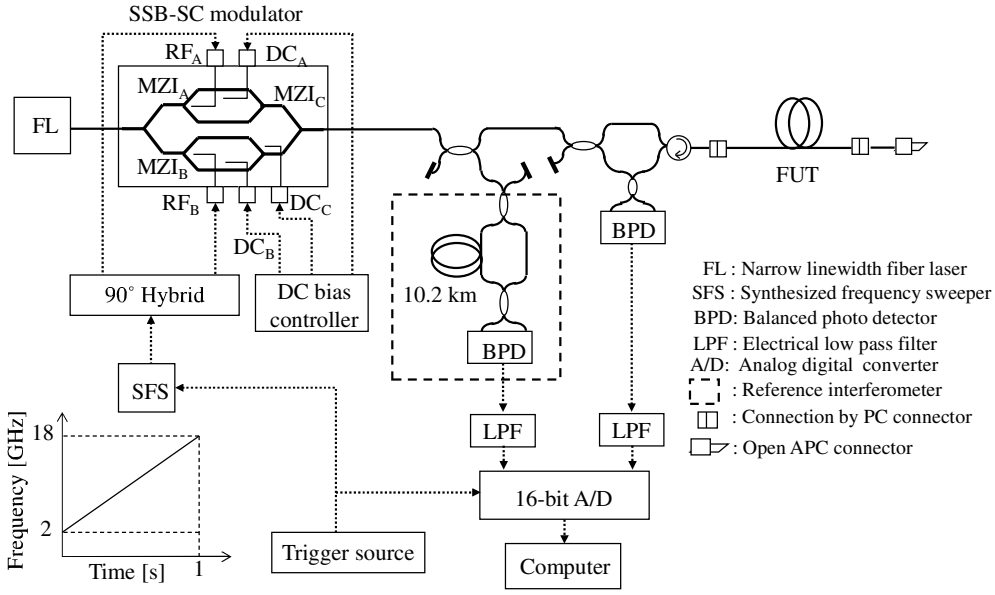

Figure 3-4 Configuration of C-OFDR employing SSB-SC modulator and narrow linewidth fiber laser.

$$E_{out}(t) = \exp(j2\pi f_0 t)[\exp(j\phi\cos\Omega(t)) + \exp(-j\phi\cos\Omega(t))\exp(j\pi) + \{\exp(j\phi\sin\Omega(t)) + \exp(-j\phi\sin\Omega(t))\exp(j\pi)\}\exp(j\pi/2)], \quad (3\text{-}11)$$

where $\Omega(t)=2\pi f_m t+\pi\gamma t^2$. Expanding (3-11) a first-order Bessel function and regrouping the terms, we obtain

$$E_{out}(t) = J_{+1}(\phi)\exp[\, j(\pi\gamma t^2 + 2\pi f_0 t + 2\pi f_m t)] + J_{-3}(\phi)\exp[\, j(-3\pi\gamma t^2 + 2\pi f_0 t - 6\pi f_m t)]. \quad (3\text{-}12)$$

Consequently, the +1st and –3rd-order sidebands remain, and the carrier and the other order sidebands are suppressed. At ϕ=1.8, the influence of the –3rd-order sideband becomes particularly significant. In the experimental setup, RF-signals for the modulation were applied to electrodes RF_A and RF_B by the synthesized frequency sweeper and an RF 90° hybrid coupler as shown in Fig. 3-4. We could realize SSB-SC modulation by applying an RF-signal to only two RF electrodes because we used an x-cut $LiNbO^3$ waveguide [3-9]. Phase differences of π were given between lightwaves passing through the two arms of MZI_A and MZI_B by controlling the DC_A and the DC_B bias voltages. In MZI_C, a phase difference of π/2 was achieved by controlling the DC_C bias voltage. The optical frequencies of the modulation sidebands were swept by changing the modulation frequency of the RF-signal linearly with respect to time. The frequency of the modulation sideband was precisely equal to that of the RF-signal and the frequency sweep of the RF-signal was extremely linear, so we were able to obtain sufficient linearity for the optical frequency sweep. In our experiment, the frequency was swept from 2 to 18 GHz (the frequency sweep span ΔF was 16 GHz). The sweep time was 1 s and the frequency sweep rate γ was 16 GHz/s. The achievable spatial resolution Δz_{min} is given by (2-6). Therefore, the theoretical spatial resolution with this SSB-OFDR setup is 6.25 mm. As shown in Fig. 3-6, the suppression ratio between the +1st-order sideband and the other sidebands (including the carrier) of the spectrum of the SSB modulated lightwave was 20–25 dB throughout the modulation bandwidth of

2–18 GHz. This sufficient suppression of the carrier and sidebands other than the +1st-order sideband enables us to realize a simpler C-OFDR configuration than that for C-OFDR with a DSB-SC modulator, because this setup does not need the delay fiber or acoustic-optic modulator used in [3-6]. A reference interferometer with a 10.2 km-long delay fiber L_{ref} in one arm was used to compensate for the phase noise of the light source within the coherence length [3-10]. In the frequency domain, the beat signal obtained by the main interferometer has a broadened phase noise spectrum, which corresponds to a measurement dead zone and a system noise floor. Therefore, a phase noise compensation is needed. The phase noise level is almost proportional to the distance to a reflection point and its reflectivity [3-11], [3-12]. The phase noise is compensated by resampling the beat signal data of the FUT by using a clock signal generated from phase information about the beat signal obtained from the reference interferometer as described in section 2.3 and 2.4. The compensation is most effective when the length of the delay fiber in the reference interferometer is the same as the round-trip distance to a reflection point because the beat signals from the reference and main interferometers have the same phase information including the phase noise. Therefore, we employed a 10.2 km-long fiber as a delay in the reference interferometer to realize the most effective compensation at the far end of the longest FUT because the longest FUT in our experiment was about 5 km (the round-trip distance is about 10 km). The modulated lightwave was divided and input into the main interferometer and the reference interferometer. The optical power launched into the FUT changed from –12.3 to –21.9 dBm along with the frequency sweep. The change in the optical power is caused by the frequency characteristic of the SSB modulator. The maximum beat frequency corresponding to the reference interferometer and the FUT was about 0.8 MHz for a sweep rate of 16 GHz/s. We sampled the beat signals from both the FUT and the reference interferometer by using a 16-bit analog to digital converter (A/D) with the same 2.4 MHz internal clock for a 1 s acquisition time. The sampled data were filtered at 0.96 MHz with an electrical low pass filter (LPF) for antialiasing. Then, for the compensation, the measured data of the reference interferometer were transformed into

phase information with a computer by using the Hilbert transformation [3-13]. From this phase information, we calculated the time of every phase increase of $\pi/2$. We then numerically resampled the beat signal of the FUT, which had already been sampled with the A/D and stored in the computer, based on the calculated time, which is a newly generated clock for the resampling. The spectrum of the resampled FUT data was analyzed by using a fast Fourier transform with a computer. The frequency was swept once per measurement, and we did not perform the frequency domain averaging any time. We measured five kinds of FUTs, which included a connection with a physical contact connector at the far end as a reflection point. The distances L_{FUT} of the reflection points in each FUT were 0.5, 1.3, 2.5, 4 and 5 km.

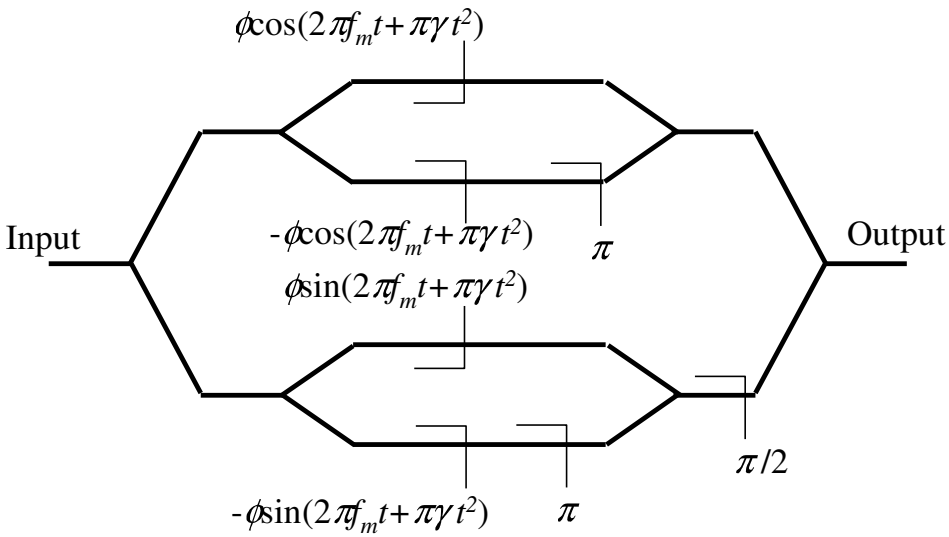

Figure 3-5 Schematic structure of SSB-SC modulator.

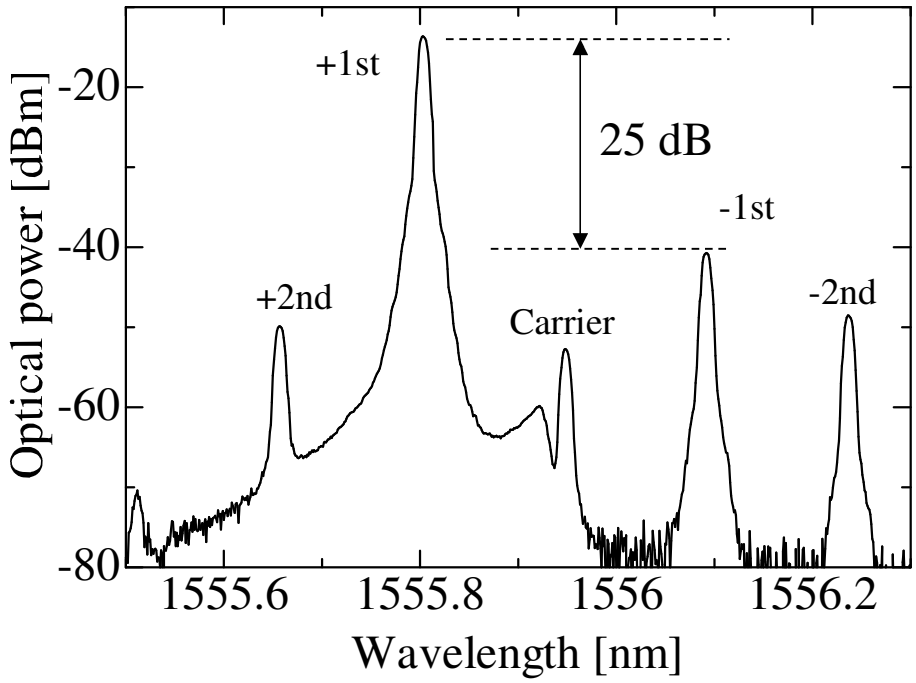

Figure 3-6. Spectrum of SSB-SC modulated lightwave. The modulation frequency f_m was 18 GHz.

3.3.2. Experimental results over 5 km measurement range

Averages and standard deviations of spatial resolutions based on the full width at half maximum (FWHM) obtained from twelve measurements for each different FUT are shown in Fig. 3-7. The open triangles show the averages of the spatial resolution without the phase noise compensation. The solid circles and the error bars show the averages and the standard deviations with the phase noise compensation, respectively. When we employed the phase noise compensation, the average spatial resolution was < 30 mm over 5 km. Figure 3-8 shows the overall view and details of a typical trace for a 5 km-long FUT. The reflectivity was calibrated to the –14.8 dB Fresnel reflection. Rayleigh backscattering was observed clearly over 5 km. Moreover, the sensitivity (relative to the Rayleigh backscattering level) was about –30 dB. As shown in Figs. 3-8(b) and (c), the spatial resolution at 4 m and 5 km were 10 and 18 mm, respectively. One of the reasons for the theoretical spatial resolution of 6.25 mm not being achieved is acoustic perturbations acting on FUT, and its details are described in chapter 4.

No polarization diversity configuration was introduced in any of above experiments. As a result, we observed the periodic variation in the scattered light caused by the birefringence of the FUT as shown in Fig. 3-9. Fluctuations caused by interference among many backscattered signals, namely fading noise, were also observed [3-14]. The fluctuations reduce the loss measurement accuracy in an optical fiber network. In this experiment, the measured standard deviation of the backscattered signal power was about 5.5 dB. The fluctuations can be reduced by employing the well known FSAV technique [3-15], which is described in chapter 6 in detail.

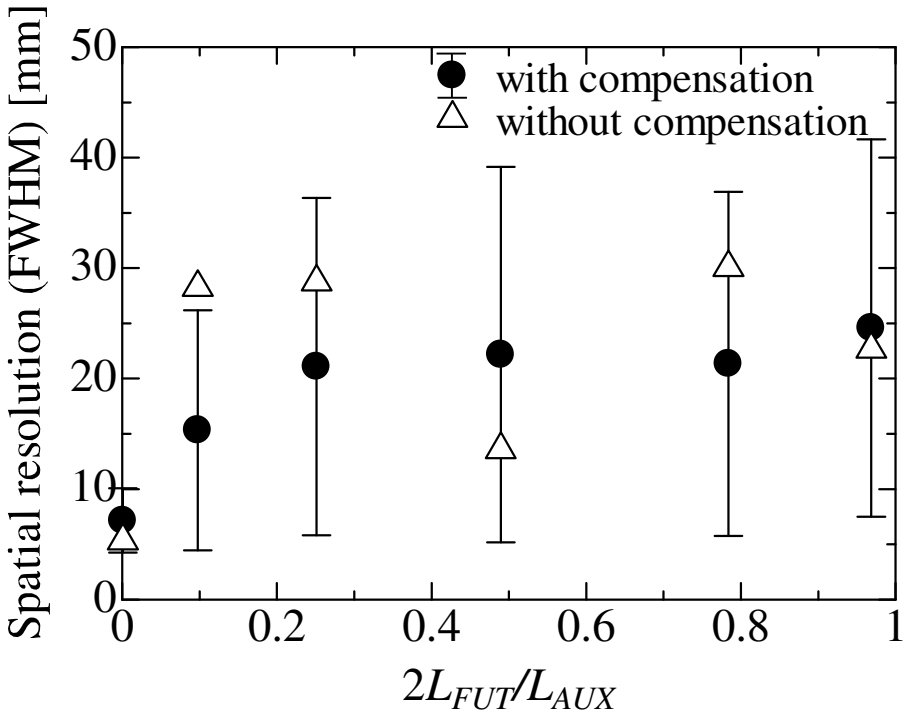

Figure 3-7 Averages and standard deviations of spatial resolutions (FWHM) obtained with twelve measurements for each different FUT as a function of round trip distance up to a reflection point normalized with the delay fiber length in the reference interferometer. Open triangles show the averages of the spatial resolution without the phase noise compensation. Solid circles and error bars show the averages and the standard deviations of the spatial resolution with the phase noise compensation, respectively.

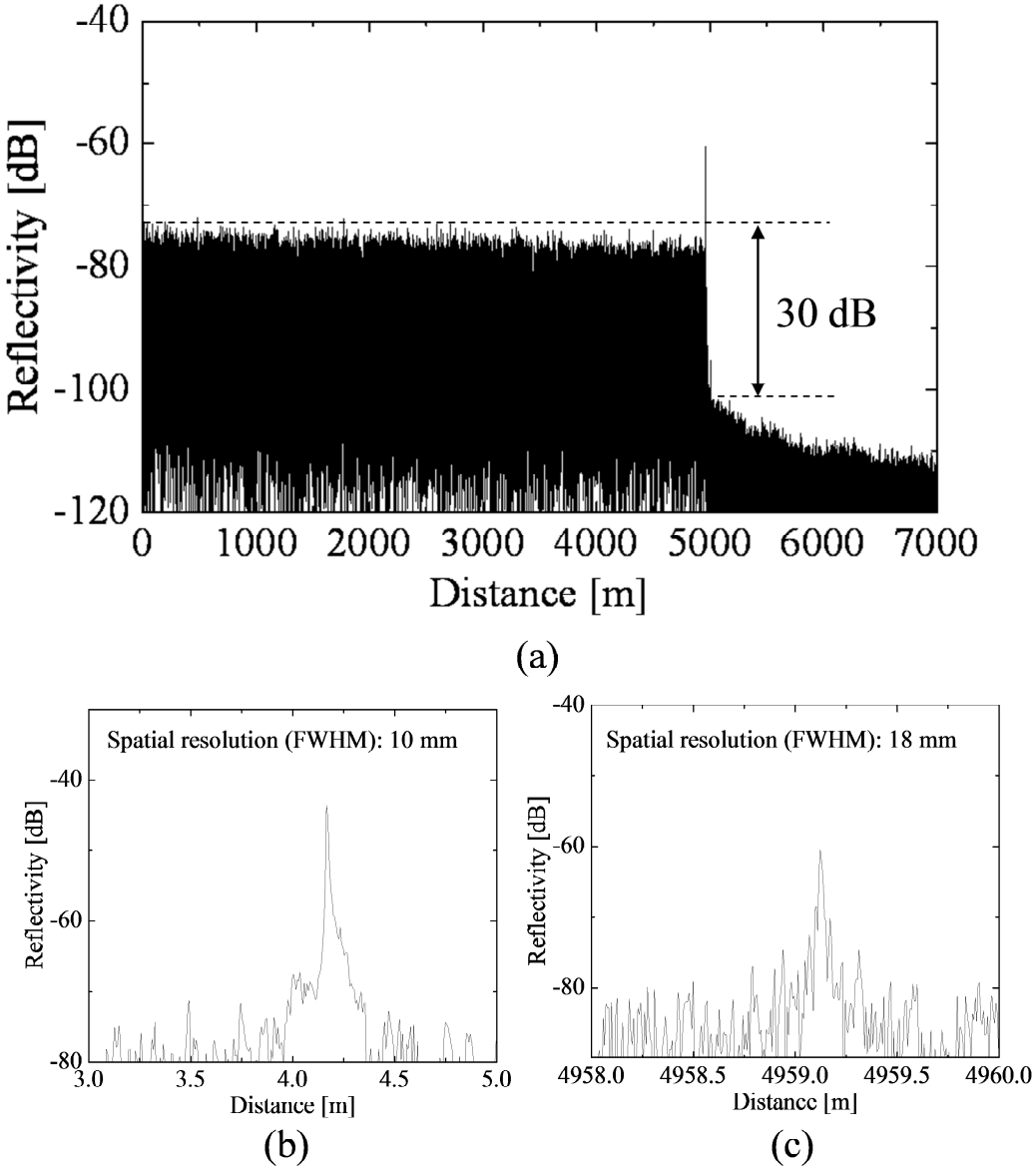

Figure 3-8. (a) Overall view and details of reflection at (b) 4 m and (c) 5 km for a measured reflectivity trace. The reflectivity was calibrated to the –14.8 dB Fresnel reflection.

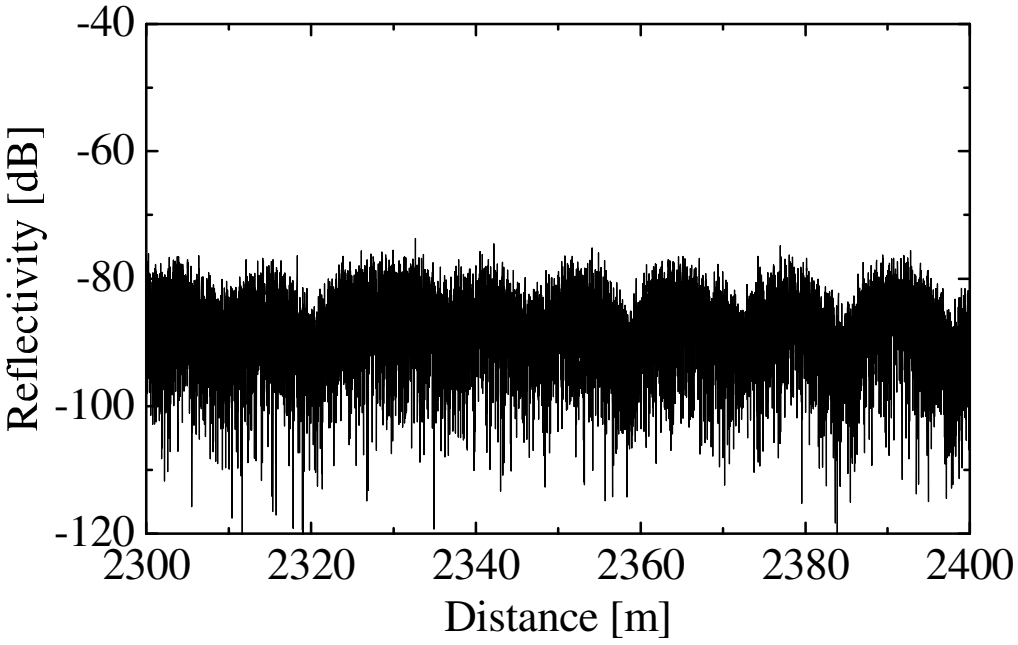

Figure 3-9 Variation in Rayleigh backscattering caused by birefringence of FUT. The reflectivity was calibrated to the –14.8 dB Fresnel reflection.

Figures 3-10(a) and (b) show traces around reflections at 0.5, 2.5 and 5 km without and with the phase noise compensation, respectively. As shown in Fig. 3-10(a), without compensation, the phase noise levels were sufficiently lower than the reflection peaks because the distances to the reflection points were less than the laser coherence length [3-12]. Therefore, there was little difference between the spatial resolution with and without the phase noise compensation as shown in Fig. 3-7 because the reflection peaks were clearly identified even without compensation. When there was no compensation, the phase noise increased with respect to distance. By contrast, when compensation was employed, as shown in Fig. 3-10(b), the phase noise was greatly reduced at a distance of 5 km (the round-trip distance was 10 km), which was almost the same length as the delay fiber in the reference interferometer, because the compensation is most effective when the round-trip distance to a reflection point is the same as a length of the delay fiber line in a reference interferometer [3-16]. At 0.5 km, the low phase noise level was achieved after the compensation despite the effectiveness of the compensation being modest at best because the original phase noise level before the compensation was low. At 2.5 km, the phase noise level after the compensation was the highest in our measurement because the original phase noise level was also high and the effect of the phase noise compensation was modest at best. If there is a strong reflection in an FUT, Rayleigh backscattering around the reflection is enveloped in the phase noise caused by the reflection. This is a measurement dead zone and we cannot obtain reflectivity information around the reflection point. Then, if we employ the phase noise compensation, the measurement dead zone is reduced because of the reduced phase noise level. This means, for a measurement within the laser coherence length, the phase noise compensation is effective in reducing the measurement dead zone rather than in improving the spatial resolution.

The phase noise also influences the noise floor, which corresponds to the sensitivity. The phase noise is generated by reflection and Rayleigh backscattering. The noise floor is increased by the broad spectrum of the phase noise when its level is higher than that of other noise factors such as shot noise and the thermal noise of electrical circuits of a

receiver. In fact, when the reflection at the far end of the 5 km-long FUT was eliminated, the observed noise floor was almost maintained. Moreover, when the fiber laser was turned off, the thermal noise level of the receiver was 4 dB lower than the observed noise level in our experiment. These results mean that the dominant factor as regards the noise level of –30 dB (relative to the Rayleigh backscattering level) after compensation in our experiment is not the phase noise generated by the reflection at the far end but the integrated power of the phase noise spectrum skirts generated by Rayleigh backscattering along the FUT.

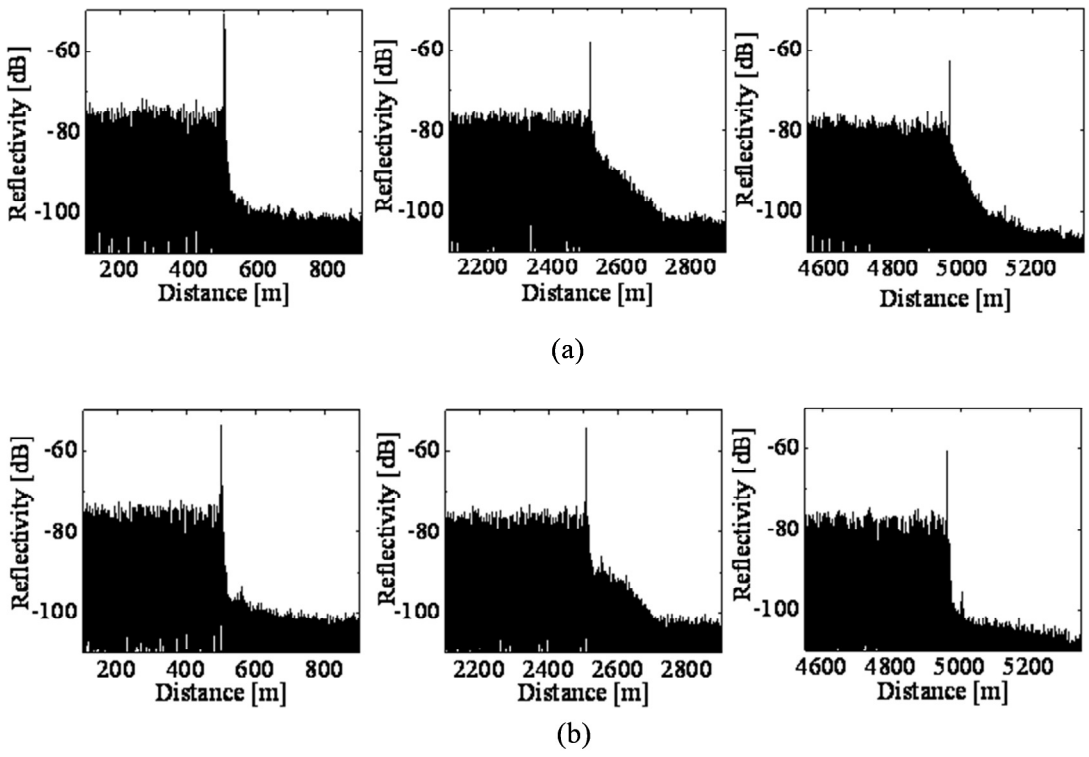

Figure 3-10 Traces (a) without and (b) with the phase noise compensation around reflections at 0.5, 2.5 and 5 km. The reflectivity was calibrated to the –14.8 dB Fresnel reflection.

When a reflection event occurred at a distance of about 10 km (one-way distance), this C-OFDR did not work well to provide a narrow peak for the reflection because of the increased phase noise. Therefore, the maximum measurement range of this C-OFDR setup is more than 5 km but less than 10 km.

The measurement range is limited by the phase noise caused by the laser, namely the light source coherence, and environmental disturbances such as the vibration of an optical fiber cable degrade the spatial resolution although C-OFDR with the SSB-SC modulator and the fiber laser improves the measurement range up to 5 km. Therefore, if C-OFDR is employed to diagnose longer optical fiber networks, it is needed to employ the phase noise compensation technique for measurements beyond the coherence length, namely the CRM mentioned in the previous section. It is also required to investigate the influence of disturbances to ensure a high spatial resolution in field applications because with long-range measurements, the signal is affected by the disturbances over long range, and these perhaps broaden the reflection spectrum.

3.4. Conclusion

C-OFDR employing an SSB-SC modulator and a narrow linewidth fiber laser as a tunable light source was described. The advantage of this scheme is that long range measurement over several kilometers can be realized because the optical frequency sweep is conducted while maintaining the high coherency of the narrow linewidth fiber laser. The superiority of using SSB-SC modulation for the external modulation by theoretically comparing the use of SSB-SC and DSB-SC modulation was also clarified. When DSB-SC modulation was used, it was confirmed that there were distances where the amplitude of the obtained beat signal was zero. This causes errors in the reflectivity measurement. In contrast, when SSB-SC modulation was used, there were no such distances and the amplitude, and they were almost constant with respect to distance. It is the advantage of using SSB-SC modulation for the C-OFDR frequency sweep. A 5 km range measurement with cm-level spatial resolution was demonstrated. Rayleigh backscattering was observed clearly over the whole range. The average spatial resolution (FWHM) was < 30 mm over a 5 km-long FUT and the sensitivity was –30 dB relative to the Rayleigh backscattering level. It is significant to improve basic performances of C-OFDR by employing the laser with higher coherency and broader sweep span, which consists of the SSB-SC modulator and the narrow linewidth fiber laser, because PNC-OFDR can be rationally realized by using both the laser and the phase noise compensation described theoretically in section 2.5.

4. Configuration of PNC-OFDR and influence of acoustic perturbation of fiber

4.1. Introduction

The attempt described in chapter 3 expanded the C-OFDR measurement range by the tunable light source using a narrow linewidth fiber laser and external modulator. However, the laser's finite coherence remains a major factor limiting such an expansion. In chapter 2, PNC-OFDR employing the CRM to overcome this limitation imposed by the laser coherence length was theoretically described. Basically, measurements beyond the coherence length can be realized by CRM. However, the number of a concatenately generated phase (or amount of calculation required for obtaining them) is decided by the laser coherence length. If a light source with long coherence length is used, we can reduce the number of calculation for the phase noise compensation, resulting in a shorter measurement time. Therefore, it is quite significant to combine PNC-OFDR and the tunable light source with a good coherency as shown in chapter 3.

On the other hand, the spatial resolution was degraded by the remaining noise as the reflection event became more remote [4-1], [4-2], although it has been shown theoretically that the spatial resolution can be maintained when using the CRM even if the measurement distance exceeds the laser coherence length as shown in chapter 2 [4-3]. We must therefore consider the remaining noise and its origin if we are to achieve improved performance for long-range measurements with PNC-OFDR.

In this chapter, first of all, the basic configuration of PNC-OFDR with a tunable light source consisting of the SSB-SC modulator and fiber laser is described in section 4.2. Section 4.3 explains that the performance of PNC-OFDR is affected by the acoustic phase noise caused by environmental acoustic perturbations applied to fibers [4-4]. It is dominant factor degrading the spatial resolution of final results after employing the light source phase noise compensation. Moreover, when both the reference interferometer and the FUT are insulated against acoustic perturbation, the theoretical spatial resolution is obtained. This means that a laser induced phase noise compensation scheme with the CRM works almost ideally and eliminates the light source phase noise even over a 40 km range with sixteen-fold concatenation. Section 4.4 explains that in the measurement beyond the coherence length, even when a laser with a very narrow linewidth of a few kHz is used, a dominant factor in performance degradation is not the acoustic phase noise but the laser induced phase noise, and it is effective to employing the CRM. Test results for an actual fiber cable installed in underground show that there is no severe degradation in performance, and that PNC-OFDR sustains its unique high resolution in actual field use. Section 4.5 summarizes this chapter.

4.2. Basic configuration of PNC-OFDR

Figure 4-1 is a diagram of the PNC-OFDR configuration. It includes two interferometers: a main interferometer (MI), which includes the FUT, and a reference interferometer (RI) with a constant reference delay, τ_{ref}. The reference delay should be set around the coherence length of the light source. Too long a reference delay cannot compensate for the full range of a section divided, whereas too short a reference delay requires a large amount of summing up for the concatenative reference generation process, which might inefficiently exhaust the resource of the computer used for the calculation. While the measurement is under way, the output beat signals from the main and reference interferometers are simultaneously acquired by A/D and stored in memories. By using the measured reference signal, a personal computer numerically generates the appropriate reference, namely CGP $X_N(t)$, according to the distances of the divided section, and resamples the data from the main interferometer based on the CGP for the phase noise compensation.

The above phase noise compensation is realized with a program written using LabView. The program uses the reference delay, τ_{ref}, to calculate (2-23). For this purpose, we measured τ_{ref} with an accuracy of about 5 ns and input it into the program. In our experience, this amount of τ_{ref} misevaluation does not seriously affect the quality of the compensation (see section 4.3). The program consists of the following five steps:

(1) The phase of the reference beat signal is extracted by using the Hilbert transformation. This corresponds to $X_1(t)$.

(2) A set of $X_1(t-n\tau_{ref})$ is calculated by time-shifting $X_1(t)$. Since, in most cases, the time, $n\tau_{ref}$, does not coincide with the sampling point, this calculation needs interpolation.

(3) The compensation section N is selected. From the obtained $X_1(t-n\tau_{ref})$, $X_N(t)$ is calculated according to (2-23).

(4) At every increment of $X_N(t)$, time stamps, t_m, are attached to the MI signal. We calculate the values at the time stamps by interpolation. The obtained new

measurement signal is Fourier transformed. This is the final result for the N-th section ($(N-1/2)\tau_{ref} < \tau_{FUT} < (N+1/2)\tau_{ref}$).

(5) Procedures (3) to (5) are repeated for every section, and the results are combined.

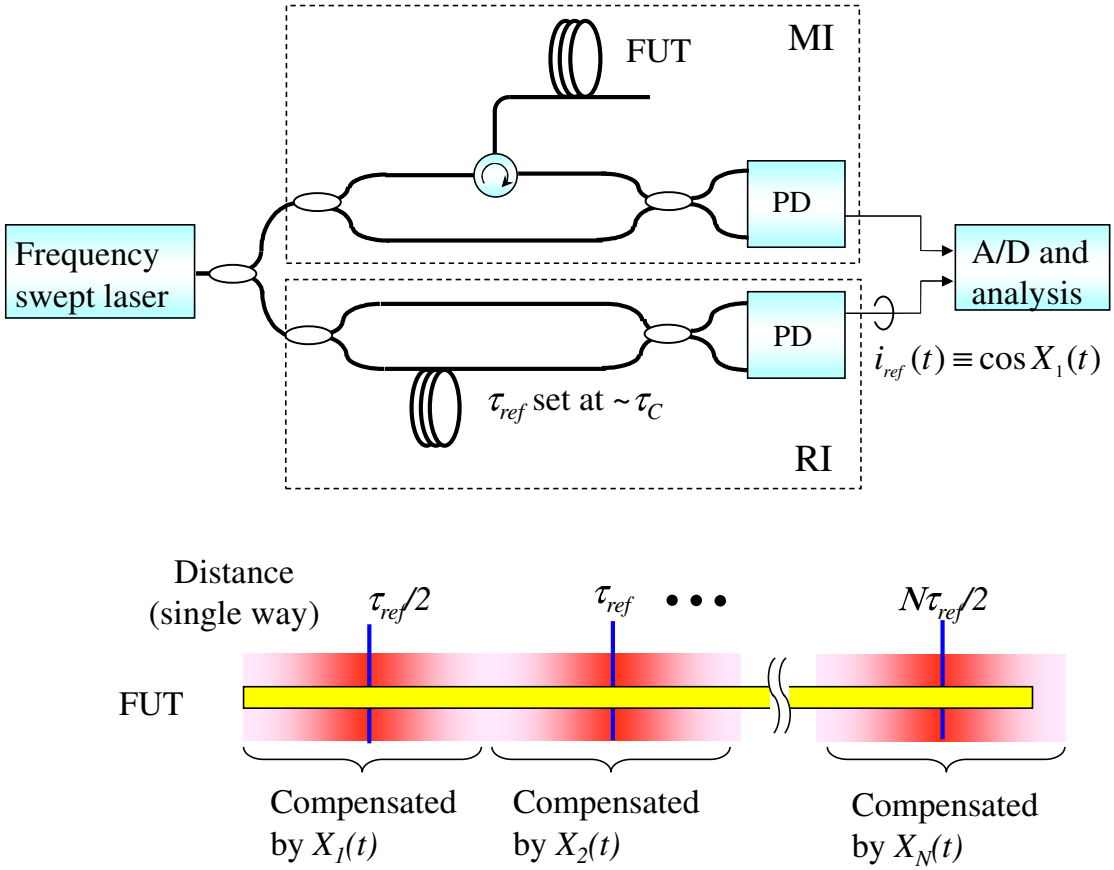

Figure 4-1 Schematic of PNC-OFDR configuration

Figure 4-2 shows an experimental setup. We used a fiber laser with a narrow linewidth (Koheras Adjustik^{TM}) as the PNC-OFDR test light. The linewidth measured using the self-delay heterodyne method with a 100 km delay fiber was about 4 kHz, corresponding to a measurement range of 7.5 km with conventional C-OFDR taking the round-trip path into consideration. An SSB-SC modulator and an RF synthesizer were used for sweeping the optical frequency [4-5]. The frequency sweep span ΔF was about 2 GHz, and this corresponds theoretically to a spatial resolution Δz_{min} of 5 cm. The frequency sweep rate $\gamma$was 400 GHz/s. It should be noted that when measuring 30 and 40 km-long FUTs we set the sweep rate at 200 GHz/s due to the limitation of the sampling rate of the A/D that we used. A Mach-Zehnder interferometer with a 5 km-long delay fiber line (DFL) in one arm was used as a reference interferometer for the laser phase noise compensation, and was placed in a sound-proof box to insulate it from acoustic noise (see section 4.3 for more information). We used a simple hand-made soundproof box consisting of wooden-walls and soundproof mats. The main interferometer consisted of a local arm and a measurement arm and was equipped with a circulator for launching the test light into the FUT and receiving the signal reflected from the FUT.

Polarization diversity was employed to eliminate polarization sensitivity. The measurement results had no influence even when we changed the polarization state alignment because of the polarization diversity scheme. Beat signals from both the main and the reference interferometers were detected with balanced photo detectors and then acquired with the 12-bit A/D at a sampling rate of 200 MS/s. The obtained data were stored in a personal computer for the phase noise compensation process mentioned above.

The FUT lengths were L_{ref} − 2 m (a), $2L_{ref}$ + 37 m (about 10 km), $4L_{ref}$ + 61 m (about 20 km), $6L_{ref}$ + 96 m (about 30 km) and $8L_{ref}$ + 95 m (about 40 km). They were wound on a bobbin and their far ends were the open end of a physical contact connector (4 % reflection). Each FUT was measured 50 times at a single wavelength. We obtained the final waveform by averaging the 50 results after employing the phase

noise compensation process.

The delay of the reference interferometer τ_{ref} was preliminarily measured by using the sampling system with the same time base as the PNC-OFDR measurement. The sampling rate was 200 MS/s, and so the accuracy was 5 ns. The obtained delay was 24545 ns, and this was used for the compensation process with (2-23).

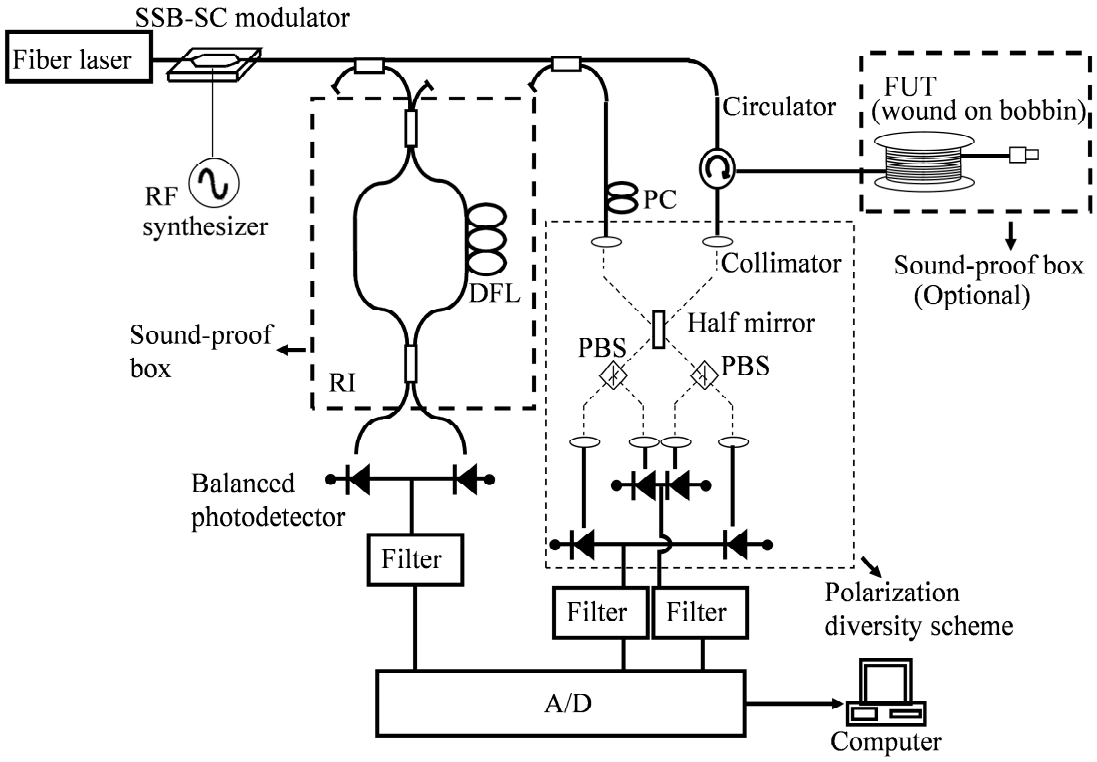

Figure 4-2 Configuration of PNC-OFDR. SSB: single sideband, RF: radio frequency, DFL: delay fiber line, FUT: fiber under test, PC: polarization controller, PBS: polarization beam splitter, A/D: analog to digital converter.

4.3. Dominant factor limiting performance of PNC-OFDR

It was theoretically clarified that the CRM perfectly compensates for the light source phase noise at the best compensation positions as shown in chapter 2. In previous reports, however, the spatial resolution deteriorated and the theoretical value was not achieved even though the CRM was used [4-1], [4-2]. In this section, we clarify the reason for the degraded spatial resolution of PNC-OFDR.

In the first experiment, we insulated both the reference interferometer and the FUT to protect them from the acoustic perturbation to allow us to investigate its influence, and we compared the data we obtained with and without the insulation. Figure 4-3 shows sound pressure density spectra measured in and out of a soundproof box, which was used to provide insulation. The soundproof box was placed in a relatively noisy laboratory environment with a rather loud computer server one meter from the experimental setup. The soundproof box provided effective insulation against acoustic noise of more than 100 Hz. The sound levels, which are numerically integrated values of sound pressure density spectra, were 62 dB (22 mPa) and 57 dB (14 mPa), respectively. Consequently, in all the experiments, a sound pressure of 62 dB acted on the FUT and/or the reference interferometer without the insulation. On the other hand, a lower sound pressure of 57 dB acted on the FUT and/or the reference interferometer when the insulation provided by the soundproof box was used. The CRM was employed for all the measurements presented in this section.

The blue line in Fig. 4-4 shows the far end reflection of 40 km-long FUT when neither the reference interferometer nor the FUT were insulated. The reflection shape was somewhat different from the theoretical shape obtained with the CRM, which is a sinc^2 function whose envelope is shown by the black dashed line. Moreover, no clear reflection peak could be observed due to the remaining noise. Then we put both the reference interferometer and the FUT into soundproof boxes to insulate them from acoustic noise, and the obtained spectrum is shown as the green line. This result agrees with the theoretical line with an SNR of 25 dB. The obtained spatial resolution was also

5 cm, namely the theoretical value. Here, the horizontal axis in Fig. 4-4 is the frequency deviation Δf with respect to the peak (lower axis), and it also indicates the distance deviation ΔL from the reflection position (upper axis), which satisfies $\Delta f = 2\gamma\Delta L/v_g$ (0.5 m/kHz).

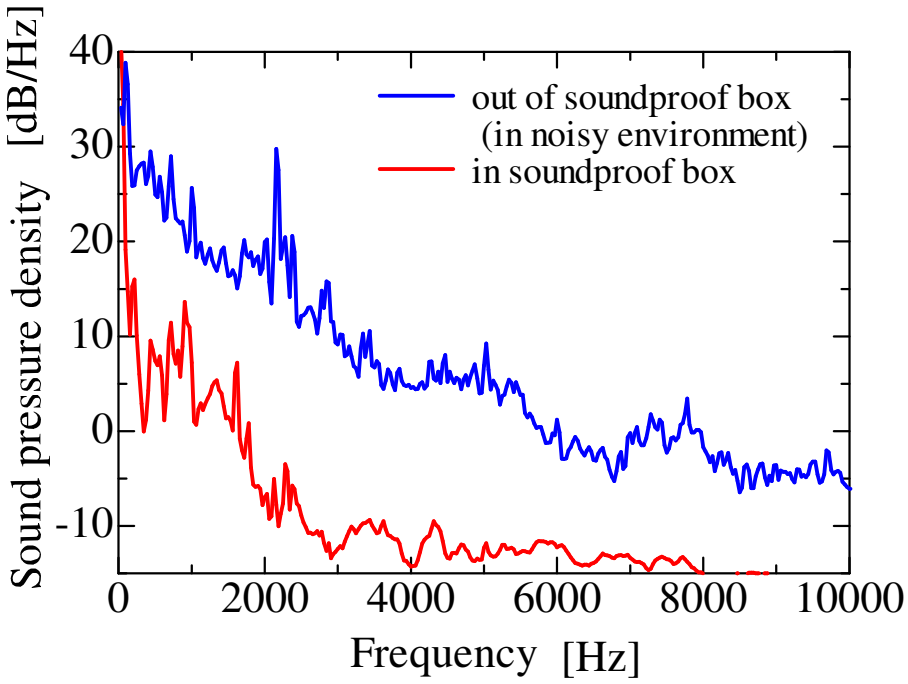

Figure 4-3 Sound pressure densities out of the soundproof box (blue line), namely in a noisy environment, and in the soundproof box (red line).

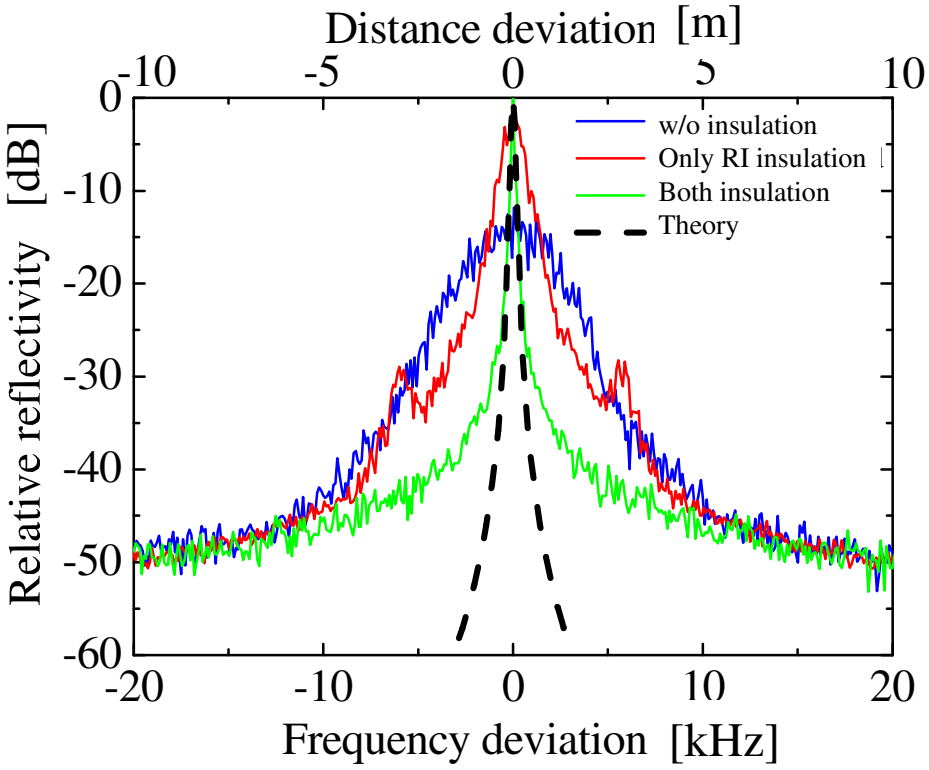

Figure 4-4 Measured and theoretical reflection shapes of 40 km-long FUT. The CRM was employed for all measured shapes. The reflectivity is normalized by the peak value of both insulated result. The upper and lower horizontal axes show distance deviation and frequency deviation, respectively.

From the above results, it is clear that the laser phase noise compensation scheme with the CRM works almost ideally even over a 40-km range with the sixteen-fold concatenation. Moreover, the remaining noise after the compensation process is mainly caused by environmental acoustic perturbation acting on an optical fiber, here the FUT and the reference interferometer, rather than some kind of numerical error in the compensation process with the CRM even with the sixteen-fold concatenation.

Note that there was difference from the theoretical shape in the region below −25 dB even though both the FUT and the reference interferometer were insulated and the CRM worked well (green line in Fig. 4-4). Three reasons were assumed for the remaining noise. The first is the deviation from the best compensation position. As mentioned in chapter 2, the CRM achieves its maximum effect when $N\tau_{ref}$ equals τ_{FUT}. If the deviation becomes longer, the phase noise remains. However, the deviation of a 40 km-long FUT is only 95 m corresponding to a deviation of 2 % from L_{ref}. Therefore, this is not a dominant cause of the remaining noise. The second reason is the error in the τ_{ref} value used for the numerical compensation process. Figs. 4-5(a), (b), and (c) show reflection shapes at 40 km when τ_{ref} = 24545 (measured value), 24550 (error of 5 ns from the measured value) and 24595 ns (error of 50 ns from the measured value) to the numerical compensation process, respectively. Periodic spikes were observed, which originated from the deviation from the true value of τ_{ref}. The levels of these spikes increased when the τ_{ref} error increased. On the other hand, the spectrum shapes around the reflection were in almost complete agreement when the error was within 50 ns. Hence, τ_{ref} was measured with sufficient accuracy and the error was not a dominant cause of the remaining noise although it causes the periodic spike. The third reason is residual acoustic perturbation. Even if both the FUT and the reference interferometer were insulated, it would be very difficult to eliminate acoustic noise completely because the insulation of our soundproof box was imperfect. In fact, as shown by the red line in Fig. 4-3, residual acoustic perturbation was observed although the sound level was lower. This residual perturbation causes an increase in the acoustic phase noise, and so the measured shape is different from the theoretical shape even if both the FUT and the

reference interferometer are placed in the soundproof box. We presume that this is the dominant factor as regards the difference between the theoretical and measured shapes, namely the remaining noise.

The red line in Fig. 4-4 shows the reflection shape when only the reference interferometer was insulated. The broadening of the spectrum, namely the remaining noise, is due solely to the acoustic perturbation acting on the FUT because the laser phase noise was compensated for sufficiently with the CRM. In practical use, only the reference interferometer can be placed in the soundproof box under this insulation condition. Hence, the reflection shape shown by the red line corresponds to an obtainable reflection shape in the practical use. It also means that the dominant noise limiting the spatial resolution of final results obtained by PNC-OFDR is the acoustic noise acting on the FUT, and so it is quite effective to employ the soundproof box to PNC-OFDR configuration.

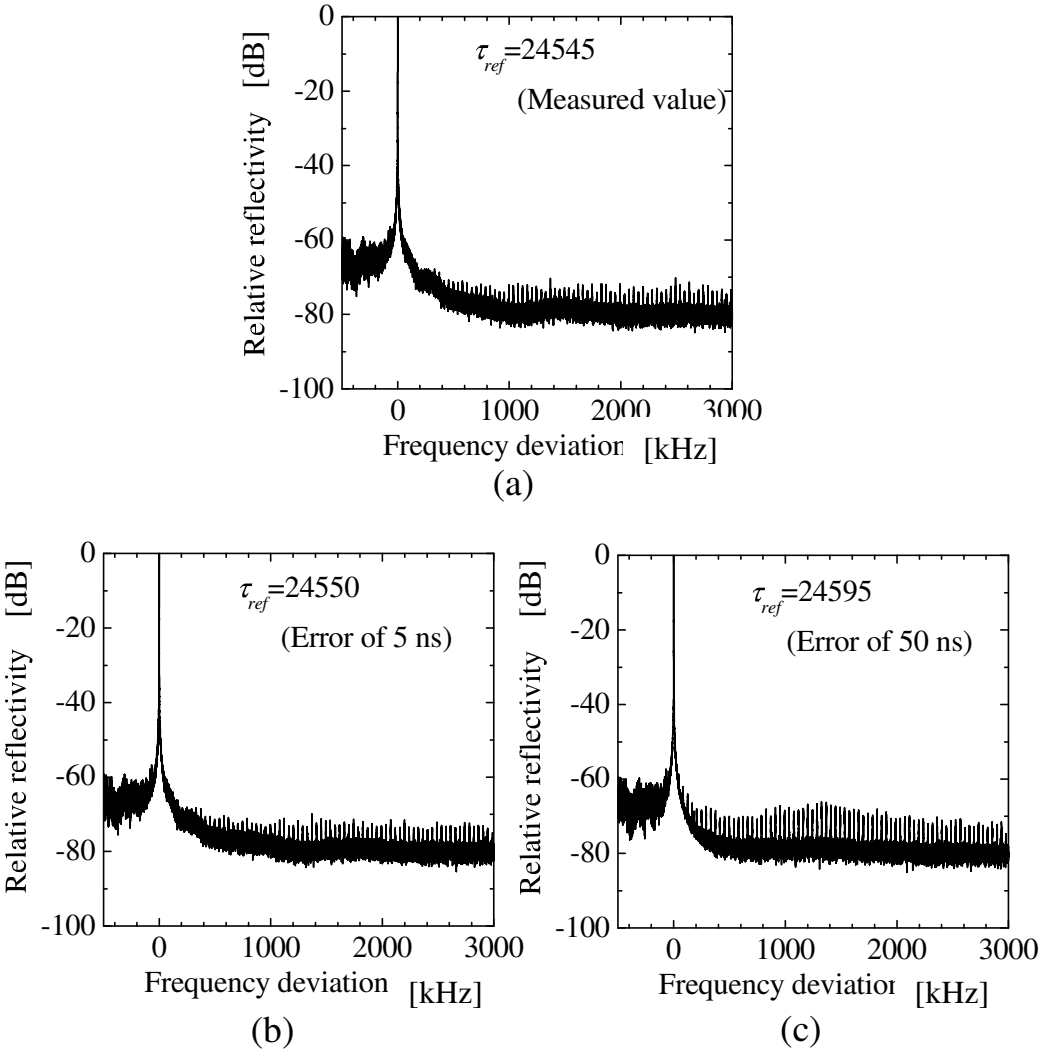

Figure 4-5 Spectrum shapes of a 40 km-long FUT with delay τ_{ref} of (a) 24545 (measured value), (b) 24550 (error of 5 ns from measured value), and (c) 24595 ns (error of 50 ns from measured value).

4.4. Laser phase noise and environmental acoustic noise

The CRM compensates only for the laser induced phase noise, and so if environmental acoustic noise is more dominant than the laser phase noise, the CRM is not effective in improving the spatial resolution. Therefore, in this section, we attempt to determine which noise is dominant before employing the CRM.

We compare the following two cases

.

a) Case #1 (Laser phase noise dominant)
   - Both the FUT and the reference interferometer were placed in the soundproof box.
   - The CRM was not used.

b) Case #2 (Acoustic noise dominant)
   - Only the reference interferometer was placed in the soundproof box.
   - The CRM was used.

Consequently, in case #1, both the FUT and the reference interferometer were insulated from the effects of the acoustic perturbation, and only the laser phase noise was observed. In case #2, the laser phase noise was eliminated by the CRM, and only acoustic noise acting on the FUT was observed. Therefore, a comparison of the spectra obtained in case #1 and #2 corresponds to a comparison of the laser phase noise and the acoustic noise.

Figure 4-6 shows measurement results for 5, 10, 20 and 40 km-long FUTs under the two experimental conditions mentioned above. Focusing on the results of case #1, we see that the behavior of the laser phase noise agrees qualitatively with the well-known random walk model because its shape approached the Lorentzian when the FUT length increased. Note that the reflection shape for a 30 km-long FUT was similar to those for 20 and 40 km-long FUTs. Concerning the results of case #2, the red symbols in Fig. 4-7

show the spectrum bandwidth at −3, −10 and −20 dB for each FUT length. The bandwidth broadened when the distance to the reflection increased. This is due to the acoustic perturbation acting on the longer FUT. The bandwidth at −3 dB was no more than 0.6 kHz in these experiments. Moreover, the bandwidth was less than 3.9 kHz even at −20 dB. The bandwidth can be converted to the spatial resolution by $\Delta f = 2\gamma\Delta L/v_g$ (0.25 m/kHz) as shown by the right side axis in Fig. 4-7. Here, the spatial resolutions at 30 and 40 km should be double the indicated value because they were measured at $\gamma =$ 200 GHz/s (0.5 m/kHz). Hence, the spatial resolutions at −3dB at 5, 10, 20, 30 and 40 km were 6, 6.5, 6.5, 9 and 28 cm, respectively. Therefore, it can be found that the spatial resolution of a final result given by PNC-OFDR is mainly decided by the low frequency environmental acoustic noise. The side peaks observed at ±7 kHz disappeared when both FUTs were placed in the soundproof box, and so it is clarified that they were generated by the acoustic perturbation acting on the FUT.

A comparison between cases #1 and #2 shows that the laser phase noise played a more dominant role with respect to the spatial resolution than the environmental acoustic noise even when we used a highly coherent light source such as a fiber laser with the linewidth of 4 kHz. The full widths at half maximum at 40 km in case #1 and #2 were 6 and 0.6 kHz, respectively. Roughly speaking, if we use a laser with a tenfold better spectral purity, the spectral width of the laser phase noise becomes similar to that of the environmental acoustic noise. Although the future development of narrow linewidth lasers may change these conclusions, when using current commercial lasers with linewidths of several kHz, the laser phase noise is dominant. Therefore its compensation with the CRM is also significant in terms of improving the spatial resolution of long-range measurements using a C-OFDR technique.

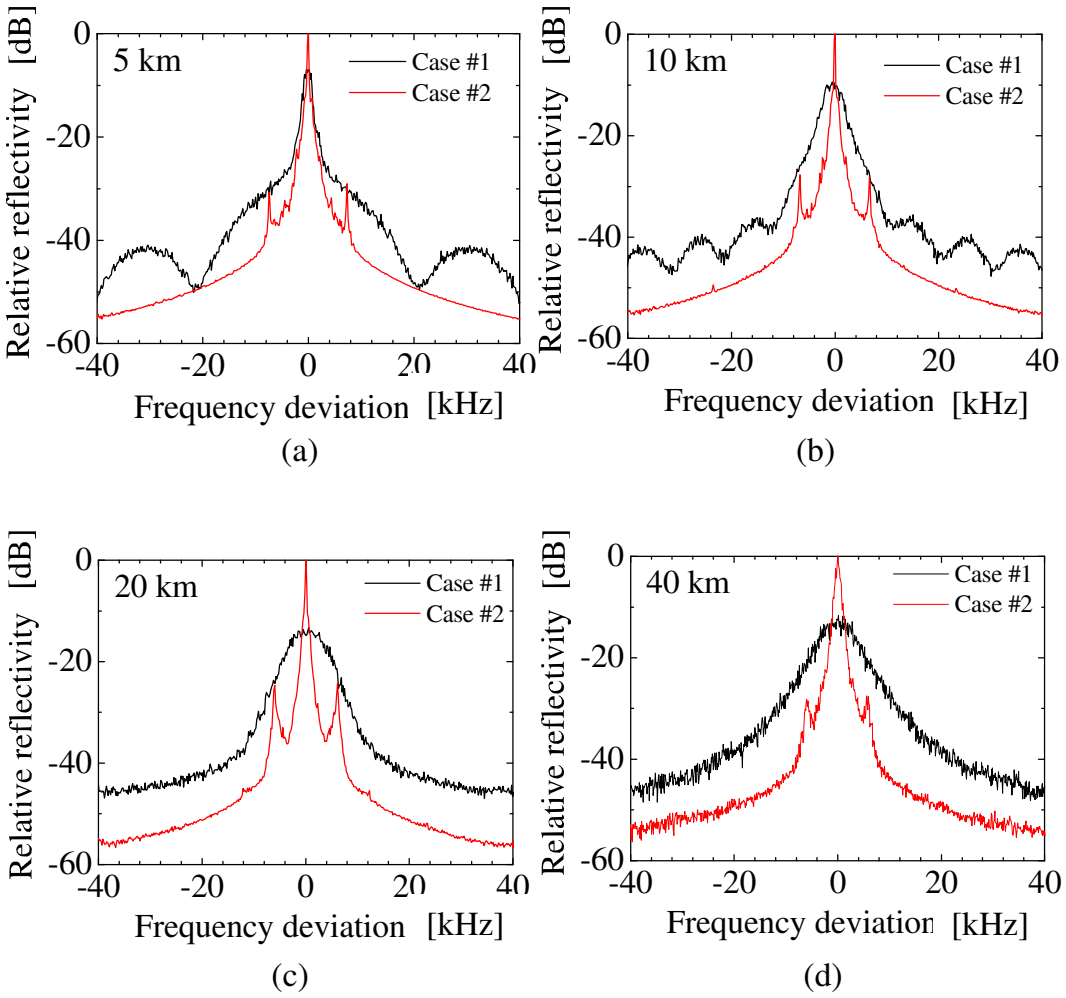

Figure 4-6 Spectra measured under two test conditions. The black lines show measurement results with an insulated FUT and reference interferometer, and without the CRM. The red lines show results with an insulated reference interferometer (the FUT was not insulated) and the CRM. The FUT lengths were (a) L_{ref} − 2 m (a km), (b) $2L_{ref}$ + 37 m (about 10 km), (c) $4L_{ref}$ + 61 m (about 20 km), and (d) $8L_{ref}$ + 95 m (about 40 km).

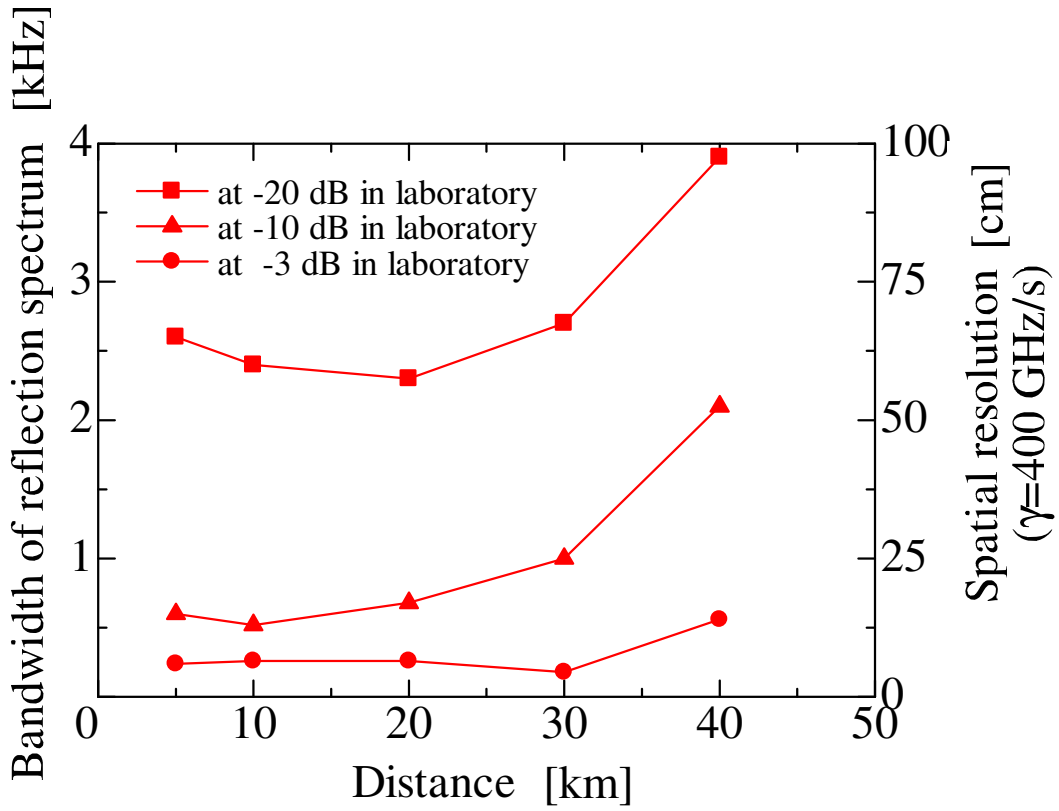

Figure 4-7 Spectrum bandwidth and spatial resolution at −3, −10, and −20 dB obtained in a laboratory environment. Note that the spatial resolutions at 30 and 40 km should be double the indicated values because they were measured at γ= 200 GHz/s.

We also investigated the influence of actual acoustic perturbation to confirm the PNC-OFDR performance in the field. An FUT consisting of an optical cable installed in an underground duct was measured at γ= 200 GHz/s. The cable was about 660 m long. Turned-back fiber lines were constructed for a long-range measurement by connecting some optical fibers in the cable. Consequently, the total lengths of the fiber lines were L_{ref} − 210 m (about 5 km), $2L_{ref}$ + 110 m (about 10 km), and $4L_{ref}$ + 100 m (about 20 km). The obtained bandwidths of the reflection spectra at each fiber length are shown by blue symbols in Fig. 4-8. The maximum bandwidths at −3 and −20 dB were 0.7 and 2.1 kHz, respectively. The spatial resolution at −3 dB was 36 cm. As an example, reflection shapes at 20 km, which were measured in our laboratory (red line) and in the actual field (blue line), are also shown in Fig. 4-9. As can be seen, there was no significant broadening of the reflection shapes although the low frequency component had a slight influence. This means that the spatial resolutions obtained for both cases were about the same when the same sweep rate γ was used. This indicates that PNC-OFDR maintains its performance even when it is used in the field.

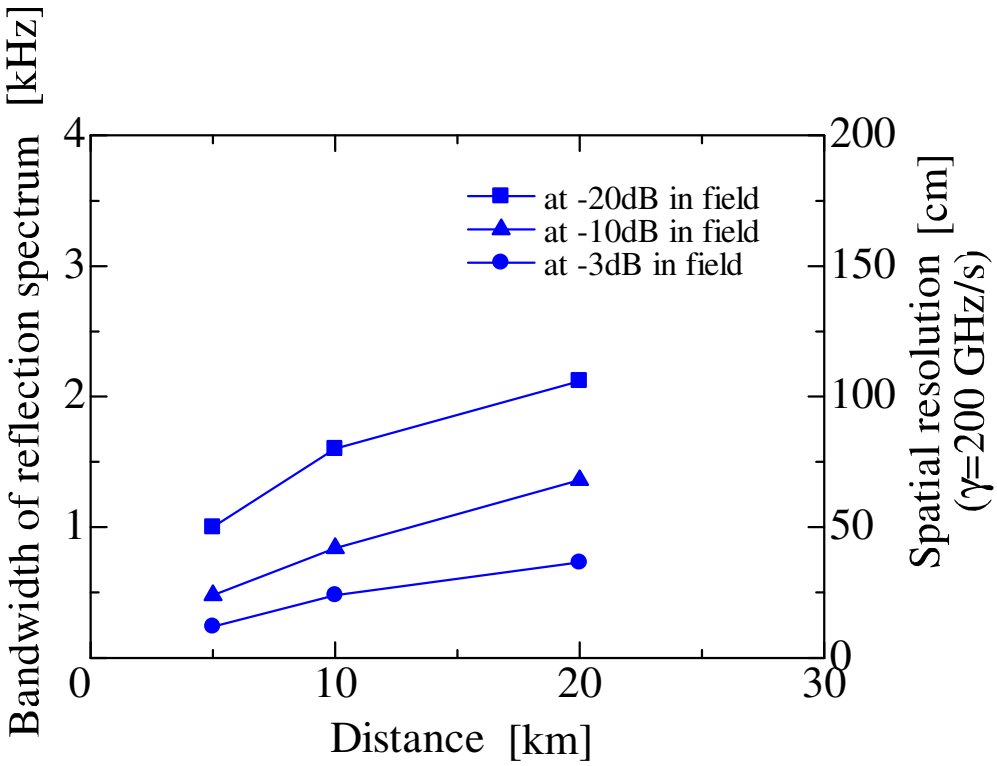

Figure 4-8 Spectrum bandwidths and spatial resolutions at −3, −10 and −20 dB obtained in the field.

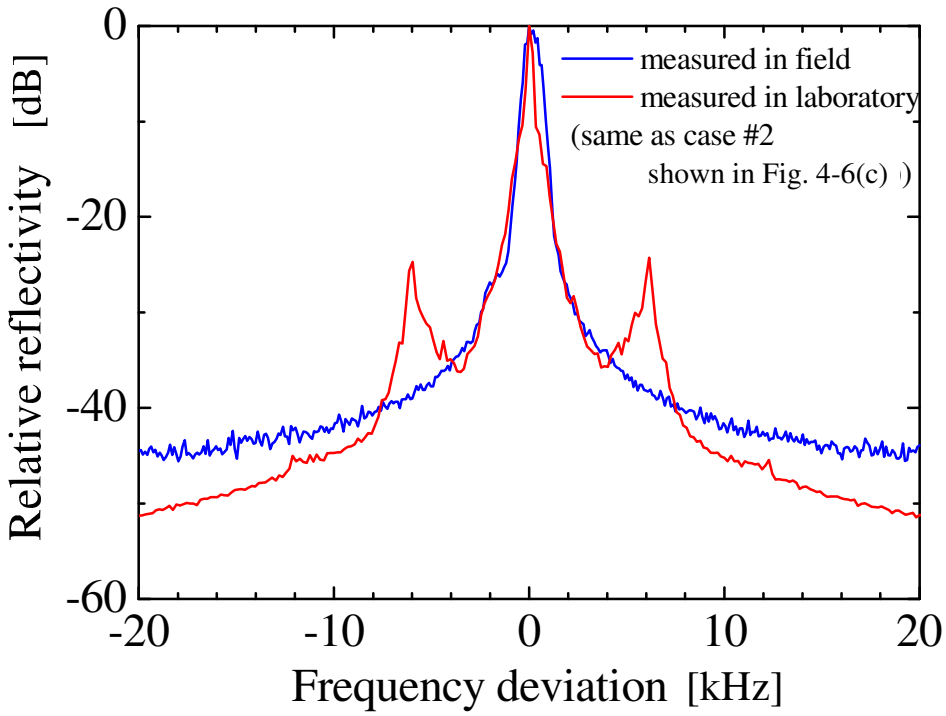

Figure 4-9 Reflection shapes at 20 km, which were measured in our laboratory and actual field.

4.5. Conclusion

A basic configuration of PNC-OFDR employing the CRM and the high coherent broadband tunable light source was demonstrated. It was clarified that the dominant noise limiting the spatial resolution of PNC-OFDR with the CRM for the laser phase noise compensation was acoustic noise caused by environmental acoustic perturbation acting on the FUT. It was demonstrated that when both the reference interferometer and the FUT were insulated against acoustic noise, the phase noise compensation scheme functioned well over a 40 km range, with sixteen-fold concatenation. This result reveals that the coherence length requirement for the light source is not very strict, and we can realize mid-range C-OFDR even with an inexpensive optical source.

It was also indicated experimentally that the dominant noise before the phase noise compensation was the laser phase noise rather than acoustic noise even when the fiber laser with a narrow line width of a few kHz was used. This makes the laser phase noise compensation with the CRM is very significant as regards improving the spatial resolution for long-range measurement.

The performance during field use was also investigated. There was no great degradation in the performance, and so PNC-OFDR can be used for various applications targeting mid- to long-range networks with a narrow spatial resolution, which cannot be achieved with other reflectometry technique.

5. Enhancement of frequency sweep span with 3rd-order optical modulation sideband

5.1. Introduction

A broader optical frequency sweep span is needed to improve the spatial resolution of PNC-OFDR. The optical frequency sweeping in PNC-OFDR is realized by sweeping a 1st-order optical modulation sideband generated by an external modulator as described in chapter 3. In this case, the optical sweep span is equivalent to that of the RF signal input into the modulator. However, it is difficult to realize wideband and linear sweeping of a high-frequency signal because of the limitation by the quality of the RF signal input into the modulator. With the commonly used RF synthesizer, it is difficult to sweep the RF signal frequency over a bandwidth of more than a few GHz without signal interruption owing to the switching of various electrical modules in the synthesizer. The CRM does not work well with such signal interruptions, and so a light source phase noise is not compensated for. Therefore, the theoretical spatial resolution of PNC-OFDR has been limited to several cm because of the sweep span of a few GHz.

In this chapter, a new scheme for improving the spatial resolution by expanding the optical frequency sweep span of PNC-OFDR is proposed [5-1]. Section 5.2 theoretically describes the principle of a 3rd-order optical modulation sideband sweeping. It is realized by employing two LN-IMs arranged in series as the external modulator for the tunable light source. And the optical frequency sweep span becomes three times broader than that of the 1st-order sideband. Based on the scheme, in section 5.3, sub-cm spatial

resolution measurement over a 10 km range with PNC-OFDR adopting the 3rd-order sideband sweeping is demonstrated experimentally. Section 5.4 summarizes this chapter.

5.2. Principle of 3rd-order sideband sweeping

The conventional PNC-OFDR technique uses a 1st-order sideband for external frequency sweeping [5-2]–[5-4]. If we can use a higher order sideband as the test light, the spatial resolution will be improved because of the broader optical frequency sweep span. Two LN-IMs are arranged in series to generate only ±3rd-order sidebands as shown in Figure 5-1. First, the input lightwaves are modulated by RF signals of $\phi_1 \sin\Omega t$ and $-\phi_1 \sin\Omega t$, and also have a phase difference of zero radian by applying DC bias voltages at the first LN-IM. ϕ_1 is modulation index, and Ω is the angular frequency of the RF signal. Thus, when sidebands higher than 5th-order are neglected, the optical field output from the first LN-IM $E_{1out}(t)$ is expressed as

$$E_{1out}(t) = e^{j\omega t}\left\{J_0(\phi_1) + J_2(\phi_1)e^{j2\Omega t} + J_4(\phi_1)e^{j4\Omega t} + J_2(\phi_1)e^{-j2\Omega t} + J_4(\phi_1)e^{-j4\Omega t}\right\}, \quad (5\text{-}1)$$

where ω is the angular frequency of the lightwave, and $J_n(\phi_x)$ is a 1st-order Bessel function. Then, at the second LN-IM, the lightwaves are modulated by RF signals of $\phi_2 \sin\Omega t$ and $-\phi_2 \sin\Omega t$, and has a phase difference of π radians. ϕ_2 is modulation index. When sidebands higher than 3rd-order are neglected, the optical field output from the second LN-IM $E_{2out}(t)$ is given by

$$\begin{aligned} E_{2out}(t) &= E_{1out}(t)\left\{J_1(\phi_2)e^{j\Omega t} - J_1(\phi_2)e^{-j\Omega t}\right\} \\ &= e^{j\omega t}J_1(\phi_2)\left[\left\{J_0(\phi_1) - J_2(\phi_1)\right\}e^{j\Omega t} + \left\{J_2(\phi_1) - J_4(\phi_1)\right\}e^{j3\Omega t} + J_4(\phi_1)e^{j5\Omega t}\right. \\ &\qquad \left. + \left\{J_2(\phi_1) - J_0(\phi_1)\right\}e^{-j\Omega t} + \left\{J_4(\phi_1) - J_2(\phi_1)\right\}e^{-j3\Omega t} - J_4(\phi_1)e^{-j5\Omega t}\right]. \end{aligned} \quad (5\text{-}2)$$

Here, when ϕ_1=1.84, $J_o(\phi_1)$–$J_2(\phi_1)$=0. Therefore, the terms of ±1st-order sidebands in (5-2) disappear. Note that ±5th-order sidebands still exist but they are negligible because the ratio of the amplitudes of the ±5th and ±3rd-order sidebands $J_4(\phi_1)/\{J_2(\phi_1)-J_4(\phi_1)\}$ is 0.08 when ϕ_1=1.84. When applying this scheme to PNC-OFDR, Ω must be linearly swept with respect to time. Therefore, Ωt in (5-2) can be expressed

as $\Omega(t)=2\pi f_m t+\pi\gamma^2$, where f_m and γ are the initial value of the modulation frequency and the frequency sweep rate of the RF signal, respectively. Finally, the output of the optical field is simply given as follows;

$$E_{out}(t) = e^{j\omega t} J_1(\phi_2)[\{J_2(\phi_1) - J_4(\phi_1)\}e^{j(6\pi f_m t+3\pi\gamma t^2)} + \{J_4(\phi_1) - J_2(\phi_1)\}e^{-j(6\pi f_m t+3\pi\gamma t^2)}]. \tag{5-3}$$

In this way, only ±3rd-order sidebands are strongly generated and swept by a very simple configuration consisting of two LN-IMs. From (5-3), the optical frequency sweep rate and sweep span of the 3rd-order sideband become three times higher than that of the input RF signal. Therefore, the spatial resolution of PNC-OFDR with a 3rd-order sideband is three times greater than that of conventional PNC-OFDR employing 1st-order sideband for the optical frequency sweeping.

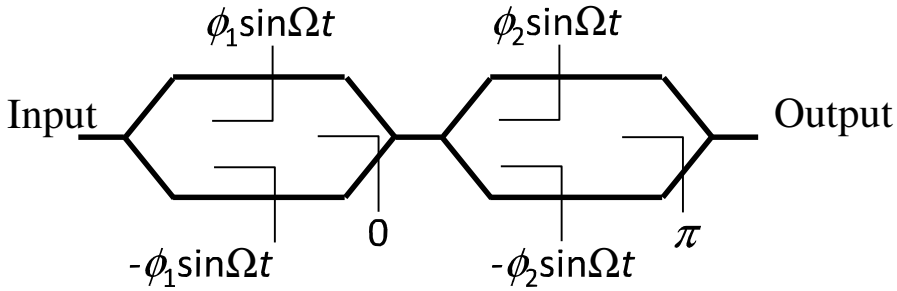

Figure 5-1 Configuration of intensity modulators for 3rd-order sideband sweeping.

5.3. Experiments and discussion

5.3.1. Experimental set-up

Figure 5-2 shows the experimental set-up for PNC-OFDR. We used a fiber laser with a narrow linewidth (Ethernal^{TM}, Orbits Lightwave, Inc.) as the optical source. The RF signal from the RF synthesizer was input into a 3rd-order sideband generator consisting of two LN-IMs throughout a phase shifter, which was used for adjusting the modulation timing, and swept from 10 to 16 GHz for a 23 ms acquisition time. Therefore, the frequency sweep rate γ of the RF signal was 260 GHz/s, and the frequency sweep span ΔF of the RF signal was 6 GHz. Based on the above discussion, the optical frequency sweep rate γ_{opt} and sweep span ΔF_{opt} of the 3rd-order sideband became 780 GHz/s and 18 GHz, respectively. Therefore, the theoretical spatial resolution Δz_{min} was improved to 5.5 mm by employing the 3rd-order sideband. The modulated lightwave was input into an optical filter to eliminate the −3rd-order sideband, and then we were able to obtain a single sideband spectrum, as shown in Fig. 5-3. Figures 5-3(a) and (b) show spectra when RF signals were 10 and 14 GHz, respectively. Although there were some peaks between each modulation sideband, they were negligible because their power was sufficient smaller than that of the 3rd-order sideband. The suppression ratio between the +3rd-order sideband and the other sidebands of the spectrum was 10-20 dB over the entire modulation bandwidth.

The modulated lightwave was divided and input into the main interferometer, which contained the FUT, and the reference interferometer. The reference interferometer with a 5 km-long delay fiber was used to compensate for the laser induced phase noise with the CRM. The delay fiber in the reference interferometer was placed in a soundproof box to insulate it from environmental acoustic noise [5-5]. In these experiments, the total sound level was 57 dB (14 mPa). The beat signals from the main and the reference interferometers were detected and then acquired with a 12-bit A/D at a sampling rate of 200 MHz. The beat signal data were sent to a personal computer for numerical

processing with the CRM [5-6]–[5-7]. FUTs were 5, 6.25, 7.5, 8.75 and 10 km long. The far ends of the FUTs were an angled physical contact connector (APC).

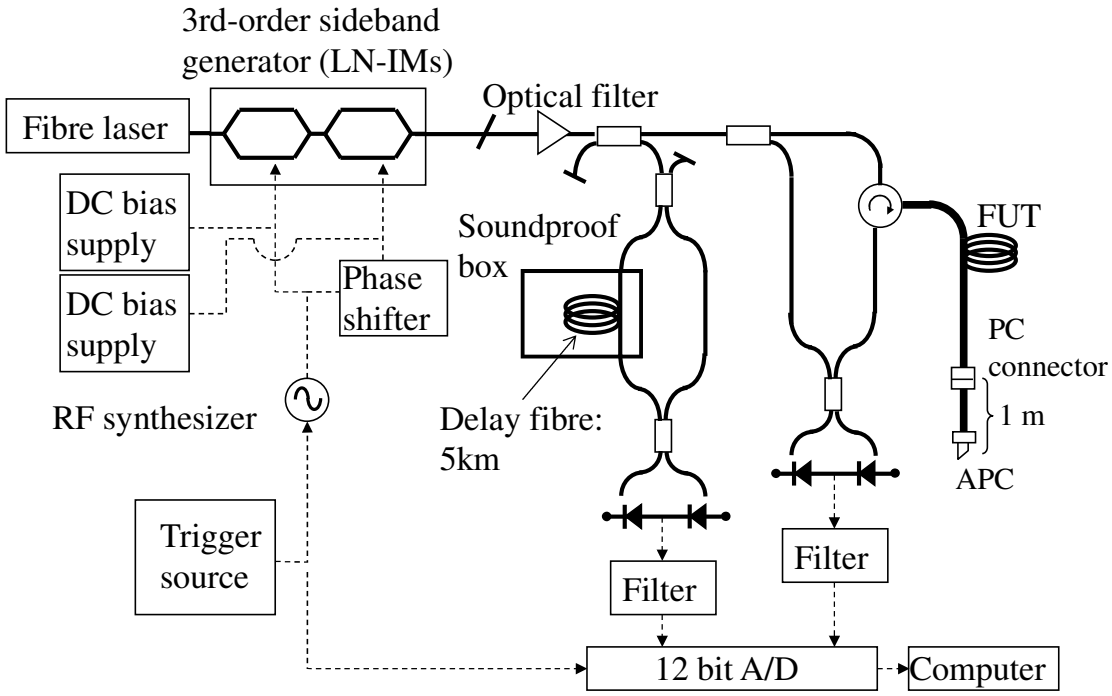

Figure 5-2 Configuration of PNC-OFDR employing 3rd-order sideband sweeping

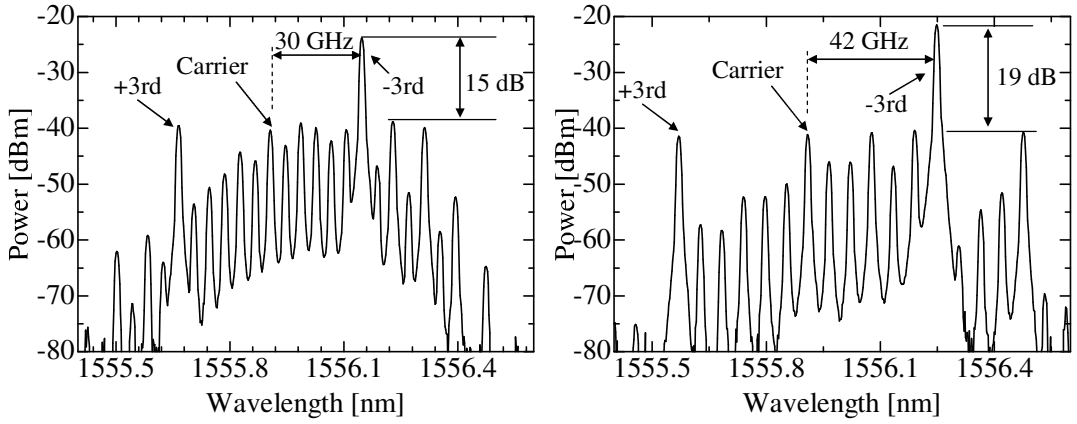

Figure 5-3 Spectra of lightwave output from 3rd-order sideband generator and optical filter. Modulation frequencies were (a) 10 GHz and (b) 14 GHz.

5.3.2. Experimental results and discussion

Figure 5-4 shows spectra of the reflection at 10 km. The red and blue lines show the reflection spectra with and without the compensation, respectively. These results were obtained by averaging ten spectra. By the compensation, the phase noise was considerably reduced, and the two reflections were clearly separated. After the compensation, the spatial resolution based on the FWHM was 8 mm. The CRM realizes the best compensation at integer multiple positions of the delay fiber length in the reference interferometer. In contrast, at the boundary positions of the compensated section, the effect of the compensation is degraded. In this experiment, 5, 7.5 and 10 km are the best compensation positions, and 6.25 and 8.75 km are boundary positions. Therefore, we investigated the spatial resolutions at those positions, as shown in Fig. 5-5. The spatial resolution under a sound noise level of 57 dB achieved a sub-cm spatial resolution over a 10 km range although the boundary positions were included. This means that the CRM worked very well over a 10 km range with 3rd-order sideband sweeping. Under a higher total sound level of 62 dB (22 mPa), the sub-cm spatial resolution was almost maintained with only the spatial resolution at 8.75 km reaching 150 mm. The sensitivity (relative to the Rayleigh backscattering level) was about −25 dB for all measurements.

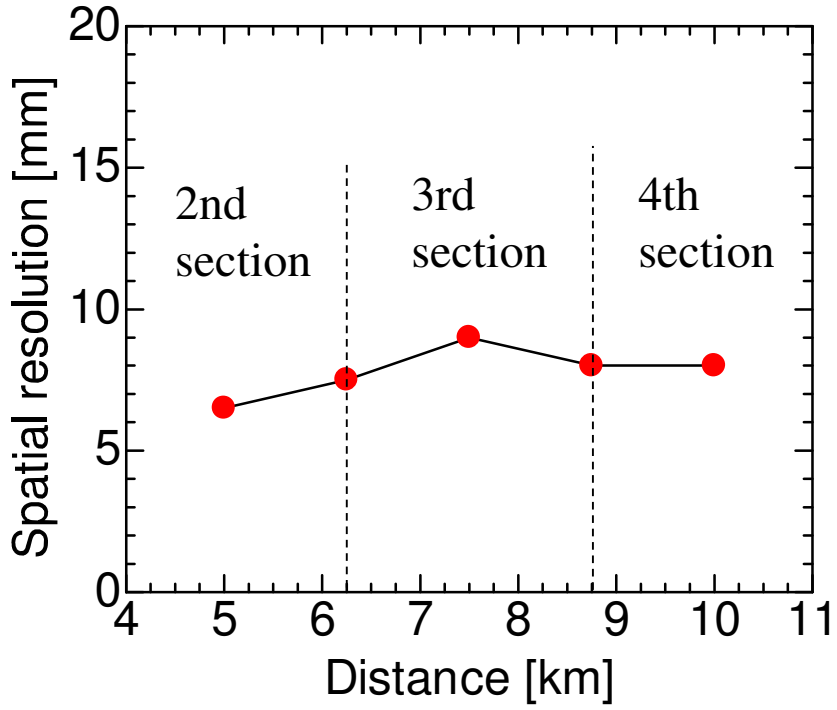

Figure 5-4 Reflection spectra around 10 km point.

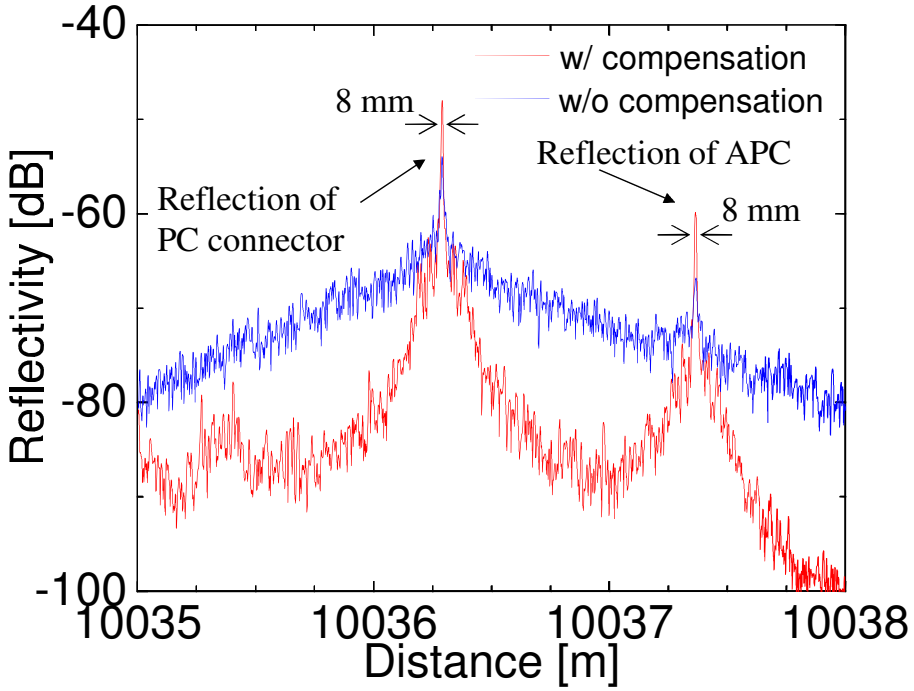

Figure 5-5 Spatial resolutions of reflection events at different distances.

5.4. Conclusion

It was theoretically derived that the 3rd-order sideband was generated by two LN-IMs arranged in series for a broader external frequency sweeping. It was experimentally confirmed that the optical frequency sweep rate and sweep span became 780 GHz/s and 18 GHz, respectively. Therefore, the theoretical spatial resolution was also improved to 5.5 mm. The achieved spatial resolution was sub-cm over a 10 km range. The sensitivity (relative to the Rayleigh backscattering level) was about −25 dB for all measurements.

6. Fading noise suppression and GVD compensation

6.1. Introduction

In previous chapters, the measurement range, the spatial resolution and sensitivity for PNC-OFDR were considered in detail. The measurement accuracy is also one of important performances for diagnosing optical fiber networks. In particular, when using reflectometry with a coherent detection scheme, the coherent speckle noise (or fading noise) in Rayleigh backscattering degrades the measurement accuracy [6-1]. However, no effective countermeasures have been reported in PNC-OFDR for dealing with the fading noise, and so the relative accuracy of the backscattering level has yet to be evaluated. The fluctuation of obtained Rayleigh backscattering level by the fading noise degrades the accuracy of an optical loss measurement between two positions undertaken for fiber network maintenance.

To suppress the fading noise in coherent reflectometry, a method called FSAV is usually used [6-2], [6-3], where uncorrelated measurements, i.e., measurements with different optical spectra, are incoherently averaged. Consequently, the wavelength of the probe lightwave must be varied for each measurement, and a broader tunable range gives a better effect on FSAV. C-OFDR requires linear sweeping of the probe lightwave when performing a reflectometry measurement. Hence, when employing FSAV in C-OFDR, the required tunable range of the light source is the C-OFDR sweep span multiplied by the averaging number. Due to this requirement, when FSAV was adopted, the achieved resolution was only 10 cm in [6-4] because the available sweep span for

PNC-OFDR was limited to only 2 GHz. This restriction arises from the narrow tunable range (60 GHz) of the fiber laser used in the experiment. Therefore, the laser with both wideband tunability and narrow linewidth is required if we need high resolution and low fading noise simultaneously.

Moreover, we should consider the deterioration of the spatial resolution caused by the GVD [6-5]–[6-7], when conducting such measurements with a broad lightwave bandwidth to suppress fading noise. In [6-7], the influence of the GVD is compensated for by sampling the detected signal with a non-equidistant clock reflecting the GVD effect.

As presented above, the previously reported PNC-OFDR has achieved narrow spatial resolution and measurement range needed for use in optical network diagnostics. However, considerations on the measurement accuracy of Rayleigh backscattering level have been insufficient, and so it is needed to consider countermeasures to the fading noise for practical use.

In this chapter, a PNC-OFDR employing an optical comb light source that provides a 675-GHz bandwidth tunability for fading noise reduction is described [6-8]. Section 6.2 presents the theoretical background of FSAV. Section 6.3 explains experimental setup to realize this highly accurate (low fading noise and high spatial resolution) PNC-OFDR. Section 6.4 demonstrates PNC-OFDR with a 2-cm spatial resolution and a 0.6-dB relative accuracy over a 10.4 km-long single mode fiber (SMF) with observable second-order GVD. Section 6.5 theoretically describes PNC-OFDR realized by incorporating the GVD compensation scheme in the phase noise compensation process, resulting in the simultaneous compensation of the phase noise and GVD induced by wideband measurement and dispersive media.

6.2. Theoretical background of fading noise suppression

The measurement accuracy of the Rayleigh backscatter level, namely its standard deviation, can be calculated theoretically as follows [6-2], [6-3].

$$\sigma = 10\log_{10}\left(1+\sqrt{\frac{3}{2m}}\right), \tag{6-1}$$

where m is an uncorrelated measurement number used for FSAV. Hence, if we require a standard deviation of less than 0.6 dB, we need an averaging process that uses about 70 uncorrelated measured traces. Moreover, the frequency sweep range corresponding to a 1-cm spatial resolution is more than 10 GHz per single measurement, and so the total bandwidth required for PNC-OFDR with a low fading noise (~0.6 dB) and a high spatial resolution (~1 cm) is about 700 GHz.

On the other hand, with such a wide band measurement, the GVD degrades the spatial resolution. When the measured fiber has a second-order GVD of β_2, the propagation of the test lightwave yields a delay time variation of $\Delta\tau=L\beta_2\Delta\omega$, where $\Delta\omega$ is the measurement bandwidth, and L is the round-trip length of the FUT. For example, if a bandwidth of 700 GHz is used for testing 10 km-long standard SMF, the spatial resolution is degraded to ~20 cm.

PNC-OFDR can compensate for the degradation in resolution caused by GVD by using a reference fiber interferometer with an identical GVD to the FUT, or by introducing non-equidistant resampling according to the difference between their GVDs. Using the GVD compensation described in [6-7] as a basis, in section 6.5 we discuss the details of the GVD compensation scheme in PNC-OFDR with the CRM.

6.3. Experimental setup of low fading noise and high spatial resolution PNC-OFDR

In terms of commercial products, the tunable range of such a laser is less than several tens of GHz, and so it is insufficient for FSAV. Therefore, to obtain a broader tunable range, an optical comb light source using a narrow linewidth laser as the seed lightwave was employed. This scheme also uses a tunable optical bandpass filter to select a single spectral line from the optical comb to perform a single PNC-OFDR measurement. This process is then repeated with each spectral line individually. Next, all the OFDR measurement results obtained with different spectral lines are averaged. The test wavelength with the selected spectral line has good coherency, which is the same as that of the seed lightwave, namely the lightwave from the narrow linewidth laser. Consequently, we can obtain a light source with both broad tunable range and high coherency for PNC-OFDR.

The experimental setup is shown in Fig. 6-1(a). A narrow linewidth fiber laser (Koheras Adjustik^{TM}) was used as the seed laser. The frequency comb generator described in [6-9] was used to generate a frequency comb consisting of 27-line spectra with a 25-GHz interval, resulting in a total bandwidth of 675 GHz. The flatness of the generated comb was better than 5 dB. A single spectral line extracted by a tunable optical bandpass filter (Finisar Waveshaper 1000E) was used for the OFDR measurement. The spectrum of the generated comb and the extracted single line spectrum are depicted in Fig. 6-1(b). The suppression to the unwanted spectral lines was greater than 50 dB.

The optical frequency of the lightwave of the extracted spectral line was swept linearly with an external SSB-SC modulator by sweeping the input RF signal frequency [6-10]. The sweep range ΔF was set at 13 GHz (2 to 15 GHz) by expanding the sweep range of the original RF signal (5.1 to 6.73 GHz) provided by an Agilent E8257D with a frequency multiplier (×8) and a down converter. This sweep range provides a theoretical spatial resolution of $c/2n\Delta F \approx 8$ mm. The sweep rate $\gamma$was 800 GHz/s. The frequency

swept lightwave was amplified with an EDFA, and then used as a test and a local lightwave for the PNC-OFDR measurement. The power of the test lightwave input into the FUT was about 0 dBm.

A reference interferometer with an L_{ref} = 5 km long SMF (delay τ_{ref} = 25 μs) was used to obtain the reference signal for the compensation for the phase noise and GVD. The phase noise compensation is accomplished individually for each $L_{ref}/2$ long section of FUT. When the round-trip distance of the measurement point equals to L_{ref}, namely $z = NL_{ref}/2$, where N is an integer, the compensation works ideally; in principal, the light source phase noise can be completely compensated for. Around the boundary of the compensation section ($z = NL_{ref}/2+L_{ref}/4$), the compensation effect is small but it is still effective if $L_{ref}/2$ is set at less than the coherence length of the light source. Also, for GVD compensation, the GVD parameter of the delay fiber in the reference interferometer was identical to that of the FUT (SMF), which was -2.16×10^{-26} s^2/m (corresponding to 17 ps/nm/km).

Polarization diversity was employed to eliminate polarization sensitivity. The beat signals from both the measurement and the reference interferometers were detected with double balanced receivers and then acquired with a 12-bit A/D at a sampling rate of 200 MS/s. The obtained data were stored in a personal computer for the phase noise compensation process.

After the above measurement had been completed once for all 27 spectral lines of the comb, the laser frequency was changed by thermally tuning the laser cavity by 12.5 GHz, and another 27 PNC-OFDR measurements were performed with 27 new spectral lines of the new comb. Since the comb interval was double the PNC-OFDR frequency sweep range, with the above procedure, we obtained 54 spectrally separated measurements, namely 54 uncorrelated speckles to be used for FSAV.

It has been found that the environmental sound level affects PNC-OFDR measurements [6-11]. Therefore, the reference interferometer was placed in a soundproof box to isolate the acoustic vibration of the fiber caused by the environmental sound. On the other hand, FUT was wound on a bobbin and placed in an

environment where the sound level was 62 dB (22 mPa) (the loudest place in our laboratory).

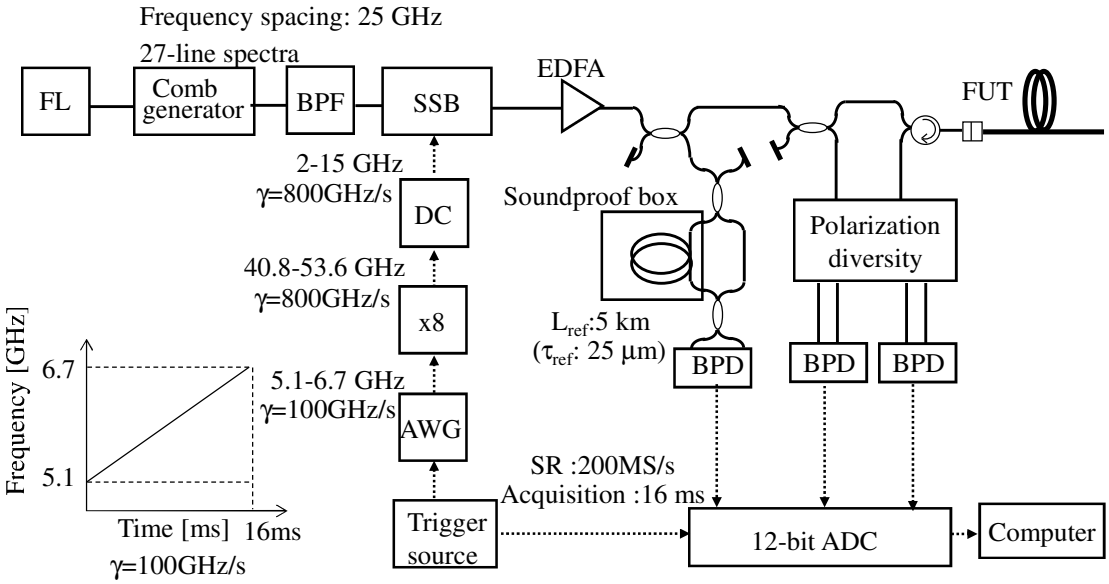

(a)

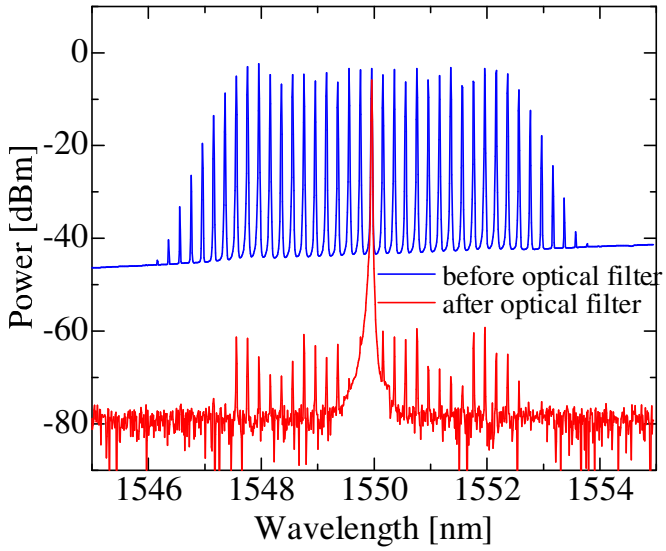

(b)

Figure 6-1 (a) Experimental setup. FL: Fiber laser, BPF: Tunable optical bandpass filter, SSB: SSB-SC modulator, AWG: Arbitrary waveform generator (Agilent E8257D), ×8: Frequency multiplier, DC: Frequency down converter, FUT: Fiber under test, BPD: Balanced receiver, A/D: Analogue-to-digital converter and SR: Sampling rate. (b) Optical spectra of frequency-comb before and after optical bandpass filter.

6.4. Performance of fading noise suppressed PNC-OFDR

Figure 6-2(a) shows samples of the obtained PNC-OFDR trace for a 10.4 km-long FUT after averaging the 54 measurements each at a different comb spectral line. All the observed reflection events inside the fiber correspond to the connection points with physical contact connectors, whose reflectivity was about 50 dB, at distances of 5, 5.5, and 10.4 km. All the reflections were clearly observed and the sensitivity was also 25 dB below the Rayleigh backscattering level.

Figure 6-2(b) shows the details of the Rayleigh backscatter signal at 10 km in Fig. 6-2(a). The standard deviation of the Rayleigh backscatter level after employing FSAV was about 0.6 dB throughout all the experiments. Figure 6-3 shows the relation between the uncorrelated measurement number and the standard deviation of the Rayleigh backscatter level. The solid line shows theoretical values calculated by using (6-1). The solid circle in Fig. 6-3 is the experimentally obtained standard deviation. This value was in good agreement with FSAV theory. This proved that the optical comb approach is effective for suppressing fading noise in PNC-OFDR employing the narrow linewidth laser.

We attributed the small difference between the measured and theoretical values to the sound vibration of the FUT. The correlation between measured Rayleigh speckle patterns decreased because of the spatial averaging effect caused by the fiber vibration. Averaging using measurement results with this decreased correlation gave us a standard deviation for the Rayleigh backscatter level, which was smaller than the theoretical value. The open circle in Fig. 6-3 shows the measurement result we obtained when the FUT was insulated from the acoustic vibration by being placed in a soundproof box. The open and solid squares, respectively, show results obtained with and without FUT insulation with another averaging number. The results with FUT insulation were in good agreement with the theoretical value. In contrast, the results without insulation were different from the theoretical values. Therefore, we revealed that the fading noise was suppressed more by the influence of the environmental sound vibration of the FUT.

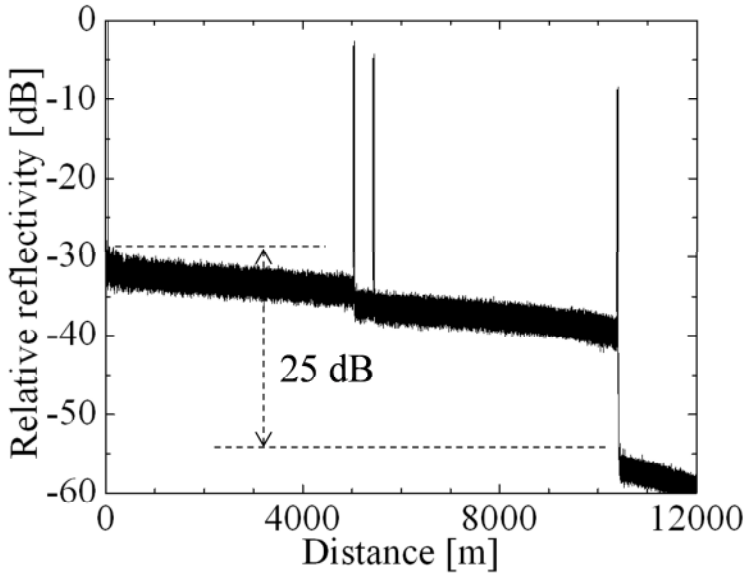

(a)

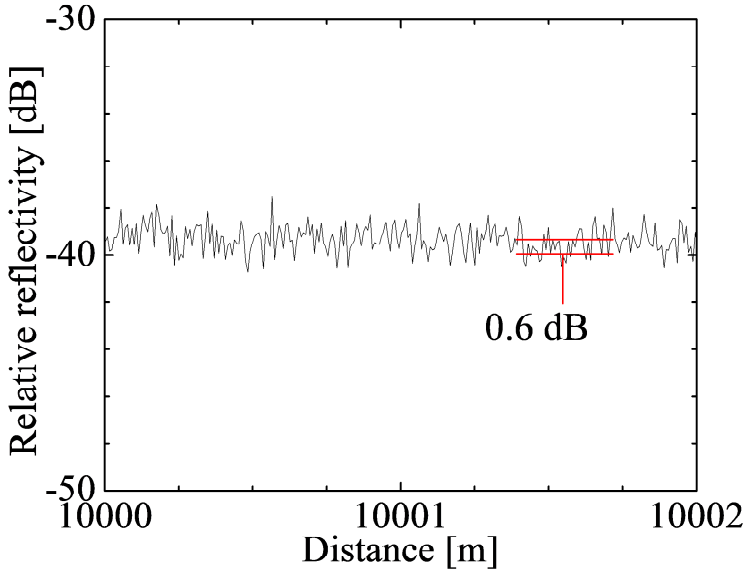

(b)

Figure 6-2 (a) Obtained OFDR trace for a 10.4 km-long FUT. (b) Details of the Rayleigh backscatter signal at 10-km. The reference of the relative reflectivity is arbitrary

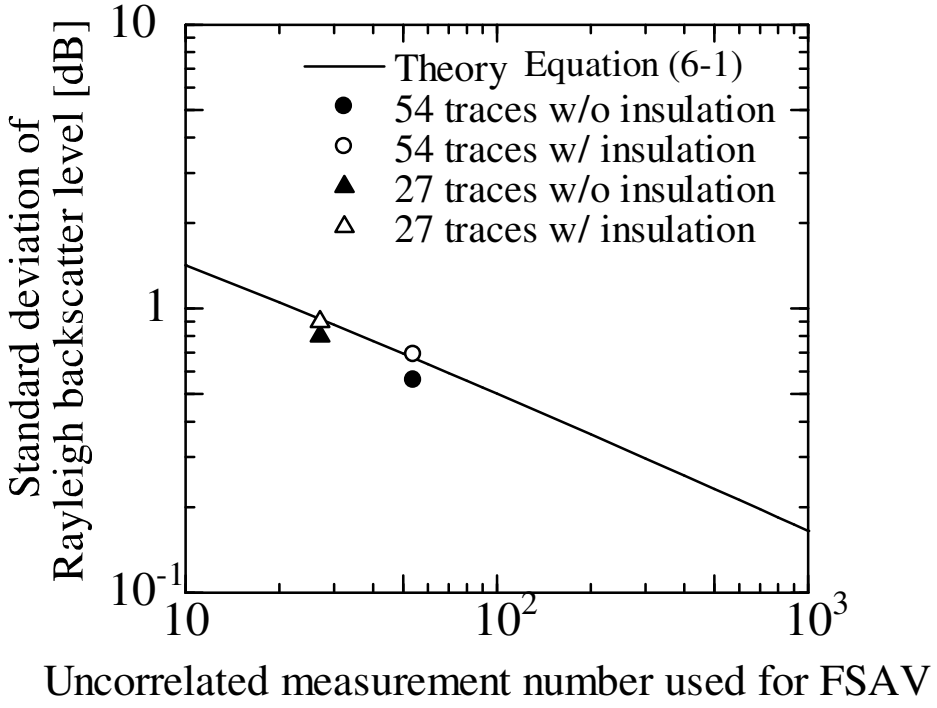

Figure 6-3 Relation between averaging number and relative accuracy of Rayleigh backscatter level.

Figures 6-4(a) and (b), respectively, show details of the trace at the 5 and 10.4 km (fiber end) reflection points in Fig. 6-2(a). The black lines show the results obtained with the phase noise and GVD compensations, while the red lines are those without compensation. The broadened reflection peaks shown by the red line are caused by the phase noise and GVD. By employing compensations, the achieved 3-dB spatial resolutions at 5 and 10.4 km were 9 and 19 mm, respectively. It can be seen clearly that the compensations for both the phase noise and GVD functioned well. We presume that the difference from the theoretical value of 8 mm is caused by the sound vibration of the FUT as described in chapter 4. A lightwave from a longer distance is exposed to the fiber vibration for a longer time, and so the spatial resolution at 10.4 km was poorer than that at 5 km. Figure 6-4(c) shows a measurement result for another FUT whose length was 8.75 km. This length is the boundary between the 3rd and 4th sections for the phase noise compensation. However, we were able to obtain a 2-cm spatial resolution although the effectiveness of the compensation theoretically degrades because of the section boundary.

Figure 6-5 shows the observed 3-dB resolution at various distances with compensation. These plots include results acquired with various FUTs that differ from those in Fig. 6-2, and show the average resolutions for three measurements (the error bars show the maximum and minimum values). A resolution of better than 2 cm was confirmed at every distance. The spatial resolution broadened when the distance to the reflection increased. This is due to the acoustic perturbation acting on the longer FUT [6-11]. As mentioned in section 6.2, when the broadband lightsource of 700 GHz is used for measuring 10 km-long SMF, the spatial resolution is degraded to ~20 cm by influence of GVD. However, such degradation was not found in all measurement results.

These experimental results mean that there was no deterioration in the PNC-OFDR performance caused by the broadband measurement of a dispersive medium because the simultaneous compensations for the phase noise and for GVD functioned well.

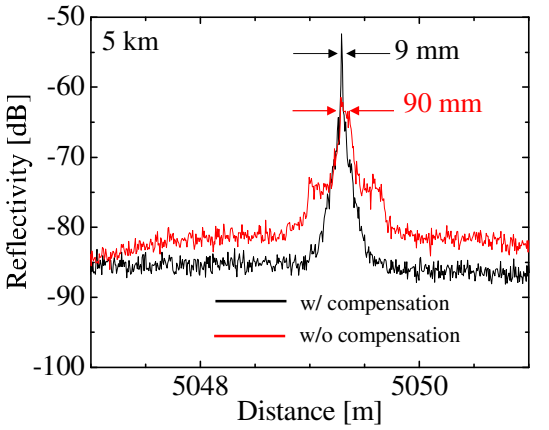

(a)

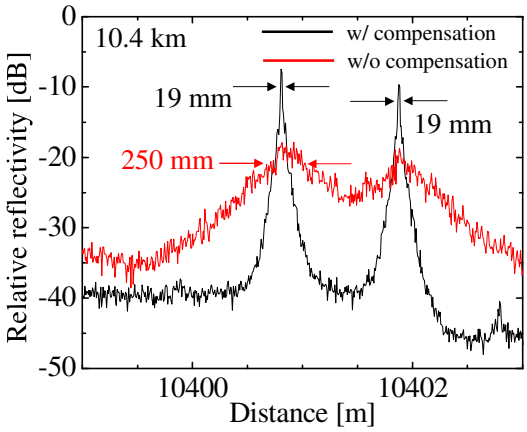

(b)

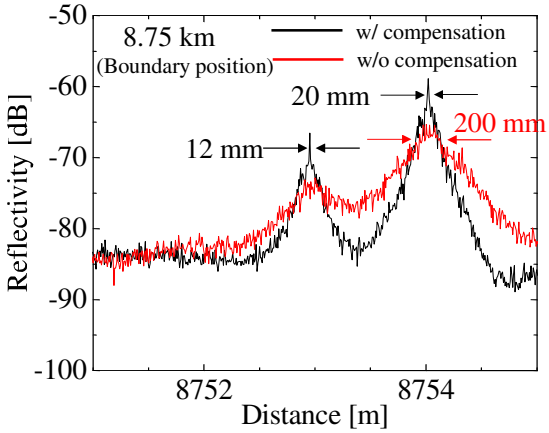

(c)

Figure 6-4 Details of the reflection peaks at (a) 5 km and (b) 10.4 km. (c) Reflection profile of an 8.75-km-long FUT (not the FUT shown in Fig. 6-2(a)). 8.75 km was the boundary between the 3rd and 4th sections. The reference of the relative reflectivity is arbitrary.

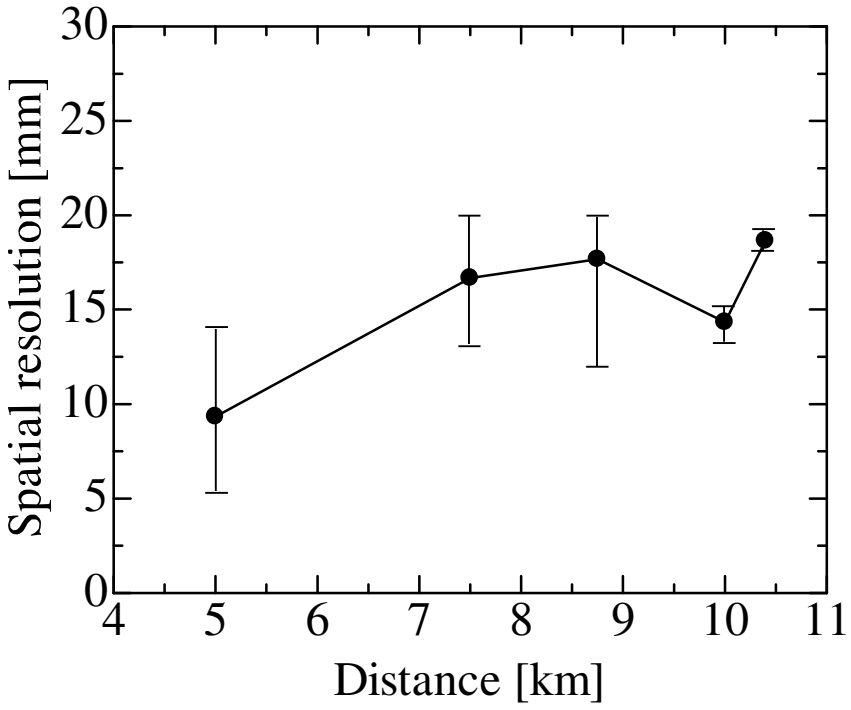

Figure 6-5 Spatial resolution at various distances.

6.5. Group velocity dispersion compensation scheme in PNC-OFDR

6.5.1. Theory of group velocity dispersion compensation for conventional C-OFDR

Firstly, we show theoretically the influence of GVD on the beat frequency when using conventional C-OFDR. The time behavior of the angular frequencies of the local light and the reflected light from the FUT is shown in Fig. 6-6. This includes the influence of the GVD, which depends on the GVD parameter of the FUT $\beta_2^{(F)}$. L_{FUT} is the round trip distance to a reflection point in the FUT. T is the total time for a full band sweep. ω_0 is the initial angular frequency of the test light. $\Delta\Omega$ and $\Delta\omega$ are angular frequencies swept with respect to times T and t, respectively. We also assumed that the GVD parameter is constant along the FUT and that the third-order dispersion is negligible ($\beta_3 = 0$). Here, the angular frequency of the local light $\omega_L(t)$ is given by

$$\omega_L(t) = 2\pi\gamma t + \omega_0, \tag{6-2}$$

where $\gamma$is the sweep rate of the angular frequency. Therefore, the electrical field of the local light is given by

$$E_L(t) \propto \exp j\Phi_L(t), \tag{6-3}$$

where

$$\Phi_L(t) = \pi\gamma t^2 + \omega_0 t. \tag{6-4}$$

When we consider that the time delay caused by the GVD τ_{GVD} to be given by

$$\tau_{GVD} = \beta_2^{(F)} \Delta\omega L_{FUT}, \tag{6-5}$$

the angular frequency of the reflected light from FUT $\omega_S(t)$ is given by

$$\omega_S(t) = \frac{2\pi\gamma}{2\pi\gamma\beta_2^{(F)} v_g \tau_0 + 1} t + \omega_0 - \frac{2\pi\gamma\tau_0}{2\pi\gamma\beta_2^{(F)} v}, \tag{6-6}$$

where v_g is the group velocity. τ_0 is the round trip time to a reflection point in the FUT ($\tau_0 = L_{FUT}/v_g$). The electrical field of the reflected light is given by

$$E_S(t) \propto \exp j\Phi_S(t), \tag{6-7}$$

where

$$\Phi_S(t) = \frac{\pi\gamma}{2\pi\gamma\beta_2^{(F)} v_g \tau_0 + 1} t^2 + \left(\omega_0 - \frac{2\pi\gamma\tau_0}{2\pi\gamma\beta_2^{(F)} v}\right) t. \tag{6-8}$$

From (6-3) and (6-7), the beat signal $i_{FUT}(t)$ is as follows,

$$i_{FUT}(t) \propto \cos\Phi_{FUT}(t), \tag{6-9}$$

where

$$\Phi_{FUT}(t) = \frac{-2\pi\gamma\tau_0}{2\pi\gamma\beta_2^{(F)} v_g \tau_0 + 1}\left(\pi\gamma\beta_2^{(F)} v_g t^2 + t\right). \tag{6-10}$$

Therefore, the beat frequency of the signal is expressed by

$$\omega_{FUT}(t) = \frac{d\Phi_{FUT}(t)}{dt} = \frac{-2\pi\gamma\tau_0}{2\pi\gamma\beta_2^{(F)} v_g \tau_0 + 1}\left(2\pi\gamma\beta_2^{(F)} v_g t + 1\right). \tag{6-11}$$

It can be clearly seen that the beat frequency of the reflected light from one reflection point is not constant but depends on the time t. This time dependence means a broadening of the reflection in the C-OFDR trace. This can also mean that a broader measurement bandwidth leads to the reflection shape being broadened by the GVD because $\gamma t = \Delta\omega$.

A compensation scheme for the GVD effect for conventional C-OFDR is described in [6-7]. This approach can be demonstrated by sampling the detected signal with a clock that reflects the GVD effect. This clock can be obtained by using a reference interferometer consisting of a delay fiber with the same GVD parameter as the FUT. Here, we describe that principle in detail theoretically. As with (6-11), The beat frequency of a reference signal obtained by the reference interferometer $\omega_{ref}(t)$ is as follows:

$$\omega_{ref}(t) = \frac{-2\pi\gamma\tau_1}{2\pi\gamma\beta_2^{(r)}v \quad +1}\left(2\pi\gamma\beta_2^{(r)}v_g t + 1\right), \tag{6-12}$$

where $\beta_2^{(r)}$ is the GVD parameter of the delay fiber used in the reference interferometer. τ_1 is the delay time between the two arms of the reference interferometer. The beat frequency of the resampled signal $\omega_r(t)$ is expressed by

$$\begin{aligned}\omega_r(t) &= \frac{\omega_{FUT}(t)}{\omega_{ref}(t)} \\ &= \frac{\tau_0}{\tau_1}\left(\frac{2\pi\gamma\beta_2^{(r)}v \quad +1}{2\pi\gamma\beta_2^{(F)}v_g\tau_0+1}\right)\left(\frac{2\pi\gamma\beta_2^{(F)}v_g t+1}{2\pi\gamma\beta_2^{(r)}v \quad +1}\right).\end{aligned} \tag{6-13}$$

In (6-13), the first bracket expresses the GVD effect which is developed by the deviation of the round trip time to a reflection point τ_0 from the delay time of the reference interferometer τ_1. The last bracket expresses the GVD effect which is induced by the measurement bandwidth because $\gamma t = \Delta\omega$. Here, the term in the first bracket is

negligible because $\left|2\pi\gamma\beta_2^{(r)}v_g\tau_1\right| < 10^{-7}$ and $\left|2\pi\gamma\beta_2^{(F)}v_g\tau_0\right| < 10^{-7}$ in most cases. Thus (6-13) becomes

$$\omega_r(t) = \frac{\tau_0}{\tau_1}\left(\frac{2\pi\gamma\beta_2^{(F)}v}{{}^{(r)}v}\right). \tag{6-14}$$

This shows theoretically that if $\beta_2^{(F)} = \beta_2^{(r)}$, the GVD effect vanishes and is compensated for by this approach.

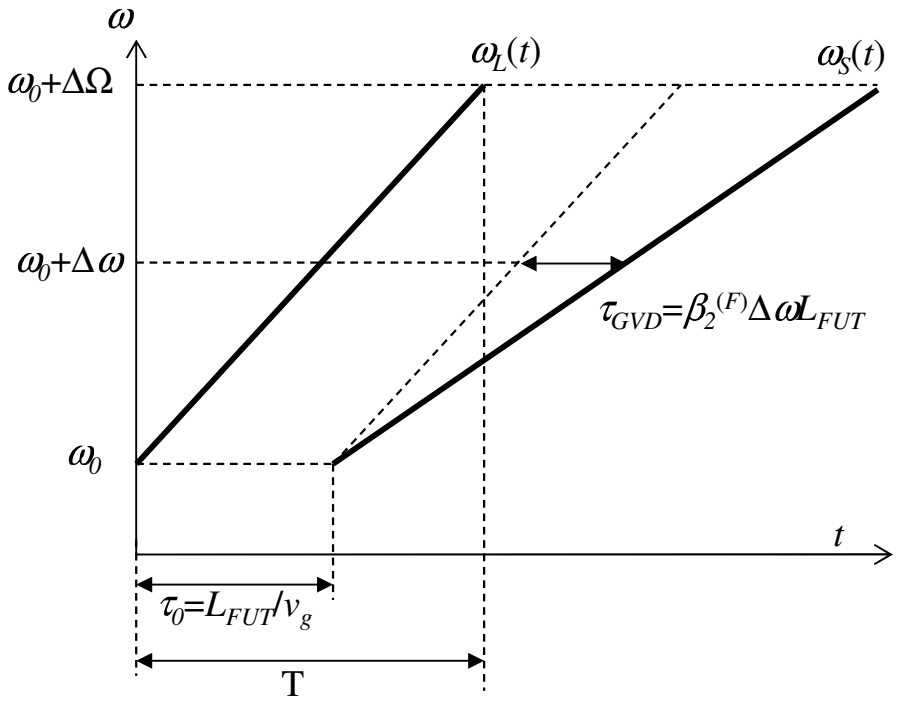

Figure 6-6 Time behavior of the angular frequencies of the local light and the reflected light from the FUT, which is influenced by the GVD.

6.5.2. Influence of group velocity dispersion on PNC-OFDR

In this section, we theoretically describe a scheme for the simultaneous compensation for GVD and the phase noise. As described in chapter 2, PNC-OFDR compensates for the phase noise by resampling a detected signal based on the phase $\Phi_{NPNC}(t)$ estimated by the phase noise compensation algorithm. The phase $\Phi_{NPNC}(t)$ is exactly the same as the phase $\Phi_{Nref}(t)$ obtained by a reference interferometer with a delay of $N\tau_1$ (N is integer). If the phase noise term is neglected for simplicity, the phase estimated by the algorithm is given by

$$\begin{aligned}\Phi_{NPNC}(t) &= \sum_{n=0}^{N-1} \Phi_{ref}(t - n\tau_1) \\ &= \frac{-2N\pi\gamma\tau_1}{2\pi\gamma\beta_2^{(r)} v_g \tau_1 + 1}\Big[\pi\gamma\beta_2^{(r)} v_g t^2 + t \\ &\qquad -(N-1)\pi\gamma\beta_2^{(r)} v_g \tau_1 t + C.C.\Big], \end{aligned} \tag{6-15}$$

where

$$\Phi_{ref}(t) = \frac{-2\pi\gamma\tau_1}{2\pi\gamma\beta_2^{(r)} v}\left(\pi\gamma\beta_2^{(r)} v_g t^2 + t\right). \tag{6-16}$$

Therefore, from (6-15), the beat frequency $\omega_{NPNC}(t)$ is given by

$$\begin{aligned}\omega_{NPNC}(t) = \frac{-2\pi\gamma N\tau_1}{2\pi\gamma\beta_2^{(r)} v_g \tau_1 + 1}\Big[2\pi\gamma\beta_2^{(r)} v_g t + 1 \\ -(N-1)\pi\gamma\beta_2^{(r)} v_g \tau_1\Big]. \end{aligned} \tag{6-17}$$

The beat frequency of the signal resampled by (6-17) $\omega_{rNPNC}(t)$ is expressed by

$$\omega_{rNPNC}(t) = \frac{\omega_{FUT}(t)}{\omega_{NPNC}(t)} = \frac{\tau_0}{N\tau_1}\left(\frac{2\pi\gamma\beta_2^{(r)}v}{{}^{(F)}v}\right)\left(\frac{2\pi\gamma\beta_2^{(F)}v_g t+1}{2\pi\gamma\beta_2^{(r)}v \quad +1-(N-1)\pi\gamma\beta_2^{(r)}v}\right). \tag{6-18}$$

Let us consider the beat frequency $\omega_{rNref}(t)$ of the signal resampled based on the phase $\Phi_{Nref}(t)$ which can be obtained by the reference interferometer with $N\tau_1$. The beat frequency $\omega_{rNref}(t)$ is simply given by replacing τ_1 with $N\tau_1$ in (6-13) as follows.

$$\omega_{rNref}(t) = \frac{\tau_0}{N\tau_1}\left(\frac{2\pi\gamma\beta_2^{(r)}v_g N\tau_1+1}{2\pi\gamma\beta_2^{(F)}v \quad +1}\right)\left(\frac{2\pi\gamma\beta_2^{(F)}v \quad +1}{2\pi\gamma\beta_2^{(r)}v_g t+1}\right). \tag{6-19}$$

As can be seen, (6-18) which was estimated by the phase noise compensation algorithm is different from (6-19), namely $\Phi_{NPNC}(t)$ is not equal to $\Phi_{Nref}(t)$ in this case. This error can be described by considering the principle of the phase noise compensation of PNC-OFDR (Fig. 6-7(a)). If the time behavior of the optical frequency of the signal can be expressed as a pure time shift of that of the local light, the phase noise compensation method is exactly correct and provides correctly estimated phase information. However, if GVD is considered, the time behavior of the optical frequency of the signal is no longer the pure time shift of the local light. In such cases, the estimated phase includes estimation errors as shown in Fig. 6-7(b), and so $\Phi_{NPNC}(t)$ is not equal to $\Phi_{Nref}(t)$ in a precise sense, and then (6-18) is different from (6-19).

However, from a practical point of view, this error is negligible for PNC-OFDR. As previously mentioned, the first bracket can be disregarded for both (6-18) and (6-19). Finally, considering $\left|(N-1)\pi\gamma\beta_2^{(r)}v_g\tau_1\right| \ll 1$ for (6-18), the following relation is obtained.

$$\omega_{rNPNC}(t) = \omega_{rNref}(t) = \frac{\tau_0}{N\tau_1}\left(\frac{2\pi\gamma\beta_2^{(F)}v}{^{(r)}v_g t+1}\right). \quad (6\text{-}20)$$

It can be seen clearly that if $\beta_2^{(F)} = \beta_2^{(r)}$, PNC-OFDR can also compensate for the GVD effect. Note that GVD also affects the phase noise compensation, but it is negligible for the same reason, namely it is very small. Therefore, it is described theoretically that PNC-OFDR can compensate both the phase noise and GVD simultaneously.

This function is also demonstrated experimentally. Figure 6-8 shows traces of a 5 km-long dispersion shifted fiber (DSF) measured by PNC-OFDR. The GVD parameter of the DSF was -2.54×10^{-27} s^2/m (corresponding to 2 ps/nm/km) and different from that of the delay fiber line consisting of SMF. The black, red and blue lines show results measured by using spectral lines with wavelengths of 1547.35, 1549.95 and 1552.56 nm, respectively, as the test light. These represent the minimum, center and maximum wavelengths of the optical comb shown in Fig. 6-1(b). The reflection positions differed because the GVD compensation did not function well as a result of the difference between the GVD parameters of the delay fiber line and the FUT, i.e. the SMF and the DSF. The difference of 7.5 cm between the reflection positions was in good agreement with the value calculated based on (6-20). If these traces are averaged for FSAV, it leads to a broadened reflection shape and degraded spatial resolution. Such broadening was not seen in experimental results using the same fibers for FUT and the delay fiber as shown in Fig. 6-4. Therefore, these results mean that the GVD of the FUT was compensated for by using a reference interferometer consisting of the delay fiber with the same GVD parameter as the FUT. Therefore, it is revealed that PNC-OFDR can simultaneously compensate for both the phase noise and the GVD effect induced by using broad optical comb light source without any additional calculation process.

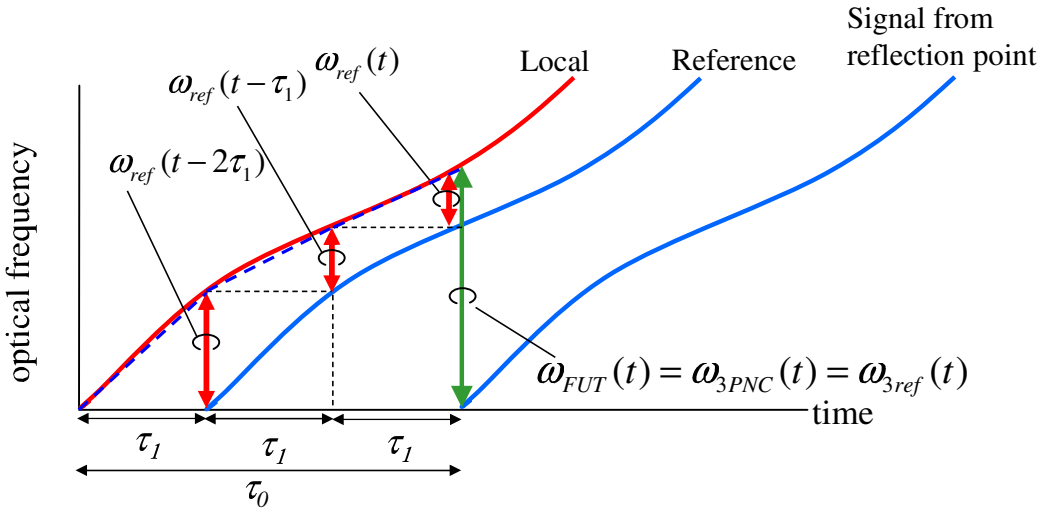

(a)

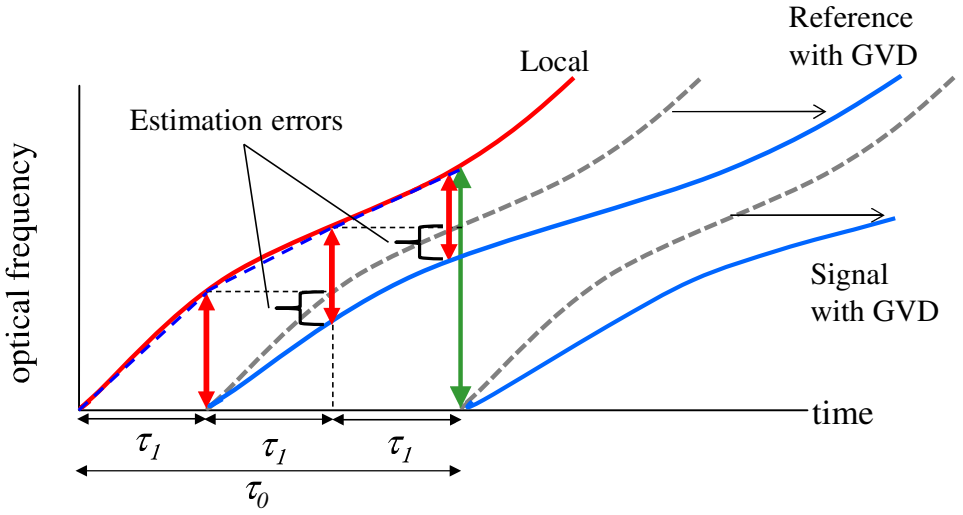

(b)

Figure 6-7 Schematic diagram of the phase noise compensation in PNC-OFDR.

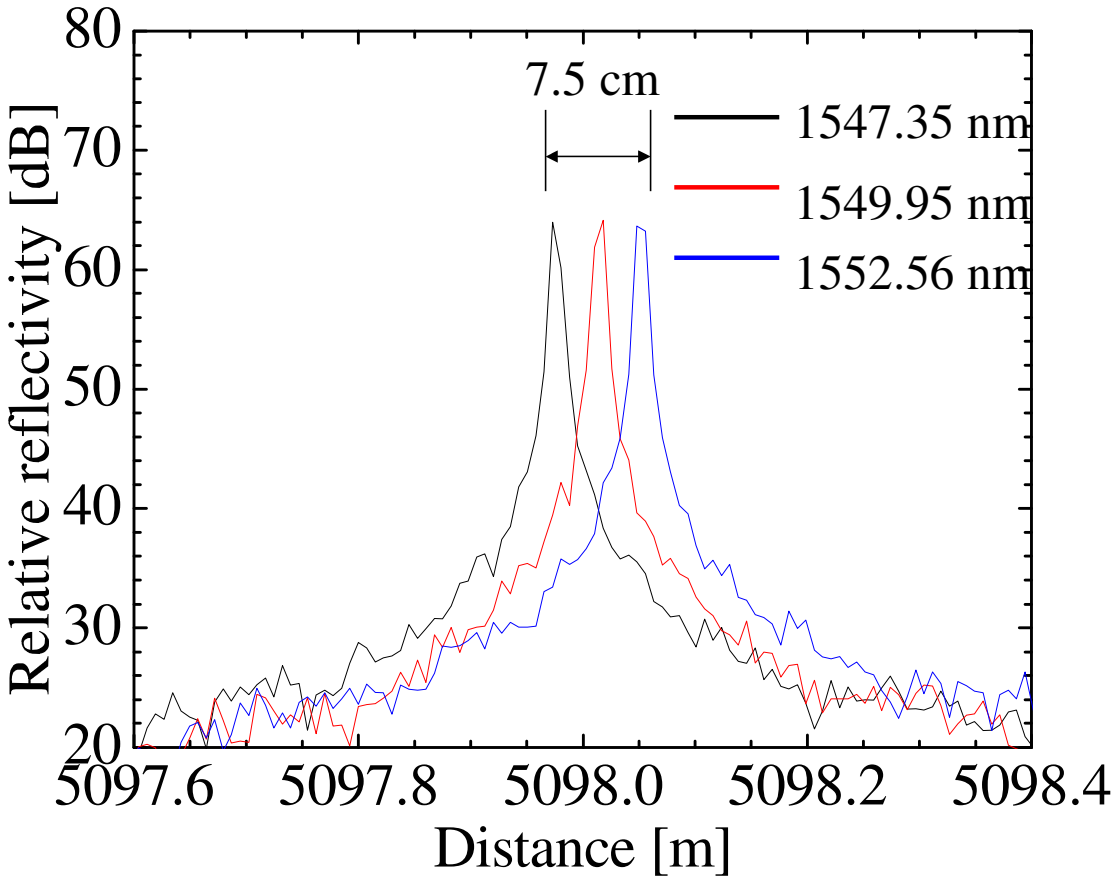

Figure 6-8 Reflection obtained by different comb spectral lines. The FUT was a 5 km-long DSF.

6.6. Conclusion

It was clarified that it was useful to employ an optical comb light source with a 675-GHz bandwidth tunability and several kHz linewidth in PNC-OFDR for fading noise reduction. The phase noise compensation algorithm functioned well with the fading noise suppression using the comb light source, and so PNC-OFDR achieved a 0.6-dB relative accuracy for the Rayleigh backscatter level with a spatial resolution of 2 cm over a 10.4 km-long SMF with GVD. To enhance practical use of PNC-OFDR, development of more compact light source with the narrow linewidth and broad tunability would be a key issue.

It was also clarified theoretically and experimentally that PNC-OFDR could provide simultaneous compensation for both the phase noise and GVD to achieve a high spatial resolution. GVD compensation was demonstrated by using a reference interferometer consisting of a delay fiber with the same GVD parameter as the FUT. Moreover, the GVD compensation did not need additional equipment or calculation because it could be performed simultaneously during the phase noise compensation process. We revealed that the influence of GVD on the phase noise compensation algorithm was negligible.

The Rayleigh scattering level was accurately observed with cm-level resolution over a 10-km range, and we believe that this achievement is a significant step towards the practical use of OFDR in diagnosing short- or middle-range fiber networks.

7. Field test of PNC-OFDR

7.1. Introduction

The PMD of installed optical fiber cables is a limiting factor for ultrafast transmission systems operating at, for example, a single channel transmission rate of 40 Gbit/s or more. In particular, legacy fibers installed before the early 1990s often exhibit high PMD values that are unsuitable for high-speed transmission. In terms of fiber management, it is very useful to know the distribution of such large birefringence along installed fibers. Polarization-sensitive optical time domain reflectometry (P-OTDR) [7-1] is a useful tool for measuring the states of polarization (SOPs) of backscattered lightwaves, from which we can know the beat length. Recently, techniques for calculating birefringence, or even PMD, by employing the backscattered SOP measured using P-OTDR, have progressed greatly [7-2]-[7-6]. However, the spatial resolution of P-OTDR is limited to ~1 m and this is insufficient to sample the birefringence of high-PMD fibers. So, how to recognize a large birefringence with a corresponding beat length that is shorter than the spatial resolution of P-OTDR remains an open issue. Moreover, a longer measurement range is desired because the ultrafast system is employed to long-haul links. If we assume that the maximum length of a terrestrial link is 80 km, a range of at least 40 km is needed with both-end access.

For these reasons, we focused on developing PNC-OFDR with a sufficiently fine spatial resolution and a long measurement range to detect short-period polarization changes of high-PMD fibers, namely short beat length, installed in long-haul links.

As shown in chapter 4, in a long range measurement, the dominant factor as regards resolution degradation of PNC-OFDR was the environmental acoustic perturbation acting on the FUT, whereas the PNC algorithm well worked even for distances of several tens of

kilometers [7-7]. If we are to extend the measurement distance while maintaining the spatial resolution, it is important issue to find a way to reduce the influence of such environmental perturbation.

In this chapter, a bandwidth-division PNC-OFDR technique capable of reducing the influence of environmental perturbation via a fast sweep of the optical source frequency is presented [7-8]. A performance evaluation of PNC-OFDR that we made when using it to measure installed optical cables in actual field environments is also reported [7-9]. Section 7.2 presents a principle of the bandwidth-division PNC-OFDR which realizes the enhancement of the measurement bandwidth. Section 7.3 explains our experimental setup. Section 7.4 demonstrates the bandwidth-division PNC-OFDR with a sub-cm spatial resolution over 40 km in a normal laboratory environment and a 5 cm spatial resolution at 39.2 km in a field environment. Section 7.5 describes results of field tests on detection of high-PMD cable sections.

7.2. Principle of bandwidth-division PNC-OFDR

At a long distance such as 40 km, even after the phase noise compensation, environmental perturbation becomes a dominant factor degrading the spatial resolution. Therefore, as mentioned in the introduction, a fast sweep of the optical source frequency is needed to reduce the effect of environmental acoustic perturbation. However, a fast sweep generates a high beat frequency, which makes it difficult for later sampling or processing. To deal with this problem, we can adopt a bandwidth-division method. If we assume a maximum frequency of F, we need a sampling card with a sampling rate of greater than 2F. Figure 7-1(a) shows that we can divide the frequency into M sections, each with a bandwidth of F/M. If we down-convert the m-th (m=2, 3, … , M) section as shown in Fig. 7-1(b) so that it is within a frequency of $0<f_{base}<F/M$, we only need a sampling card with a sampling rate of 2F/M. Meanwhile, the amount of data decreases to 1/M compared with that required when using the conventional sampling method.

We should note that $X_N(t)$ is no longer the correct reference to compensate for the phase noise in the down-converted signal. To obtain the correct reference, we should also down-convert the frequency of $X_N(t)$ by the same value. This can be realized by changing $X_N(t)$ as follows:

$$X\quad)(t) = X_N(t) - 2\pi\frac{m-1}{M}\mathrm{F}t. \tag{7-1}$$

Figure 7-2 shows schematically how to compensate for every sections of the FUT by using suitable reference signals. Another method for accomplishing the compensation correctly is to rebuild the original measurement signal before down-conversion, and use $XN(t)$ for compensation. Although the two methods are equivalent to each other and can be implemented digitally, we adopt the former because it consumes fewer calculation resources.

As a result, with bandwidth-division PNC-OFDR, the bandwidth is reduced to 1/M, thus enabling us to find a suitable sampling card even when the original signals have a very large electrical bandwidth. Moreover, for a personal computer with a limited physical memory, it helps us to process more divided section data, providing another

way of improving the spatial resolution. The data-sampling number will be M times the previous number, accompanying the increase in electrical equipment. However, the most important thing is that we can reduce the influence of environmental perturbation to a 1/M level.

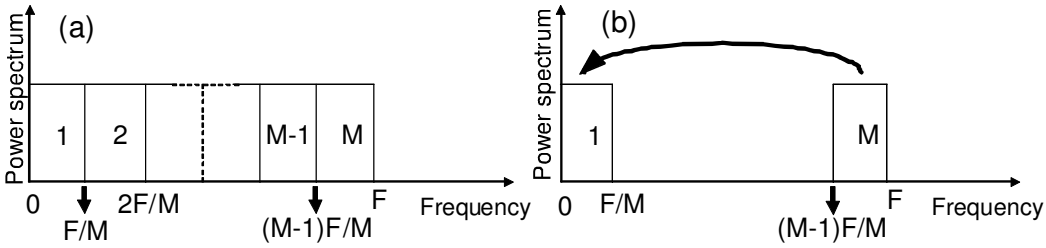

Figure 7-1 Concept of bandwidth-division process.

]

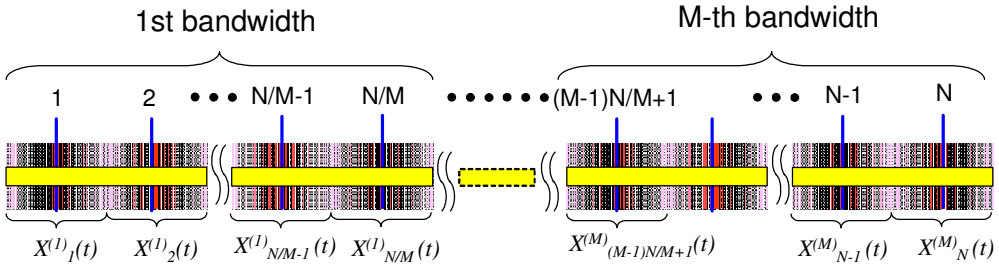

Figure 7-2 Reference signals used in each section of FUT for different bandwidths.

7.3. Experimental setup of bandwidth-division PNC-OFDR

In our experimental setup shown in Fig. 7-3, the light source is a fiber laser (Koheras Adjustik^{TM}) and the linewidth measured using the self-delay heterodyne method with a 100 km delay fiber is 4 kHz. If we assume that the lineshape is Lorentzian, the measurement range of regular OFDR can be estimated to be $c/2n\pi\Delta f$ as 8.0 km while considering the round-trip path, where c is the speed of light in vacuum, n is the refractive index of FUT, Δf is the linewidth. A SSB-SC modulator and a frequency swept RF synthesizer are used for external frequency sweeping. The sweep rate is set at 3 THz/s, which is 7.5 times faster than that used previously [7-7], with a full sweep frequency of 15 GHz (limited by available bandwidth of the modulator) for a 5-ms acquisition time. The ratio of beat frequency to distance is determined by the sweep rate to be $2n\gamma/c$ as 300 Hz/cm, where γ is the sweep rate. If we consider the calculation process, after applying PNC process and the round-off for later averaging, the useful part is 12.5 GHz (4.17 ms acquisition time), corresponding to a theoretical spatial resolution of 8 mm (240 Hz in frequency domain). A Mach-Zehnder interferometer with a 5-km delay fiber in one arm is used as a reference interferometer for compensation, and is placed in a soundproof box to insulate it from acoustic noise. The main interferometer consists of a local arm and a measurement arm, which is equipped with a circulator for launching the lightwave into the FUT and receiving the reflected signal. A polarization controller is used in the local arm to control the power of the local light so that it is split evenly by the polarization splitters, which are important elements of a polarization diversity scheme, adopted to remove the influence of the polarization effect. The signals from both the reference and main interferometers are detected by balanced photodetectors (BPDs). Then, the signals from the reference interferometer are filtered by a LPF, sampled by using an A/D, and collected by a computer. On the contrary, the signals from the main interferometers must undergo bandwidth-division processing before being sampled by the A/Ds. The details of the process are given in the next paragraph.

For this experiment, we choose an M value of 3 for the purpose of preliminary theoretical confirmation. For an FUT of ~ 40 km, the maximum frequency F of the signals from the main interferometers is ~ 1200 MHz. Figure 7-4 illustrates the electrical process after one BPD. Two electrical switches are used to select the route with the help of synchronization equipment. When the 1st route is selected, there is no processing within the route. When the 2nd or the 3rd route is selected, the signals are filtered by a band-pass filter with a bandwidth of 400 ~ 800 MHz (BPF1), or 800 ~ 1200 MHz (BPF2). Then the signals are down-converted by using a mixer beat with sinusoidal signals whose frequency is 408 MHz (route 2) or 800 MHz (route 3), generated from an arbitrary waveform generator. For route 2, 400 MHz is not used for mixing since the mixer is not ideal and this signal will still be present after mixing, resulting in a spurious peak. Therefore, it is expected that a larger frequency will be used here since the spurious peak does not influence the original results. The signals are then divided into three sections of 0 ~ 408, 408 ~ 800, and 800 ~ 1200 MHz. After the mixer, the signals are filtered by an LPF with a cut-off frequency of 400 MHz, sampled by using an ADC with a sampling rate of 1 GS/s, and collected by a computer, to undergo a numerical compensation process.

The compensation is performed with a high-end personal computer with an Intel Core i7-980X CPU and a 24 GB cache memory. To reduce fading noise, we take the average intensity of the results obtained with different probe wavelengths by using a laser tuning range of over 60 GHz. The full measurement time is about 2 min, and this is limited by the laser tuning speed. About 30 min is needed to compensate the data of one bandwidth (0 ~ 14.0, 14.0 ~ 27.5, or 27.5 ~ 41.25 km) with a 50-wavelength average.

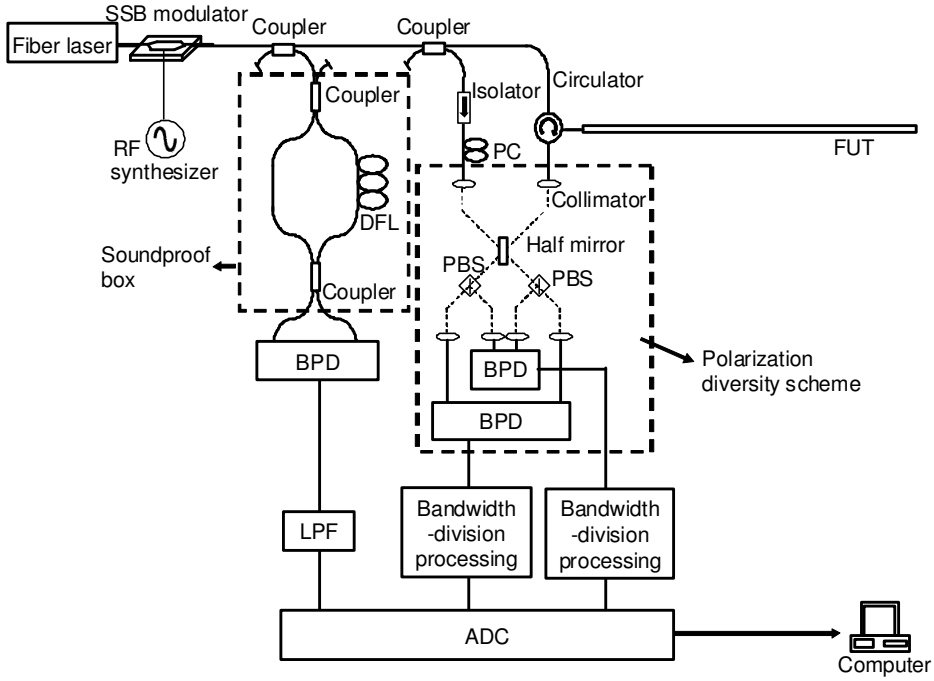

Figure 7-3 Experimental setup. SSB: single sideband, DFL: delay fiber line, PC: polarization controller, PBS: polarization beam splitter, BPD: balanced photodetector, LPF: low-pass filter, ADC: analog to digital converter and FUT: fiber under test.

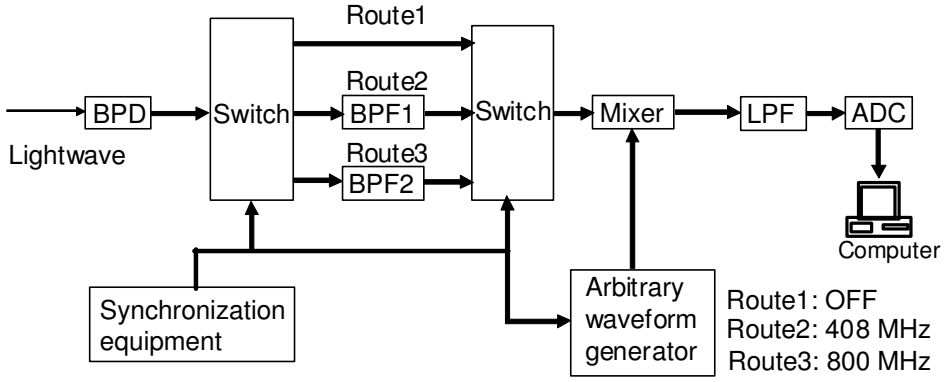

Figure 7-4 Electrical processing after the signals having been received by one BPD. The bandwidth of BPF1 and BPF2 is 400 ~ 800 MHz, and 800 MHz ~ 1200 MHz, respectively, and the LPF cutoff bandwidth is 400 MHz.

7.4. Performance of bandwidth-division PNC-OFDR

The FUT is composed of a 40 km fiber spool connected to a 1.25 km fiber spool equipped with an APC connector. Figure 7-5 shows the reflectivity of backscattered/reflected lightwave, which is a combination of three different divisions. Due to the abrupt attenuation around the cut-off frequency of the electronic filters, these signals with frequencies outside the bandwidth, such as signals around 400 ~ 408 MHz, are also highly attenuated. In fact, a more carefully designed filter should be adopted to alleviate this attenuation. Meanwhile, since the BPD used in our setup has a cut-off frequency of 800 MHz, which is less than the original frequencies (800 ~ 1200 MHz) generated at the third division, the results at longer distances are greatly attenuated. This is the widest bandwidth of our available equipment, and in fact a BPD with a wider bandwidth should be adopted to avoid the excess attenuation.

We placed the FUT in two different laboratory environments to check the spatial resolution since it is influenced by the environment. The total sound pressure was 58.1 dB in a normal laboratory environment and 60.7 dB in a relatively noisy laboratory environment. The sound pressure densities of two different experimental environments are shown in Fig. 7-6(d), while the details of the reflection peaks at different environments are shown in Figs. 7-6(a)~(b). For the reflection peaks that occur around 40 km (N × 2.5 km), which is an optimum compensation position, a 3-dB spatial resolution of 8 mm (240 Hz in frequency domain) is obtained in a normal environment and it deteriorates to about 2.5 cm (750 Hz in frequency domain) in a relatively noisy environment. For the reflection peaks that occur around 41.25 km ((N + 0.5) × 2.5 km), which is the border of the 16th compensation section, the spatial resolution is still 8 mm in a normal environment, and it deteriorates to about 5 cm (1500 Hz in frequency domain) in a relatively noisy environment.

We compared the results to those obtained without bandwidth-division process at a sweep rate of 1 THz/s, the reflection peaks almost remain the same in the frequency domain. Therefore, it is obvious that the environmental perturbation caused the added

frequency components. By sweeping the optical source frequency faster, we decreased the ratio of these added frequency components to beat frequency, therefore making spatial resolution improved. In the normal laboratory environment, we obtained a spatial resolution of 8 mm at any position within the entire measurement range.

Since the results are dependent on the environment, it is thus necessary to test the setup in a field environment to check its performance. The field trial was performed in Japan on an optical cable that was installed underground to link two cities, and that is still in use. The fiber for the test was a 39.2-km-long DSF, and was temporarily out of use. The detailed reflection peak at the final connector is also shown in Fig. 7-6(c), revealing a spatial resolution of 5 cm in the field environment.

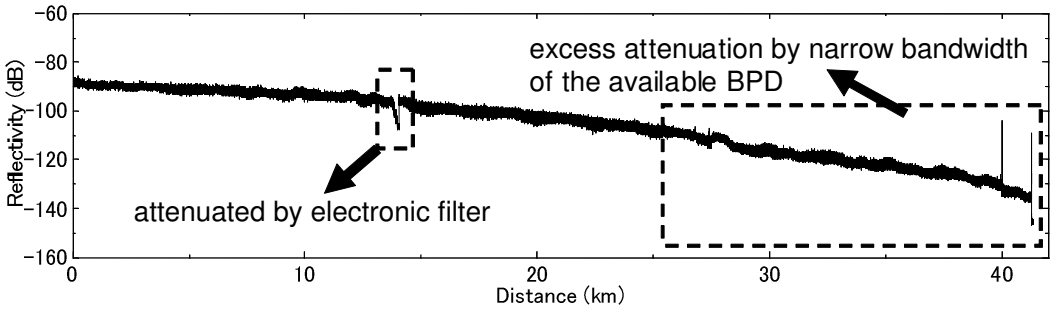

Figure 7-5 Measurement results for the reflectivity of backscattered/reflected lightwave.

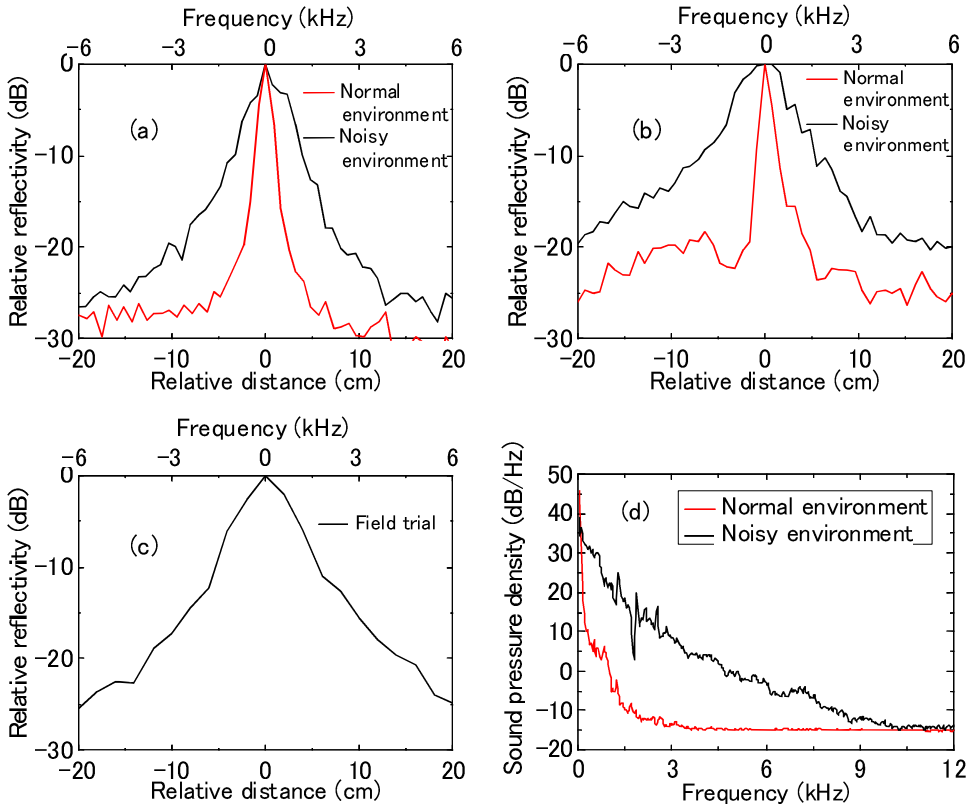

Figure 7-6 Details of reflection peaks in different environments. (a) Reflection peaks at 40 km measured in the laboratory, (b) Reflection peaks at 41.25 km measured in the laboratory, (c) Reflection peak at 39.2 km measured in the field environment and (d) Sound pressure density of two laboratory environments.

7.5. Field tests on detection of high-PMD cable sections

The field tests were performed in Japan on optical cables that were installed in the early 1990s, and that are still in use. Figure 7-7 shows the lengths of the optical cables used for the field trials. They were installed underground to link two central offices belonging to the same telecommunication carrier. The measurements were performed at all the listed offices except E and H. The fibers were all DSFs, and those temporarily not in use were chosen for the tests, whose numbers are summarized in Table 7-1. There was an interval of one week between the measurements at two neighboring offices, and all the measurements were performed during the daytime. For distances of less than 40 km such as that of cable installed between central offices A and B, the parameters used in the setup are exactly the same as those described in section 7.3. For distances between 40 and 80 km, we can perform the same measurement at both central offices to obtain full knowledge of the reflectivity along the fibers. Since there are no final Fresnel reflection peaks with which to evaluate the performance, we decreased the optical frequency sweep rate to 1.5 THz/s, namely half of the speed used in section 7.3, to limit the beat frequencies to less than 1.2 GHz, thus avoiding the need for a hardware upgrade. For purposes of comparison, the spatial resolution can be described in frequency units, or can be converted into length units using the original sweep rate of 3 THz/s, since in reality we perform the measurements at both central offices using this sweep rate. Both processing methods are effective, and the latter is adopted in this measurement.

Figure 7-8 summarizes the final Fresnel reflection peaks of fibers in different optical cables, by averaging all the peak shapes of fibers in same optical cables. It is obvious that the spatial resolutions are different for these different environments, including the installed environments, and the instant changes that occurred during the measurement. The cable between central offices F and E has one part installed in a shared duct that is very close to the ground and susceptible to the influence of external perturbations such

as vibrations. The span of the shared conduit line is about 1~2 km, and it has an adverse influence on the spatial resolution, which is clearly shown by the blue line in Fig. 7-8.

The 3- and 10-dB spatial resolutions of different cables are summarized in Fig. 7-9. Error bars show the standard deviations calculated from fibers in the same cable and measured from the same direction. For a different measurement direction, the distance shown in Fig. 7-9 is slightly adjusted to avoid superimposition. The spatial resolutions obtained from the same cable with different measurement directions exhibit similar statistical behaviors. The aim for a 3-dB spatial resolution is 10 cm, and the results show that it has almost been realized.

Table 7-1 Numbers of FUT

FUT	Number	FUT	Number
A to B	15	B to A	15
C to D	28	D to C	28
E to F	0	F to E	2
F to G	16	G to F	16
G to H	4	H to G	0

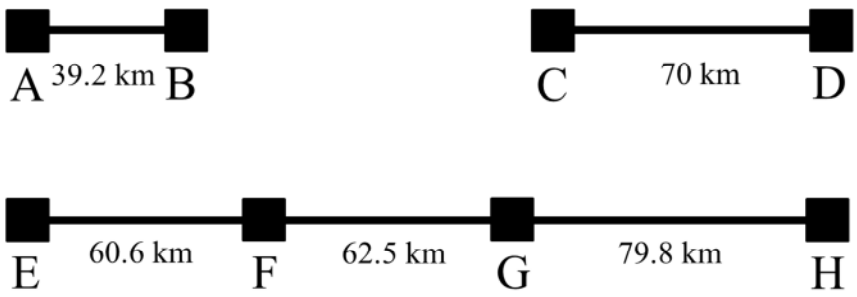

Figure 7-7 Lengths of optical cables between central offices used for field trials.

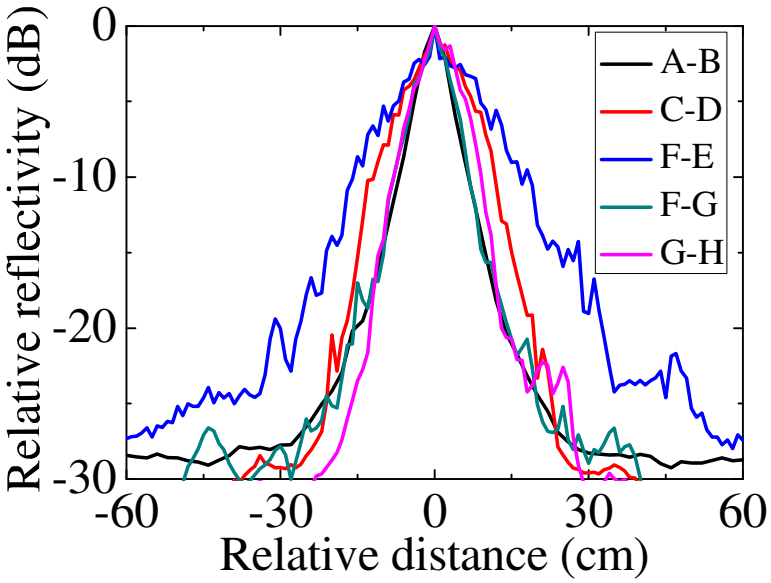

Figure 7-8 Reflection shapes of fibers in different optical cables

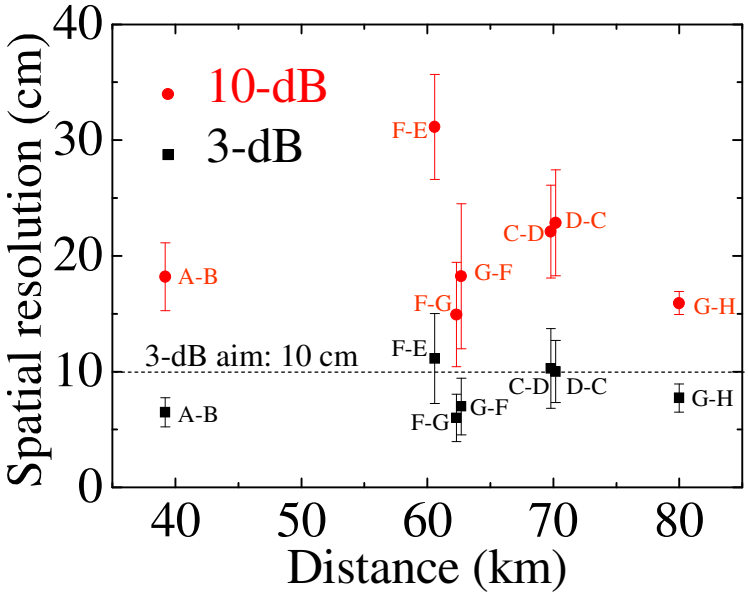

Figure 7-9 3- and 10-dB spatial resolutions of different optical cables.

As explained in [7-10], with a polarization diversity detection scheme, full polarization information was obtained with PNC-OFDR. To improve the accuracy when measuring backscattered SOPs along the fibers, a method of averaging in the wavelength domain is used to suppress Rayleigh fading noise. The wavelength range used for averaging is about 0.4 nm (50 GHz optical frequency), which we tune in steps of about 1 GHz to obtain 50 measurements. The averaging process limits the measurable PMD to much less than 20 ps to avoid washing out the polarization beat at the far end. The residual noise on the measured Stokes parameter causes a maximum variation of about 0.2 rad on the Poincaré sphere. Then the round-trip birefringence vectors are obtained by calculating the radians rotated around the Poincaré sphere. Since the algorithm is a kind of differential approach, which amplifies the noises, we averaged the calculated vectors every ten meters to reduce these noises.

The magnitude of the average vector is the round-trip birefringence, and the results of three examples measured from central office A to central office B are shown in Fig. 7-10. Here, red columns are used to show the locations of the splice points, which are introduced from the cable management database. It is clear that round-trip birefringence was not uniform along the fiber, and several sections had large values. Abrupt changes in the round-trip birefringence are observed at certain splice points, confirming the validity of our measurement, since different kinds of fibers may be spliced in the cable. The insets in Fig. 7-10 give the x-polarization reflectivity of the high-birefringence section. It is seen that when the round-trip birefringence is high, the beat lengths are very short. One part even exhibits a beat length of only ~ 20 cm, which could not be detected by conventional P-OTDR, or, to the best of our knowledge, by any other type of reflectometry over such a long range. The PMDs of the three examples were 4.4, 6.3 and 9.2 ps, averaged in the 1525 to 1620 nm wavelength domain in 0.05 nm steps, and measured using a commercial instrument with the Jones matrix eigen-analysis (JME) method. The PMD is rather large and we assume that the main reason for this is the existence of these high-birefringence sections.

The birefringence cannot simply be obtained from the round-trip birefringence if

there is circular birefringence [7-2]-[7-3]. However, these two parameters are thought to be closely correlated. If the birefringence is uniformly linear, a beat length of 25 cm means a round-trip birefringence of 6×10^{-6}. However, the results of #3 around 36.4 km show that the results are only 1/3 of what we expect from the beat length. We think that this may be caused by the noise of the measured SOPs, and we must undertake a detailed study in the future. However, we believe that "bad" sections can be judged from the knowledge of the round-trip birefringence distributed along the fiber. Meanwhile, a new insight into installed cables that is different from the stereotypical image is obtained from the measured information: although all three fibers (#1, #2 and #3) are in the same installed cable, the "bad" sections are not always the same. We speculate that fibers from different rods were used in the cabling process, allowing different kinds of fibers to exist in the same section.

Optical cables between central offices C and D, and those between central offices F and G were also measured, and examples of the results are shown in Fig. 7-11. Owing to the noise of the measured SOPs, the two results for overlapping positions measured from different sides are not entirely the same. However, a high correlation can be observed between them, which confirm the validity of our measurement. From all the measured results, many of which are not shown here, we also confirmed an unsurprising result that when the PMD is high, the number of "bad" section tends to be large.

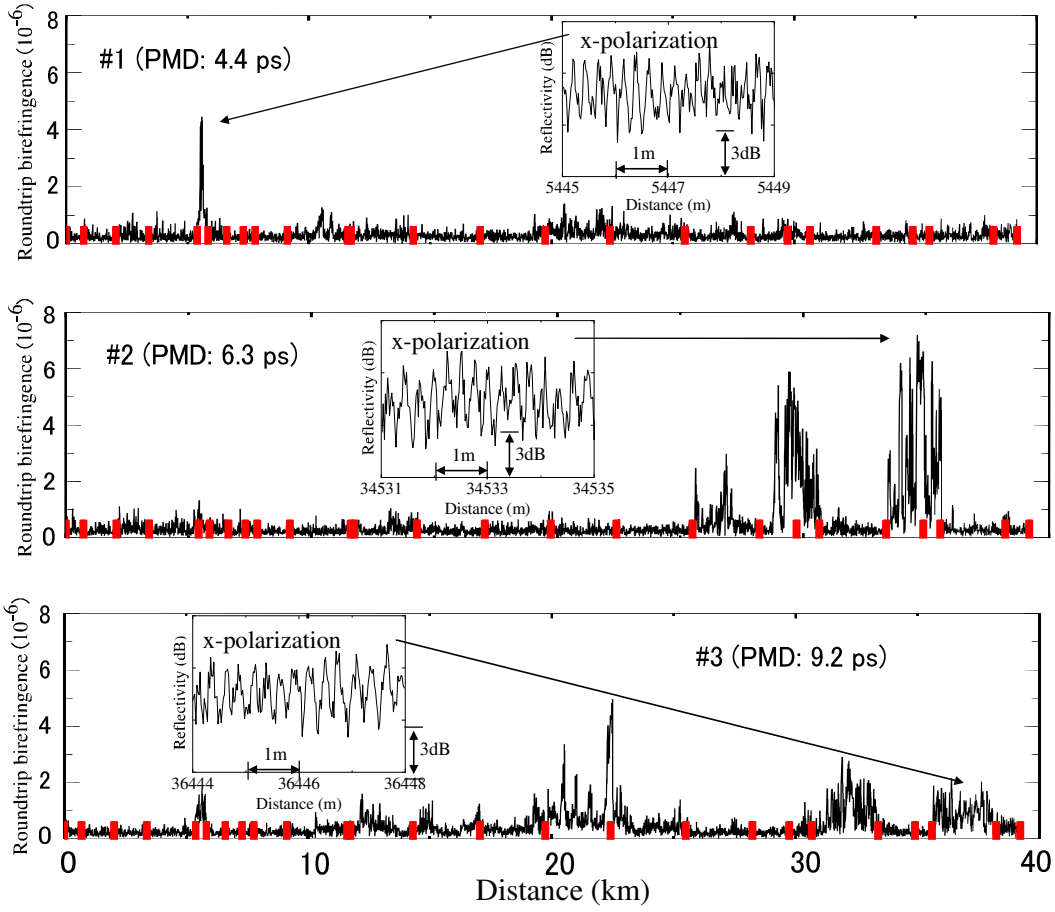

Figure 7-10 Three examples of round-trip birefringence measured from central office A to central office B. The insets show the x-polarization reflectivity of PNC-OFDR in the high-birefringence section.

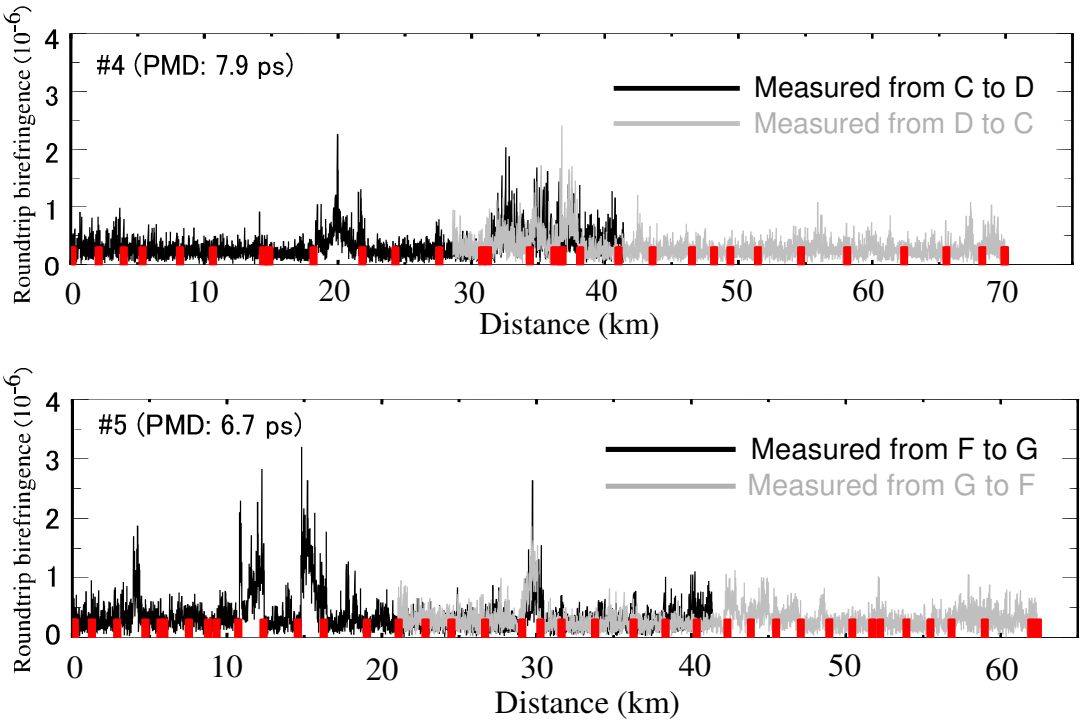

Figure 7-11 Examples of measured round-trip birefringence. Fiber #4: measured between central offices C and D, and Fiber #5: measured between central offices F and G.

7.6. Conclusion

A bandwidth-division PNC-OFDR technique, capable of reducing the influence of environmental acoustic perturbation via a fast sweep of the optical source frequency, by decreasing the ratio of the acoustic noise band to beat frequency was presented. The bandwidth-division scheme permits us to deal with high-frequency signals by adopting a fast sweep of the optical source frequency. Meanwhile, the reduction of the signal bandwidth enables us to sample and process more data, thus helping us to improve the spatial resolution. By using this technique, a sub-cm spatial resolution over 40 km in a normal laboratory environment, and a 5 cm spatial resolution of 39.2 km in a field environment was realized.

Moreover, PNC-OFDR was tested in different field environments. A spatial resolution of 10 cm was obtained in the field for distances of 60 ~ 80 km. The outstanding resolution makes it possible to identify high-birefringence sections along the installed cables. In the field trial, we successfully observed beat lengths as small as ~ 20 cm, which shows that there were very large birefringence sections in the installed cables. By identifying high-birefringence sections using PNC-OFDR, we can obtain a good understanding of the installed cables with a new insight. The result will be very useful in relation to fiber management.

8. Summaries and conclusions

The main objective of this thesis is to realize long range measurement with high spatial resolution and sensitivity by overcoming the limitation of C-OFDR and clarify applicability to optical fiber network diagnostics. The theory to overcome the limitation caused by the light source coherency was proposed in chapter 2. For improving basic performance of conventional C-OFDR, a novel scheme for realizing a tunable light source with high coherency was also proposed and demonstrated in chapter 3. A novel C-OFDR implementing those two technologies, namely PNC-OFDR, was demonstrated, and effectiveness of the phase noise compensation was clarified in chapter 4. Attempts for improving a spatial resolution and a measurement accuracy of PNC-OFDR were explained in chapter 5 and 6. Results of field trials on detection of cable sections with high-PMD (or birefringence) were shown in chapter 7. The following summarizes the results which are obtained in each chapter.

Chapter 2 proposed the theory of C-OFDR employing a novel phase noise compensation technique (or CRM) for measurements beyond the light source coherence length. It was shown that the CRM numerically generated appropriate reference signals for the compensation by a single measurement with single reference interferometer. It was theoretically confirmed that the compensation effect worked well in the coherence time range of the light source on either side of the mid-point in divided section of FUT for the compensation. Hence it was clarified that the CRM was effective to overcome the limit of C-OFDR measurement range, and PNC-OFDR was powerful tool for measurements beyond the coherence length.

Chapter 3 proposed C-OFDR employing an SSB-SC modulator and a narrow linewidth fiber laser as a tunable light source. It was shown that the advantage of this

scheme was that the optical frequency sweep was conducted while maintaining the high coherency of the fiber laser. The superiority of using SSB-SC modulation for the external modulation was also clarified. A 5 km range measurement with cm-level spatial resolution was demonstrated. The average spatial resolution (FWHM) was < 30 mm and the sensitivity was –30 dB relative to the Rayleigh backscattering level. This improvement of fundamental performances enabled us to realize higher spatial resolution measurements in the region beyond the coherence length by employing the phase noise compensation..

Chapter 4 clarified that the dominant noise limiting the spatial resolution of PNC-OFDR was acoustic noise caused by environmental acoustic perturbation acting on the FUT. It was demonstrated that when both the reference interferometer and the FUT were insulated against acoustic noise, the phase noise compensation scheme functioned well over a 40 km range. It was also indicated experimentally that the dominant noise before the phase noise compensation was the laser phase noise rather than acoustic noise even when the fiber laser with a narrow line width of a few kHz was used. It was also clarified that PNC-OFDR could be used for various applications targeting mid- to long-range networks with a narrow spatial resolution because it was experimentally confirmed that the performance in field use did not degrade.

Chapter 5 proposed a novel technique for improvement of the spatial resolution. The 3rd-order sideband was generated by two LN-IMs arranged in series for a broader external frequency sweeping. It was experimentally confirmed that the optical frequency sweep rate and sweep span became 780 GHz/s and 18 GHz, respectively. Therefore, the theoretical spatial resolution was also improved to 5.5 mm. The achieved spatial resolution was sub-cm over a 10 km range. The sensitivity was about −25 dB for all measurements.

Chapter 6 clarified that an optical comb light source with a 675-GHz bandwidth tunability and several kHz linewidth was effective for fading noise reduction in PNC-OFDR. The phase noise compensation algorithm functioned well with the fading noise suppression, and so PNC-OFDR achieved a 0.6-dB relative accuracy for the

Rayleigh backscatter level with a spatial resolution of 2 cm over a 10.4 km-long SMF. It was also clarified theoretically and experimentally that PNC-OFDR could provide simultaneous compensation for both the phase noise and GVD. It was also clarified the GVD compensation did not need additional equipment or calculation because it could be performed simultaneously during the phase noise compensation process.

Chapter 7 described that the detection of high-birefringence sections along cables installed in actual fields were successfully performed by using the bandwidth-division PNC-OFDR. A spatial resolution of 10 cm was achieved for distances of 60 ~ 80 km in the field. We successfully observed beat lengths as small as ~ 20 cm, which shows that there were very large birefringence sections, namely high-PMD sections, in the installed cables. By identifying high-birefringence sections using PNC-OFDR, we can obtain a good understanding of the installed cables with a new insight. The result will be very useful in relation to fiber management.

As summarized above, the limitation resulting from the laser coherency was overcome, and so PNC-OFDR with a long measurement range, high spatial resolution and high sensitivity was realized as shown in Fig. 8-1. For a long time, reflectometric tests on optical cable have been performed exclusively with OTDR. When optical fibers have been delivered to every home, the optical link includes many connection points and/or optical devices such as optical splitters and filters. As a result, there is an increasing demand for the detection of close events occurring in fiber. For trunk-line, it is important to detect high-PMD cable sections for an efficient cable management. Hence, the spatial resolution of OTDR is not always sufficient for maintenance engineers. PNC-OFDR studied in this thesis can be expected to fulfill the requirements on optical fiber network diagnostics. Moreover, the continuous development of maintenance technologies with optical reflectometry can be contributed to realization of future networks with high reliability and sustainability.

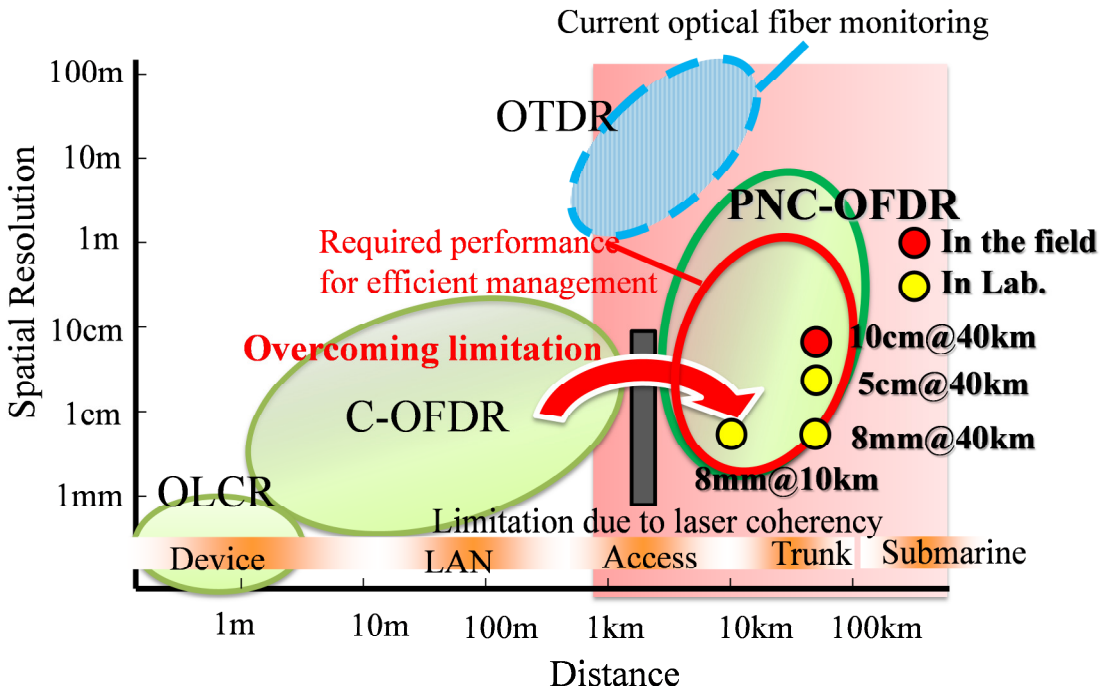

Figure 8-1 Achieved performance of PNC-OFDR

Acknowledgement

First of all, the author would like to extend sincere thanks to Professor Katsuyuki Utaka of Waseda University for his guidance, invaluable advice and encouragement to summarize this study. The author also gratefully thanks to Professor Isamu Kato, Professor Mitsuji Matsumoto and Professor Hirochika Nakajima of Waseda University for their kind advices and encouragement. The author also thanks to Professor Hiroyuki Kawada of Waseda University who provides the author with the opportunities to summarize this study.

This thesis is based on research work conducted on Access network service systems laboratories, Nippon telegraph and telephone corporation. The author gratefully thanks to Mr. Hiromichi Shinohara, Mr. Koji Sakuda, and Mr. Yuki Sakuyama who provide the author with opportunities to be engaged in this study. The author also thanks to Mr. Kiminori Sato, Dr. Tadashi Haibara, Dr. Masatoshi Shimizu, Professor Makoto Tsubokawa of Waseda University, Dr. Shigeru Tomita, Mr. Yuji Azuma, Professor Fumihiko Ito of Shimane University, Dr. Hisashi Izumita, Dr. Atsushi Nobiki and Mr. Minoru Nakamura for their kind encouragement and guidance. The author also thanks to Mr. Hiroshi Amano, Dr. Kazuyuki Shiraki, Dr. Tetsuya Manabe, Mr. Kazunori Katayama and Mr. Takatomo Banno who provided the opportunities to summarize this study.

To progress this study, the author has been provided with useful advices and discussion from Professor Kazuo Hotate of University of Tokyo and Professor Zuyuan He of Shanghai JiaoTong University who are co-authors of papers related to this study. They should be also acknowledged.

Very special thanks go to my colleagues, Professor Xinyu Fan of Shanghai JiaoTong University, Dr. Daisuke Iida, Mr. Noriyuki Araki, Mr. Keiji Okamoto, Mr. Hiroyuki Iida, Mr. Masaaki Inoue, Mr. Tatsuya Okamoto, Mr. Hiroshi Takahashi, Mr. Chihiro Kito, and Mr. Takushi Kazama for their great cooperation and fruitful discussions with me. The author also thanks many other colleagues for their valuable discussions.

Finally, the author sincerely thanks my wife, Yumi, for her kind encouragement. The author hopes this thesis will be interest to my daughters, Mei and Risa, in the near future.

References

Chapter 1.

[1-1] J. Yamada, S. Machida, and T. Kimura, "2 Gbit/s optical transmission experiments at 1.3 μm with 44 km single-mode fibre," *Elctron. Lett.*, vol. 17, pp. 479-480, 1981.

[1-2] H. Shinohara, "Fiber optic communication system in Japan," in *proceeding of IEEE Lasers and Electro-Optics Society 13th Annual Meeting (LEOS 2000)*, vol. 1, pp. 3-4, 2000.

[1-3] K. Hagimoto, K. Iwashita, A. Takada, M. Nakazawa, M. Saruwatari, K. Aida, K. Nakagawa and M. Horiguchi, "A 212km non-repeated transmission experiment at 1.8Gb/s using LD pumped Er3+-doped fiber amplifiers in an IM/direct-detection repeater system," in *Technical Digest of the Optical Fiber Communication Conference and Exposition (OFC 1989)*, PD15, 1989.

[1-4] O. Kawata, I. Sankawa, and K. Okada, "Access network evolution scenario and key technological concept," in *proceeding of IEEE Global Telecommunications Conference (GLOBECOM 97)*, vol. 3, pp. 1471-1475, 1997.

[1-5] Y. Maeda, K. Okada, and D. Faulkner, "FSAN OAN-WG and future issues for broadband optical access networks," *IEEE Comm. Mag.*, vol. 39, pp. 126-132, 2001.

[1-6] H. Ueda, K. Okada, B. Ford, G. Mahony, S. horning, D. Faulkner, J. Abiven, S. Durel, T. Ballart, and J. Erickson, "Deployment status and common technical specifications for a B-PON system," *IEEE Comm. Mag.*, vol. 39, pp. 134-141, 2001.

[1-7] K. Tanaka, and Y. Horiuchi, "Advances in Ethernet PON Technologies," in *proceeding of the Joint International Conference on Optical Internet and Next Generation Network 2006 (COIN-NGNCON 2006)*, pp. 55-57, 2006.

[1-8] K. Kikushima, H. Yoshinaga, and S. Aoyagi, "Recent FTTH Systems and Services of NTT in Japan," in *proceeding of International Conference on*

Transparent Optical Networks 2006, vol. 1, pp. 14-17, 2006.

[1-9] Ministry of Internal Affairs and Communications, [online], Available: http://www.soumu.go.jp/johotsusintokei/field/data/gt010103.xls.

[1-10] K. Takada, I. Yokohama, K. Chiba, and J. Noda, "New measurement system for fault lovation in optical waveguide devices based on an interferometric technique," *Appl. Opt.*, vol. 26, pp. 1603-1606, 1987.

[1-11] K. Takada, M. Shimizu, M. Yamada, M. Horiguchi, A. Himeno, and K. Yukiatus, "Ultrahigh-sensitive low coherence OTDR using Er3+-doped high-power superfluorescent fiber source," *Electron. Lett.*, vol.28, pp. 29-31, 1993.

[1-12] M. K. Barnoski and S. M. Jensen, "Fiber waveguides: a novel technique for investigating attenuation characteristics," *Appl. Opt.*, vol. 15, pp.2112-2115, 1976.

[1-13] S. D. Personick, "Photon probe-An optical-fiber time-domain reflectometer," *Bell Syst. Tech. J.*, vol. 56, pp. 355-366, 1977.

[1-14] E. Brinkmeyer, "Backscattering in single-mode fibres," *Electron. Lett.*, vol. 16, pp. 329-330, 1980.

[1-15] M. Nakazawa, T. Tanifuji, M. Tokuda, and N. Uchida, "Photon probe fault locator for single-mode fiber using an acoustooptical light detector," *J. Quantum Electron.,* vol. QE-17, pp. 1264–1269, 1981.

[1-16] P. Healey, "Review of long wavelength single-mode optical fiber reflectometry techniques," *J. Lightw. Technol.*, vol. LT-3, pp. 876-886, 1985.

[1-17] M. Tateda, and T. Horiguchi, "Advances in optical time-domain reflectometry," *J. Lightw. Technol.*, vol. LT-7, pp. 1217-1224, 1989.

[1-18] Y. Koshikiya, N. Araki, H. Izumita, and F. Ito, "Newly developed optical fiber line testing system employing bi-directional OTDRs for PON and in-service line testing criteria," *IEICE Trans. Commun.*, vol. E90-B, pp. 2793-2802, 2007.

[1-19] N. Araki, H. Izumita, N. Honda and M. Nakamura, "Extended optical fiber line testing system using new eight-channel L/U band crossed optical waveguide coupler for L-band WDM transmission", *J. Lightw. Technol.*, vol. 21, pp. 3316-3322, 2003.

[1-20] K. Hogari, Y. Miyajima, S. Furukawa, N. Tomita, K. Tomita and M. Ohashi, "Wideband and highly reflective step-chirped fibre grating filter embedded in an optical fibre connector", *Electron. Lett.*, vol. 32, pp. 1230-1231, 1996.

[1-21] Y. Enomoto, H. Izumita and M. Nakamura, "Over 31.5 dB dynamic range optical fiber line testing system with optical fiber fault isolation function for 32-branched PON", in *proceeding of the Optical Fiber Communication Conference (OFC2003)*, ThAA3, pp. 608-610, Atlanta, USA, 2003.

[1-22] H. Dong, P. Shum, J. Q. Zhou, G. X. Ning, Y. D. Gong, and C. Q. Wu, "Spectral-resolved backreflection measurement of polarization mode dispersion in optical fibers," *Opt. Lett.*, vol. 32, pp. 1665–1667, 2007.

[1-23] A. Galtarossa, D. Grosso, L. Palmieri, and L. Schenato, "Distributed polarization-mode-dispersion measurement in fiber links by polarization-sensitive reflectometric techniques," *IEEE Photon. Technol. Lett.*, vol 20, pp. 1944-1946, 2008.

[1-24] W. Eickhoff and R. Ulrich, "Optical frequency domain reflectometry in single-mode fiber," *Appl. Phys. Lett.*, vol. 39, pp. 693-695, 1981.

[1-25] E. Brinkmeyer,W. Brennecke, M. Zum, and R. Ulrich, "Fiber Bragg reflector for mode selection and line-narrowing of injection lasers," *Electron. Lett.*, vol. 22, pp. 134-135, 1986.

[1-26] D. Uttam and B. Culshaw, "Precision time domain reflectometry in optical fiber systems using a frequency modulated continuous wave ranging technique," *J. Lightw. Technol.*, vol. LT-3, pp. 971-977, 1985.

[1-27] S. A. Kingsley and D. E. N. Davies, "OFDR diagnostics for fiber and integrated-optic systems," *Electron. Lett.*, vol. 21, pp. 434–435, 1985.

[1-28] R. I. MacDonald and H. Ahlers, "Swept wavelength reflectometer for integrated-optic measurements," *Appl. Opt.*, vol. 26, pp. 114-117, 1987.

[1-29] H. Ghafoori-Shiraz and T. Okoshi, "Optical-fiber diagnosis using optical-frequency-domain reflectometry," *Opt. Lett.*, vol. 10, pp. 160-162, 1985.

[1-30] H. Ghafoori-Shiraz and T. Okoshi, "Fault location in optical fibers using optical

frequency domain reflectometry," *J. Lightw. Technol.*, vol. LT-4, pp. 316–322, 1986.

[1-31] H. Barfuss and E. Brinkmeyer, "Modified optical frequency domain reflectometry with high spatial resolution for components of integrated optic systems," *J. Lightw. Technol.*, vol. 7, pp. 3-10, 1989.

[1-32] W. V. Sorin, D. K. Donald, S. A. Newton, and M. Nazarathy, "Coherent FMCW reflectometry using a temperature tuned Nd: YAG ring laser," *IEEE Photon. Technol. Lett.*, vol. 2, pp. 902-904, 1993.

[1-33] S. W. Henderson, P. J. M. Suni, C. P. Hale, S. M. Hannon, J. R. Magee, D. L. Bruns, E. H. Yuen, "Coherent laser radar at 2 μm using solid-state laser," *IEEE Trans. Geosci. Remote Sens.*, vol. 31, pp. 4-16, 1993.

[1-34] J. P. von derWeid, R. Passy, and N. Gisin, "Mid-range coherent optical frequency domain reflectometry with a DFB laser diode coupled to an external cavity," *J. Lightw. Technol.*, vol. 13, pp. 954-960, 1995.

[1-35] G. Mussi, N. Gisin, R. Passy, and J. P. von derWeid, "–152.5 dB sensitivity high dynamic-range optical frequency-domain reflectometry," *Electron. Lett.*, vol. 32, pp. 926–927, 1996.

[1-36] E. C. Burrows, and K. Y. Liou, "High resolution laser LIDAR utilizing two-section distributed feedback semiconductor laser as a coherent source," *Electron. Lett.*, vol. 26, pp. 577–578, 1990.

[1-37] M.-C. Amann, "Phase noise limited resolution of coherent LIDAR using widely tunable laser diodes," *Electron. Lett.*, vol. 28, pp. 1694–1696, 1992.

[1-38] A. Dieckmann, and M.-C. Amann, "Phase-noise-limited accuracy of distance measurements in a frequency-modulated continuous-wave LIDAR with a tunable twinguide laser diode," *Opt. Eng.*, vol. 34, pp. 896–903, 1995.

[1-39] S. Venkatesh, and W. V. Sorin, "Phase noise considerations in coherent optical FMCW reflectometry," *J. Lightw. Technol.*, vol. 11, pp. 1694–1700, 1993.

Chapter 2.

[2-1] W. Eickhoff and R. Ulrich, "Optical frequency domain reflectometry in single-mode fiber," *Appl. Phys. Lett.*, vol. 39, pp. 693-695, 1981.

[2-2] H. Barfuss and E. Brinkmeyer, "Modified optical frequency domain reflectometry with high spatial resolution for components of integrated optic systems," *J. Lightw. Technol.*, vol. 7, pp. 3-10, 1989.

[2-3] U. Glombitza, and E. Brinkmeyer, "Coherent frequency-domain reflectometry for characterization of single-mode integrated-optical waveguide", *J. Lightw. Technol.*, vol. 11, pp. 1377-1384, 1993.

[2-4] B. J. Soller, D. K. Gifford, M. S. Wolfe, and M. E. Froggatt, "High resolution optical frequency domain reflectometry for characterization of components and assemblies", *Opt. Express*, vol. 13, pp. 666-674, 2005.

[2-5] R. Passy, N. Gisin, and J. P. von der Weid, "High-sensitivity-coherent optical frequency-domain reflectometry for characterization of fiberoptic network components," *IEEE Photon. Technol. Lett.*, vol. 7, pp. 667–669, 1995.

[2-6] G. Mussi, N. Gisin, R. Passy, and J. P. von derWeid, "-152.5 dB sensitivity high dynamic-range optical frequency-domain reflectometry," *Electron. Lett.*, vol. 32, pp. 926–927, 1996.

[2-7] S. Venkatesh, and W. V. Sorin, "Phase noise considerations in coherent optical FMCW reflectometry," *J. Lightw. Technol.*, vol. 11, pp. 1694–1700, 1993.

[2-8] E. Brinkmeyer and U. Glombitza, "High-resolution coherent frequency-domain reflectometry using continuously tuned laser diodes," in *proceeding of the Optical Fiber Communication Conference (OFC1991)*, WN2, p.p. 129, San Diego, USA, 1991.

[2-9] S. Venkatesh, W. V. Sorin, D. K. Donald, and B. L. Heffner, "Coherent FMCW reflectometry using a piezoelectrically tuned Nd:YAG ring laser," in *Proceeding of the International Conference on Optical Fibre Sensors*,Monterey, CA, pp. 61-64, 1992.

[2-10] K. Takada, “High-resolution OFDR with incorporated fiber-optic frequency encoder,” *IEEE. Photon. Tech. Lett.*, vol. 4, pp. 1069-1072, 1992.

[2-11] X. Fan, Y. Koshikiya, and F. Ito, “Phase-noise-compensated optical frequency domain reflectometry with measurement range beyond laser coherence length realized using concatenative reference method,” *Opt. Lett.*, vol. 32, pp. 3227-3229, 2007.

[2-12] X. Fan, Y. Koshikiya, and F. Ito, “Phase-noise-compensated optical frequency domain reflectometry,” *J. Quantum Electron.*, vol. 45, pp. 594-602, 2009.

[2-13] A. Yariv and P. Yeh, Photonics: Optical electronics in modern communications. chapter 10, Oxford, U. K.: Oxford Univ. Press, 2007.

Chapter 3.

[3-1] D. K. Gifford, M. E. Froggatt, M. S. Wolfe S. T. Kreger, and B. J. Soller “Millimeter resolution reflectometry over two kilometers,” in *Proceeding of the 33rd European Conference on Optical Communication (ECOC’2007)*,Berlin, Germany vol. 2, paper Tu.3.6.1, pp. 85-87, 2007.

[3-2] K. Tsuji, K. Shimizu, T. Horiguchi, and Y. Koyamada, “Spatial-resolution improvement in long-range coherent optical frequency domain reflectometry by frequency-sweep linearization,” *Electron. Lett.*, vol. 33, pp. 408-410, 1997.

[3-3] J. Geng, C. Spiegelberg, and S. Jiang, “Narrow linewidth fiber laser for 100-km optical frequency domain reflectometry,” *IEEE Photon. Technol. Lett.*, vol. 17, pp. 1827-1829, 2005.

[3-4] Y. Koshikiya, X. Fan, and F. Ito, “Long range and cm-level spatial resolution measurement using coherent optical frequency domain reflectometry with SSB-SC modulator and narrow linewidth fiber laser”, *J. Lightw. Technol.*, vol. 26, pp. 3287–3294, 2008.

[3-5] K. Tsuji, K. Shimizu, T. Horiguchi, and Y. Koyamada, “Coherent optical frequency domain reflectometry for a long single-mode optical fiber using a

coherent lightwave source and an external phase modulator," *IEEE Photon. Technol. Lett.*, vol. 7, pp. 804-806, 1995.

[3-6] K. Tsuji, K. Shimizu, T. Horiguchi, and Y. Koyamada, "Coherent optical frequency domain reflectometry using a dual-drive Mach-Zehnder modulator," in *Proceeding of the 4th Optical Fibre Measurement Conference*, pp. 250-253, 1997.

[3-7] T. Kawanishi, T. Sakamoto, and M. Izutsu, "Fast optical frequency sweep for ultra-fine real-time spectral domain measurement," *Electron. Lett.*, vol. 42, pp. 999-1000, 2006.

[3-8] M. Izutsu, S. Shikama, and T. Sueta, "Integrated optical SSB modulator/frequency shifter," *IEEE J. Quantum Electron.*, vol. QE-17, pp. 2225-2227, 1981.

[3-9] K. Higuma, S. Oikawa, Y. Hashimoto, H. Nagata, and M. Izutsu, "X-cut lithium niobate optical single-sideband modulator," *Electron. Lett.*, vol. 37, pp. 515-516, 2001.

[3-10] U. Glombitza, and E. Brinkmeyer, "Coherent frequency-domain reflectometry for characterization of single-mode integrated-optical waveguide," *J. Lightwave Technol.*, vol. 11, pp. 1377-1384, 1993.

[3-11] G. Mussi, N. Gisin, R. Passy, and J. P. von derWeid, "–152.5 dB sensitivity high dynamic-range optical frequency-domain reflectometry," *Electron. Lett.*, vol. 32, pp. 926–927, 1996.

[3-12] S. Venkatesh, and W. V. Sorin, "Phase noise consideration in coherent optical FMCW reflectometry," *J. Lightw. Technol.*, vol. 11, pp. 1694-1700, 1993.

[3-13] T. J. Ahn, J. Y. Lee, and D. Y. Kim, "Suppression of nonlinear frequency sweep in an optical frequency-domain reflectometer by use of Hilbert transformation," *App. Opt.*, vol. 44, pp. 7630-7634, 2005.

[3-14] H. Izumita, S. Furukawa, Y. Koyamada, and I. Sankawa, "Fading noise reduction in coherent OTDR," *IEEE Photon. Technol. Lett.*, vol. 4, pp. 201-203, 1992.

[3-15] K. Shimizu, T. Horiguchi, and Y. Koyamada, "Characteristics and reduction of coherent fading noise in Rayleigh backscattering measurement for optical fibers and components,", *J. Lightw. Technol.*, vol. 10, pp. 982-987, 1992.

[3-16] X. Fan, Y. Koshikiya, and F. Ito, “Phase-noise-compensated optical frequency domain reflectometry with measurement range beyond laser coherence length realized using concatenative reference method,” *Opt. Lett.*, vol. 32, pp. 3227-3229, 2007.

Chapter 4.

[4-1] Y. Koshikiya, X. Fan, and F. Ito, “40-km range, 1-m resolution measurement based on phase-noise-compensated coherent optical frequency domain reflectometry,” in *Proceedings of the 34th European Conference on Optical Communication (ECOC’2008)*, Brussels, Belgium, vol. 5, P.1.11, pp. 21–22, 2008.

[4-2] X. Fan, Y. Koshikiya, and F. Ito, “Highly sensitive reflectometry over 20 km with submeter spatial resolution based on phase-noise-compensated optical frequency domain reflectometry and concatenative reference method,” in *Proceedings of the 19th International Conference on Optical Fibre Sensors (OFS–19)*, Perth, Australia, vol. 7004, pp. 7004 3L, 2008.

[4-3] X. Fan, Y. Koshikiya, and F. Ito, “Phase-noise-compensated optical frequency-domain reflectometry,” *J. Quantum Electron.*, vol. 45, pp. 594–602, 2009.

[4-4] Y. Koshikiya, X. Fan, and F. Ito, “Influence of acoustic perturbation of fibers in phase-noise compensated optical frequency domain reflectometry,” *J. Lightw. Technol.*, vol. 28, pp. 3323–3328, 2010.

[4-5] Y. Koshikiya, X. Fan, and F. Ito, “Long range and cm-level spatial resolution measurement using coherent optical frequency domain reflectometry with SSB-SC modulator and narrow linewidth fiber laser”, *J. Lightw. Technol.*, vol. 26, pp. 3287–3294, 2008.

Chapter 5.

[5-1] Y. Koshikiya, X. Fan, and F. Ito, "Sub-cm spatial resolution reflectometry over 10 km based on phase noise compensated OFDR with third order sideband sweeping," in *Proceeding of the 35th European Conference on Optical Communication (ECOC'2009),* Tu.4.1.1, Vienna, Austria, 2009.

[5-2] M. Izutsu, S. Shikama, and T. Sueta, "Integrated optical SSB modulator/frequency shifter," *IEEE J. Quantum Electron.*, vol. QE-17, pp. 2225-2227, 1981.

[5-3] K. Higuma, S. Oikawa, Y. Hashimoto, H. Nagata, and M. Izutsu, "X-cut lithium niobate optical single-sideband modulator," *Electron. Lett.*, vol. 37, pp. 515-516, 2001.

[5-4] Y. Koshikiya, X. Fan, and F. Ito, "Long range and cm-level spatial resolution measurement using coherent optical frequency domain reflectometry with SSB-SC modulator and narrow linewidth fiber laser", *J. Lightw. Technol.*, vol. 26, pp. 3287–3294, 2008.

[5-5] Y. Koshikiya, X. Fan, and F. Ito, "Influence of acoustic perturbation of fibers in phase-noise compensated optical frequency domain reflectometry," *J. Lightw. Technol.*, vol. 28, pp. 3323–3328, 2010.

[5-6] X. Fan, Y. Koshikiya, and F. Ito, "Phase-noise-compensated optical frequency domain reflectometry with measurement range beyond laser coherence length realized using concatenative reference method," *Opt. Lett.*, vol. 32, no. 22, pp. 3227-3229, 2007.

[5-7] X. Fan, Y. Koshikiya, and F. Ito, "Phase-noise-compensated optical frequency-domain reflectometry", *J. Quantum Electron.*, vol. 45, pp. 594–602, 2009.

Chapter 6

[6-1] P. Healey, "Fading in heterodyne OTDR," *Electron. Lett.* vol. 20, pp. 30–32, 1984.

[6-2] P. Healey, “Statistics of Rayleigh backscatter from a single-mode optical fiber,” *Electron. Lett.* vol. 21, pp. 226–228, 1985.

[6-3] K. Shimizu, T. Horiguchi, and Y. Koyamada, “Characteristics and reduction of coherent fading noise in Rayleigh backscattering measurement for optical fibers and components,” *J. Lightw. Technol.*, vol. 10, pp. 982-987, 1992.

[6-4] X. Fan, Y. Koshikiya, and F. Ito, “10 cm spatial resolution and 20 km range full polarimetric reflectometry for distributed DGD measurement of high PMD fibres”, in *Proceeding of the 35th European Conference on Optical Communication (ECOC’2009)*, Tu 4.1.2, Vienna, Austria, 2009.

[6-5] E. Brinkmeyer, and R. Ulrich, “High-resolution OCDR in dispersive waveguide,” *Electron. Lett.* vol. 26, pp. 413–414, 1990.

[6-6] A. Kohlhaas, C. Fromchen, and E. Brinkmeyer, “High-resolution OCDR for testing integrated-optical waveguides: dispersion-corrupted experimental data corrected by a numerical algorithm,” *J. Lightw. Technol.*, vol. 9, pp. 1493–1502, 1991.

[6-7] U. Glombitza, and E. Brinkmeyer, “Coherent frequency-domain reflectometry for characterization of single-mode integrated-optical waveguide,” *J. Lightw. Technol.*, vol. 11, pp. 1377–1384, 1993.

[6-8] Y. Koshikiya, X. Fan, F. Ito, Z. He, and K. Hotate, “High resolution PNC-OFDR with suppressed fading noise for dispersive media measurement,” *J. Lightw. Technol.*, vol. 31, pp. 866-873, 2013.

[6-9] T. Yamamoto, T. Komukai, K. Suzuki, and A. Takada, “Multicarrier light source with flattened spectrum using phase modulator and dispersion medium,” *J. Lightw. Technol.*, vol. 27, pp. 4297-4305, 2009.

[6-10] Y. Koshikiya, X. Fan, and F. Ito, “Long range and cm-level spatial resolution measurement using coherent optical frequency domain reflectometry with SSB-SC modulator and narrow linewidth fiber laser,” *J. Lightw. Technol.*, vol. 26, pp. 3287–3294, 2008.

[6-11] Y. Koshikiya, X. Fan, and F. Ito, “Influence of acoustic perturbation of fibers in

phase-noise compensated optical frequency domain reflectometry," *J. Lightw. Technol.*, vol. 28, pp. 3323–3328, 2010.

Chapter 7

[7-1] A. J. Rogers, "Polarization-optical time domain reflectometry: a technique for the measurement of field distributions," *Appl. Opt.*, vol. 20, pp. 1060-1074, 1981.

[7-2] J. G. Ellison and A. S. Siddiqui, "Automatic matrix-based analysis method for extraction of optical fiber parameters from polarimetric optical time domain reflectometry data," *J. Lightw. Technol.*, vol. 18, pp. 1226-1232, 2000.

[7-3] A. Galtarossa and L. Palmieri, "Spatially resolved PMD measurements," *J. Lightwave Technol.*, vol. 22, pp. 1103-1115, 2004.

[7-4] R. Goto, S. Tanigawa, S. Matsuo, and K. Himeno, "On-spool PMD estimation method for low-PMD fibers with high repeatability by local-DGD measurement using POTDR," *J. Lightwave Technol.*, vol. 24, pp. 3914-3919, 2006.

[7-5] H. Dong, P. Shum, J. Q. Zhou, G. X. Ning, Y. D. Gong, and C. Q. Wu, "Spectral-resolved backreflection measurement of polarization mode dispersion in optical fibers," *Opt. Lett.*, vol. 32, pp. 1665-1667, 2007.

[7-6] D. Fritzsche, M. Paul, L. Schuerer, A. Ehrhardt, D. Breuer, W. Weiershausen, N. Cyr, H. Chen, and G. W. Schinn, "Measuring the link distribution of PMD: field trial using an RS-POTDR," in *proceeding of the Optical Fiber Communication Conference (OFC2008)*, NThE2, San Diego, USA, 2008.

[7-7] Y. Koshikiya, X. Fan, and F. Ito, "Influence of acoustic perturbation of fibers in phase-noise compensated optical frequency domain reflectometry," *J. Lightw. Technol.*, vol. 28, pp. 3323–3328, 2010.

[7-8] X. Fan, Y. Koshikiya, and F. Ito, "Centimeter-level spatial resolution over 40 km realized by bandwidth-division phase-noise-compensated OFDR," *Opt. Express*, vol. 19, pp. 19122-19128, 2011.

[7-9] X. Fan, Y. Koshikiya, N. Araki, and F. Ito, "Field trials of PNC-OFDR in different

environments for detecting short beat lengths," *IEEE Photon. Technol. Lett.*, vol. 24, pp. 1288-1291, 2012.

[7-10] X. Fan, Y. Koshikiya, and F. Ito, "Full polarimetric phase-noise-compensated optical-frequency-domain reflectometry for distributed measurement of high-PMD fibers," *Opt. Lett.*, vol. 35, pp. 25-27, 2010.

List of acronyms

A/D	analog to digital converter
AO	acousto-optic
APC	angled physical contact
BPD	balanced photodetector
BPF	band-pass filter
CGP	concatenately generated phase
CO	central office
C-OFDR	coherent optical frequency domain reflectometry
CRM	concatenative reference method
DAC	data acquisition card
DFL	delay fiber line
DSB-SC	double sideband with suppressed carrier
DSF	dispersion shifted fiber
DUT	device under test
FBG	fiber Bragg grating
FL	fiber laser
FMCW	frequency modulated continuous wave
FSAV	frequency shift averaging
FTTH	fiber to the home
FUT	fiber under test
FWHM	full width at half maximum
GVD	group velocity dispersion
JME	Jones matrix eigen-analysis
LN-IM	$LiNbO_3$ intensity modulator
LPF	low-pass filter
MI	main interferometer
MZI	Mach-Zehnder interferometer
OFDR	optical frequency domain reflectometry
OLCR	optical low coherence reflectometry
ONT	optical network terminal
OTDR	optical time domain reflectometry
PBS	polarization beam splitter

PC	polarization controller
PMD	polarization-mode dispersion
PNC	phase noise compensation
PNC-OFDR	phase noise compensated optical frequency domain reflectometry
P-OTDR	polarization-sensitive optical time domain reflectometry
RI	reference interferometer
SFS	synthesized frequency sweeper
SMF	single mode fiber
SNR	signal-to-noise ratio
SOP	states of polarization
SSB-SC	single sideband with a suppressed carrier

List of publications

Papers related to this thesis

[1] Y. Koshikiya, X. Fan, F. Ito, Z. He, and K. Hotate, "High resolution PNC-OFDR with suppressed fading noise for dispersive media measurement," *J. Lightw. Technol.*, vol. 31, no. 6, pp. 866-873, Mar. 2013.

[2] F. Ito, X. Fan, and Y. Koshikiya, "Long-range coherent OFDR with light source phase noise compensation (invited)," *J. Lightw. Technol.*, vol. 30, no.8, pp. 1015-1024, Apr. 2012.

[3] X. Fan, Y. Koshikiya, and F. Ito, "Centimeter-level spatial resolution over 40 km realized by bandwidth-division phase-noise-compensated OFDR," *Opt. Express*, vol. 19, pp. 19122-19128, Sep. 2011.

[4] Y. Koshikiya, X. Fan, and F. Ito, "Influence of acoustic perturbation of fibers in phase-noise-compensated optical-frequency-domain reflectometry,"*J. Lightw. Technol.*, vol. 28, no. 22, pp. 3323-3328, Nov. 2010.

[5] X. Fan, Y. Koshikiya, and F. Ito, "Phase-noise-compensated optical frequency-domain reflectometry," *J. Quantum Electron.*, vol. 45, no. 6, pp. 594-602, Jun. 2009.

[6] Y. Koshikiya, X. Fan, and F. Ito, "Long range and cm-level spatial resolution measurement using coherent optical frequency domain reflectometry with SSB-SC modulator and narrow linewidth fiber laser", *J. Lightw. Technol.*, vol. 26, no. 18, pp. 3287-3294, Sep. 2008.

[7] Y. Koshikiya, N. Araki, H. Izumita, and F. Ito, "Newly developed optical fiber line testing system employing bi-directional OTDRs for PON and in-service line testing criteria," *IEICE Trans. Commun.*, vol. E90-B, no. 10, pp. 2793-2802, Oct. 2007.

Letters related to this thesis

[1] X. Fan, Y. Koshikiya, N. Araki, and F. Ito, "Field trials of PNC-OFDR in different environments for detecting short beat lengths," *IEEE Photon. Technol. Lett.*, vol. 24, no. 15, pp. 1288-1291, Aug. 2012.

[2] X. Fan, Y. Koshikiya, and F. Ito, "Full polarimetric phase-noise-compensated optical-frequency-domain reflectometry for distributed measurement of high-PMD fibers," *Opt. Lett.*, vol. 35, no. 1, pp. 25-27, Jan. 2010.

[3] X. Fan, Y. Koshikiya, and F. Ito, "Phase-noise-compensated optical frequency domain reflectometry with measurement range beyond laser coherence length realized using concatenative reference method," *Opt. Lett.*, vol. 32, no. 22, pp. 3227-3229, Nov. 2007.

International conferences related to this thesis

[1] F. Ito, X. Fan, and Y. Koshikiya, "Identification of high-PMD sections along installed optical cables with long range OFDR," in *Technical Digest of the Optical Fiber Communication Conference and Exposition (OFC 2013)*, OW4H.2, Anaheim, USA, Mar. 2013.

[2] X. Fan, Y. Koshikiya, K. Okamoto, H. Iida, H. Takahashi, and F. Ito, "Field trial of cm-level resolution PNC-OFDR for identifying high-birefringence section," in *Proceeding of the 37th European Conference on Optical Communication (ECOC'2011)*, Tu.6.LeCervin.6, Geneva, Switzerland, Sep. 2011.

[3] F. Ito, X. Fan, and Y. Koshikiya, "Long-range coherent optical frequency domain reflectometry and its applications (invited)," in *Proceeding of the 21st International Conference on Optical Fibre Conference (OFS-21)*, Proc. of SPIE, 77533F-1, Ottawa, Canada, May 2011.

[4] X. Fan, Y. Koshikiya, and F. Ito, "2-cm spatial resolution over 40 km realized by bandwidth division phase-noise-compensated OFDR," in *Technical Digest of the Optical Fiber Communication Conference and Exposition (OFC 2011)*, OMF3, Los Angeles, USA, Mar. 2011.

[5] F. Ito, X. Fan, and Y. Koshikiya, "Long-range coherent OFDR with light source phase noise compensation (invited)," in *Proceeding of the 9th International Conference on Optical Communications and Networks (ICOCN 2010)*, pp. 5-8, Nanjing, China, Oct. 2010.

[6] Y. Koshikiya, X. Fan, F. Ito, Z. He, and K. Hotate, "Fading-noise suppressed cm-level resolution reflectometry over 10-km range with phase noise and chromatic dispersion compensation," in *Proceeding of the 36th European Conference on Optical Communication (ECOC'2010)*, Tu.3.F.2, Turin, Italy, Sep. 2010.

[7] X. Fan, Y. Koshikiya, and F. Ito, "Noise of long-range optical frequency domain reflectometry after optical source phase noise compensation," in *Proceeding of the 20th International Conference on Optical Fibre Sensors (OFS-20)*, Proc. of SPIE, 75032E, Edinburgh, UK, Oct. 2009.

[8] Y. Koshikiya, X. Fan, and F. Ito, "Sub-cm spatial resolution reflectometry over 10 km based on phase noise compensated OFDR with third order sideband sweeping," in *Proceeding of the 35th European Conference on Optical Communication (ECOC' 2009)*, Tu.4.1.1, Vienna, Austria, Sep. 2009.

[9] X. Fan, Y. Koshikiya, and F. Ito, "10 cm spatial resolution and 20 km range full polarimetric reflectometry for distributed DGD measurement of high PMD fibres," in *Proceeding of the 35th European Conference on Optical Communication (ECOC'2009)*, Tu.4.1.2, Vienna, Austria, Sep. 2009.

[10] Y. Koshikiya, X. Fan, and F. Ito, "40-km Range, 1-m resolution measurement based on phase-noise-compensated coherent optical frequency domain reflectometry," in *Proceeding of the 34th European Conference on Optical Communication (ECOC' 2008)*, vol. 5, P.1.11, pp. 21-22, Brussels, Belgium, Sep. 2008.

[11] X. fan, Y. Koshikiya, and F. Ito, "Evolution of backscattered polarization in high-PMD fibres measured by phase-noise compensated optical frequency domain reflectometry," in *Proceeding of the 34th European Conference on Optical Communication (ECOC'2008)*, vol. 5, P.1.12, pp. 23-24, Brussels, Belgium, Sep. 2008.

[12] X. fan, Y. Koshikiya, and F. Ito, "Highly sensitive reflectometry over 20 km with submeter spatial resolution based on phase-noise-compensated optical frequency domain reflectometry and concatenative reference method," in *Proceeding of the 19th International Conference on Optical Fibre Sensors (OFS-19)*, vol. 7004, pp. 7004 3L, Perth, Australia, Apr. 2008.

[13] F. Ito, Y. Koshikiya, and X. Fan, "High-resolution fiber line measurement based on optical frequency domain reflectometry," in *Proceeding of the 8th Chitose International Forum on Photonics Science & Technology (CIF'8)*, pp. 71-77, Chitose, Japan, Nov. 2007.

[14] Y. Koshikiya, X. Fan, and F. Ito, "Highly sensitive coherent optical frequency-domain reflectometry employing SSB-modulator with cm-level spatial resolution over 5 km," in *Proceeding of the 33rd European Conference on Optical Communication (ECOC' 2007)*, vol. 2, paper Tu.3.6.2, pp. 89-90, Berlin, Germany, Sep. 2007.

[15] Y. Koshikiya, N. Araki, H. Izumita, and F. Ito, "Simple and cost-effective fault location technique using bi-directional OTDR and in-service line testing criteria for PONs," in *Proceedings of the 31st European Conference on Optical Communication (ECOC'2005)*, vol. 1, paper Mo.4.3.2, pp. 83-84, Glasgow, U.K., Sep. 2005.

[16] Y. Koshikiya, N. Araki, H. Izumita, and M. Nakamura, "New design for optical fiber line testing system employing two-wavelength bidirectional OTDR for PON," in *Technical digest of the 9th Optical Electronics and Communications Conf. (OECC'2004)*, no. 15A3-4, pp. 600-601, Yokohama, Japan, Jul. 2004.

Domestic conferences related to this thesis

[1] Y. Koshikiya, X. Fan, and F. Ito, "Characteristics of PNC-OFDR in acoustic noise environment," IEICE Technical Report, OCS2010-87, pp. 177-182, Oct. 2010 (in Japanese).

[2] Y. Koshikiya, X. Fan, F. Ito, Z. He, and K. Hotate, "cm-level resolution reflectometry over 10-km range with phase noise and chromatic dispersion simultaneous

compensation," IEICE Technical Report, OCS2010-45, pp. 53-58, Aug. 2010 (in Japanese).

[3] Y. Koshikiya, X. Fan, and F. Ito, "Phase noise compensated optical frequency domain reflectometry with higher spatial resolution," IEICE Technical Report, OFT2009-94, pp. 59-62, Feb. 2010 (in Japanese).

[4] Y. Koshikiya, X. Fan, and F. Ito, "Limitation factor of spatial resolution for 40 km range measurement with PNC-OFDR," IEICE Technical Report, OCS2009-30, pp. 5-11, Aug. 2009 (in Japanese).

[5] Y. Koshikiya, X. Fan, and F. Ito, "40-km range, 1-m resolution measurement employing phase-noise compensated C-OFDR," IEICE Technical Report, OCS2008-46, pp. 69-72, Aug. 2008 (in Japanese).

[6] Y. Koshikiya, X. Fan, and F. Ito, "Measurement of Rayleigh backscattering by highly sensitive SSB-OFDR with high spatial resolution," IEICE Technical Report, OFT2007-27, pp. 71-76, Aug. 2007 (in Japanese).

Patents related to this thesis

[1] 古敷谷優介他 5 名, 光周波数領域反射測定方法及び光周波数領域反射測定装置, 特許第 5207252, 2013 年 3 月

[2] 古敷谷優介他 2 名, 光周波数変調装置, 特許第 5193708, 2013 年 2 月 A

[3] 古敷谷優介他 2 名, 光周波数領域反射測定方法および装置, 特許第 4918523, 2012 年 2 月

[4] ファンシンユウ, 伊藤文彦, 古敷谷優介, 光リフレクトメトリ測定方法および装置, 特許第 4917640, 2012 年 2 月

[5] 古敷谷優介他 1 名, 光周波数領域反射測定方法および装置, 特許第 5159255, 2012 年 2 月

[6] 古敷谷優介他 4 名, 光周波数領域反射測定方法及び光周波数領域反射測定装置, 特開 2012-154790, 2012 年 8 月

[7] ファンシンユウ, 伊藤文彦, 古敷谷優介, 光周波数領域反射測定方法及び光周波数領域反射測定装置, 特開 2012-117886, 2012 年 6 月

[8] 古敷谷優介 他 4 名, 光周波数領域反射測定方法及び光周波数領域反射測定装置, 特開 2011-174760, 2011 年 9 月

[9] 古敷谷優介 他 2 名, 光周波数領域反射測定方法及び光周波数領域反射測定装置, 特開 2011-038839, 2011 年 2 月

[10] ファンシンユウ, 伊藤文彦, 古敷谷優介 他 3 名, 光リフレクトメトリ測定方法及び光リフレクトメトリ測定装置, 特開 2011-022082, 2011 年 2 月

[11] 古敷谷優介 他 2 名, 光周波数領域反射測定方法及び装置, 特開 2010-185842, 2010 年 8 月